INL/EXT-06-11681

# Energy Conversion Advanced Heat Transport Loop and Power Cycle

Chang H. Oh
Robert B. Barner
Cliff B. Davis
Brian D. Hawkes
Jennifer D. Morton

August 2006


The INL is a U.S. Department of Energy National Laboratory
operated by Battelle Energy Alliance

INL/EXT-06-11681

# Energy Conversion Advanced Heat Transport Loop and Power Cycle

**Chang H. Oh**
**Robert B. Barner**
**Cliff B. Davis**
**Brian D. Hawkes**
**Jennifer D. Morton**

**August 2006**

**Idaho National Laboratory**
**Idaho Falls, Idaho 83415**

**Prepared for the**
**U.S. Department of Energy**
**Office of Nuclear Energy**
**Under DOE Idaho Operations Office**
**Contract DE-AC07-05ID14517**

## ABSTRACT

The Department of Energy and the Idaho National Laboratory are developing a Next Generation Nuclear Plant (NGNP) to serve as a demonstration of state-of-the-art nuclear technology. The purpose of the demonstration is two fold: 1) efficient low cost energy generation and 2) hydrogen production. Although a next generation plant could be developed as a single-purpose facility, early designs are expected to be dual-purpose. While hydrogen production and advanced energy cycles are still in its early stages of development, research towards coupling a high temperature reactor, electrical generation and hydrogen production is under way. Many aspects of the NGNP must be researched and developed in order to make recommendations on the final design of the plant. Parameters such as working conditions, cycle components, working fluids, and power conversion unit configurations must be understood.

Three configurations of the power conversion unit were demonstrated in this study. A three-shaft design with three turbines and four compressors, a combined cycle with a Brayton top cycle and a Rankine bottoming cycle, and a reheated cycle with three stages of reheat were investigated. An intermediate heat transport loop for transporting process heat to a High Temperature Steam Electrolysis (HTSE) hydrogen production plant was used. Helium, $CO_2$, and an 80% nitrogen, 20% helium mixture (by weight) were studied to determine the best working fluid in terms cycle efficiency and development cost. In each of these configurations the relative component size were estimated for the different working fluids. The relative size of the turbomachinery was measured by comparing the power input/output of the component. For heat exchangers, the volume was computed and compared. Parametric studies away from the baseline values of the three-shaft and combined cycles were performed to determine the effect of varying conditions in the cycle. This gives some insight into the sensitivity of these cycles to various operating conditions as well as trade offs between efficiency and capital cost. Parametric studies were carried out on reactor outlet temperature, mass flow, pressure, and turbine cooling. Recommendations on the optimal working fluid for each configuration were made.

Engineering analyses were performed for several configurations of the intermediate heat transport loop that transfers heat from the nuclear reactor to the hydrogen production plant. The analyses evaluated parallel and concentric piping arrangements and two different working fluids, including helium and a liquid salt. The thermal-hydraulic analyses determined the size and insulation requirements for the hot and cold leg pipes in the different configurations. Mechanical analyses were performed to determine hoop stresses and thermal expansion characteristics. Economic analyses were performed to estimate the cost of the various configurations.

## CONTENTS


ABSTRACT ..... iii
TABLES ..... vi
FIGURES ..... vi
1.0 INTRODUCTION ..... 1
2.0 CYCLE ANALYSIS ASSUMPTIONS ..... 2
3.0 METHODS ..... 3
3.1 Design Configuration ..... 3
3.1.1 Three-Shaft Cycle ..... 6
3.1.2 Combined Cycle ..... 7
3.1.3 Reheated Cycle ..... 7
3.1.4 HTSE Hydrogen Plant ..... 8
3.2 Working Fluids ..... 10
3.3 Efficiency Optimization ..... 10
3.4 Component Sizing and Pressure Drops ..... 13
3.5 Parametric Studies ..... 19
3.5.1 Reactor outlet temperature ..... 20
3.5.2 Mass flow ..... 20
3.5.3 Pressure ..... 20
3.5.4 Turbine cooling ..... 20
4.0 CYCLE ANALYSIS RESULTS ..... 21
4.1 Three-Shaft Design ..... 21
4.1.1 Helium Working Fluid ..... 21
4.1.2 $CO_2$ Working Fluid ..... 23
4.1.3 Nitrogen-Helium Working Fluid ..... 25
4.1.4 Parametric Studies ..... 27
4.2 Combined Cycle ..... 29
4.2.1 Helium Working Fluid ..... 30
4.2.2 $CO_2$ Working Fluid ..... 32
4.2.3 Nitrogen-Helium Working Fluid ..... 34
4.2.4 Parametric Studies ..... 36
4.3 Reheated Cycle ..... 38
4.3.1 Helium Working Fluid ..... 38
4.3.2 $CO_2$ Working Fluid ..... 41
4.3.3 Nitrogen-Helium Working Fluid ..... 44
4.4 Effects of IHTL and HTSE ..... 46
5.0 ENGINEERING ANALYSES OF THE IHTL ..... 49
5.1 Thermal-Hydraulic Analyses ..... 49
5.2 Mechanical Analyses ..... 56
5.3 Economic Analyses ..... 71
6.0 CONCLUSIONS ..... 74
7.0 REFERENCES ..... 76

## TABLES


1. Summary of primary working conditions for three-shaft and combined cycles ..... 3
2. Summary of primary working conditions for reheated cycle ..... 4
3. Working conditions in the IHTL ..... 4
4. Cycle conditions for three-shaft configuration ..... 12
5. Cycle conditions for combined configuration ..... 12
6. Cycle conditions for the reheated configuration ..... 13
7. State points for three-shaft configuration with helium working fluid ..... 23
8. Component sizing data for three-shaft configuration with helium working fluid ..... 23
9. State points for three-shaft configuration with $CO_2$ working fluid ..... 25
10. Component sizing data for three-shaft configuration with $CO_2$ working fluid ..... 25
11. State points for three-shaft configuration with a nitrogen-helium mixture working fluid ..... 27
12. Component sizing data for three-shaft configuration with a nitrogen-helium mixture working fluid ..... 27
13. Parametric study of the effects of turbine cooling on three-shaft cycle efficiency ..... 29
14. State points for Rankine bottoming cycle ..... 30
15. State points for Brayton top cycle with helium working fluid ..... 32
16. Component sizing data for combined cycle with helium working fluid ..... 32
17. State points for Brayton top cycle with $CO_2$ working fluid ..... 34
18. Component sizing data for combined cycle with $CO_2$ working fluid ..... 34
19. State points for Brayton top cycle with a nitrogen-helium mixture working fluid ..... 36
20. Component sizing data for combined cycle with a nitrogen-helium mixture ..... 36
21. Parametric study of the effects of turbine cooling on combined cycle efficiency ..... 38
22. State points for the reheated configuration with helium working fluid ..... 41
23. Component sizing data for reheated cycle with helium working fluid ..... 41
24. State points for the reheated configuration with $CO_2$ working fluid ..... 43
25. Component sizing data for reheated cycle with $CO_2$ working fluid ..... 43
26. State points for the reheated configuration with a nitrogen-helium mixture working fluid ..... 46
27. Component sizing data for reheated cycle with a nitrogen-helium mixture working fluid ..... 46
28. Summary of overall plant efficiency for each PCU configuration and IHTL working fluid ..... 48
29. Excess power available for electrical generation for each PCU configuration and IHTL working fluid ..... 48
30. Engineering analysis parameters ..... 51
31. Stress analysis parameters ..... 57
32. Stress analysis results ..... 57
33. Hot leg parameters ..... 58
34. Results of thermal expansion calculations ..... 59
35. Parameteres of Concentric Pipe ..... 65
36. Jacketed Configuration ..... 67
37. Estimated IHTL costs ..... 71


## FIGURES


1. Schematic of parallel HTLHX option for the three-shaft and combined cycle configurations ..... 5
2. Schematic of HTLHX configuration when using the reheat option ..... 5
3. IHTL process heat exchanger configuration ..... 6

4. Schematic of three-shaft cycle PCU configuration ..... 6
5. Schematic of the combined cycle PCU configuration ..... 7
6. Schematic of the reheated cycle PCU configuration ..... 8
7. Schematic of the HTSE process ..... 9
8. HYSYS diagram of three-shaft configuration with helium working fluid..... 22
9. T-S diagram for three-shaft configuration with helium working fluid ..... 22
10. HYSYS diagram of three-shaft configuration with $CO_2$ working fluid ..... 24
11. T-S diagram of three-shaft configuration with $CO_2$ working fluid ..... 24
12. HYSYS diagram of three-shaft configuration with a nitrogen-helium mixture working fluid 1 ..... 26
13. T-S diagram of three-shaft configuration with a nitrogen-helium mixture working fluid..... 26
14. Parametric study of the effects of reactor outlet temperature on three-shaft cycle efficiency..... 28
15. Parametric study of the effects of secondary mass flow rate on three-shaft cycle efficiency..... 28
16. Parametric study of the effects of working pressure on three-shaft cycle efficiency ..... 29
17. T-S diagram for Rankine bottoming cycle..... 30
18. HYSYS diagram of the combined cycle with helium working fluid ..... 31
19. T-S diagram for combined cycle with helium working fluid ..... 31
20. HYSYS diagram of Brayton top cycle with $CO_2$ working fluid ..... 33
21. T-S diagram of Brayton top cycle with $CO_2$ working fluid ..... 33
22. HYSYS diagram of Brayton top cycle with a nitrogen-helium mixture working fluid ..... 35
23. T-S diagram of Brayton top cycle with a nitrogen-helium mixture working fluid ..... 35
24. Parametric study of the effects of reactor outlet temperature on combined cycle efficiency..... 37
25. Parametric study of the effects of secondary mass flow rate on combined cycle efficiency ..... 37
26. Parametric study of the effects of working pressure on combined cycle efficiency ..... 38
27. HYSYS diagram of the reheated configuration with helium working fluid ..... 39
28. T-S diagram for the reheated configuration with helium working fluid ..... 40
29. HYSYS diagram of the reheated configuration with helium working fluid on primary and secondary sides ..... 40
30. HYSYS diagram of the reheated configuration with $CO_2$ working fluid ..... 42
31. T-S diagram of the reheated configuration with $CO_2$ working fluid ..... 42
32. HYSYS diagram of the reheated configuration with a nitrogen-helium mixture working fluid ..... 44
33. T-S diagram of the reheated configuration with a nitrogen-helium mixture working fluid ..... 45
34 HYSYS model of entire plant with a three-shaft PCU and HTSE plant ..... 47
35. Parallel and concentric piping configuration for the IHTL l..... 50
36. Thermal-hydraulic conditions for a 50-MW loop with helium working fluid ..... 52
37. Thermal-hydraulic conditions for a 600-MW loop with helium working fluid ..... 52
38. Thermal-hydraulic conditions for a 50-MW loop with $NaBF_4$-NaF working fluid ..... 53
39. Thermal-hydraulic conditions for a 600-MW loop with $NaBF_4$-NaF working fluid..... 53
40. The effect of configuration, power, and separation distance on cold leg diameter with helium as the working fluid ..... 54
41 The effect of configuration, power, and separation distance on the cold leg insulation thickness with helium as the working fluid ..... 55
42. The effect of working fluid on the cold leg diameter for the parallel configuration ..... 55

43. The effect of working fluid on the insulation thickness in the cold leg for the parallel configuration ..... 56
44. Deformation for Inconel in the semi-circular configuration at 355 °C operating temperature ..... 60
45. Highest calculated stresses for Inconel in the semi-circular configuration at 355 °C operating temperature ..... 60
46. Deformation for Inconel in the expansion loop configuration at 355 °C operating temperature ..... 61
47. Highest calculated stresses for Inconel in the expansion loop configuration at 355 °C operating temperature ..... 61
48. Deformation for carbon steel in the semi-circular configuration at 355 °C operating temperature ..... 62
49. Highest calculated stresses for carbon steel in the semi-circular configuration at 355 °C operating temperature ..... 62
50. Deformation for carbon steel in the expansion loop configuration at 355 °C operating temperature ..... 63
51. Highest calculated stresses for carbon steel in the expansion loop configuration at 355 °C operating temperature ..... 63
52. Deformation plot for concentric configuration with Inconel ..... 66
53. Highest stress table for concentric configuration with Inconel ..... 66
54. Deformation plot for jacketed configuration with Inconel 617 pipe ..... 68
55. Highest stress table for jacketed configuration with Inconel 617 pipe ..... 69
56. The effect of configuration, power, and separation distance on IHTL piping costs with helium as the working fluid ..... 70

## 1.0 INTRODUCTION

The Department of Energy and the Idaho National Laboratory are developing a Next Generation Nuclear Plant (NGNP) to serve as a demonstration of state-of-the-art nuclear technology. The purpose of the demonstration is two fold: 1) efficient low cost energy generation and 2) hydrogen production. Although a next generation plant could be developed as a single-purpose facility, early designs are expected to be dual-purpose. While hydrogen production and advanced energy cycles are still in its early stages of development, research towards coupling a high temperature reactor, electrical generation and hydrogen production is under way. Many aspects of the NGNP must be researched and developed in order to make recommendations on the final design of the plant. Parameters such as working conditions, materials, stresses, cycle components, working fluids, coupling of the hydrogen production plant and power conversion unit (PCU) configurations must be understood.

This report describes various PCU configurations coupled to a High Temperature Steam Electrolysis (HTSE) plant by means of an intermediate heat transport loop (IHTL). The key issues that are addressed in this document are:

1. PCU configuration options
2. Coupling of the HTSE to the reactor
3. Working fluids in the PCU and IHTL
4. Efficiency
5. Component sizing
6. IHTL thermal-hydraulic and economic performance
7. IHTL piping mechanical performance

The commercial process code HYSYS (Aspen Technology 2005) was used to model three configurations of the PCU coupled to a HTSE plant. A three-shaft design with three turbines and four compressors, a combined cycle with a Brayton top cycle and a Rankine bottoming cycle, and a reheated cycle with three stages of reheat were investigated. An IHTL was used for transporting heat to the HTSE plant. This IHTL was taken from configuration 6 from a report by Davis et al. (2005). The HTSE plant was adapted from work by Stoots et al. (2005). This same IHTL and HTSE were used for all configurations and parametric studies in this report.

Helium, $CO_2$, and an 80% nitrogen, 20% helium mixture (by weight) were studied to determine the best working fluid in terms cycle efficiency and development cost. Helium is a well understood fluid and has been used in numerous studies pertaining to nuclear power. $CO_2$ has been slow in developing due to material concerns with the fluid. $CO_2$ does possess some advantages over helium such as a higher density allowing for smaller velocities than helium for the same pressure drops (Perry et al. 1984). Despite the lower specific heat, the volumetric flow rates are smaller for $CO_2$ than for a helium cycle generating equivalent power. Therefore, the turbomachinery sizes are smaller for $CO_2$. Copsey et al. (2004) used the nitrogen-helium mixture for the working fluid in a combined cycle. Helium and a liquid salt ($NaBF_4$-NaF) as recommended by Davis et al. (2005) were studied in the IHTL.

In each of these configurations relative component sizes were estimated for the different working fluids. The relative size of the turbomachinery was measured by comparing the power input/output of the component. For heat exchangers the volume was computed and compared.

Parametric studies away from the baseline values of the systems were performed to determine the effect of varying conditions in the cycle. This gives some insight into the sensitivity of these cycles to various

operating conditions. The parametric studies were carried out on reactor outlet temperature, mass flow in the PCU, pressure in the PCU, and turbine cooling.

Thermal-hydraulic, mechanical, and economic analyses of the IHTL were performed for different piping configurations and working fluids. The piping configurations included parallel and concentric arrangements.

## 2.0 CYCLE ANALYSIS ASSUMPTIONS

Both direct and indirect cycles have been postulated for use in the NGNP. The direct cycle eliminates the need for an intermediate heat exchanger (IHX) between the primary and secondary loop and therefore has a higher efficiency. However this poses increased development risk due to the lack of separation between the reactor, secondary components, and the hydrogen production plant. An indirect cycle has decreased risk and only a small decrease in efficiency while also allowing for the use of $CO_2$ as a working fluid in the secondary side. Furthermore, the Independent Technology Review Group (2004) recommended the use of an indirect cycle for the NGNP. Consequently, an indirect cycle was assumed for this study.

The NGNP was assumed to produce 600 MW of thermal power with a 900 °C outlet temperature and use helium coolant on the primary side. The nominal rise in fluid temperature across the core was assumed to be 400 °C, based on the point design (MacDonald et al. 2003). However for the reheat option this value was not used and a smaller temperature rise was calculated and applied to take advantage of the cycle.

The IHTL was assumed to be the same for all configurations. The loop was developed by Davis et al. (2005) and consists of piping to the hydrogen process plant, a heat exchanger between the loop and hydrogen process plant called the process heat exchanger (PHX), and a circulator. The IHTL was assumed to receive 50 MW of thermal power (ANLW 2004). Estimations of the required separation distance between the nuclear and hydrogen process plant vary considerably. For example, Sochet et al. (2004) recommended 500 m for the High-Temperature Reactor while Smith et al. (2005) recommended a separation distance of from 60 to 120 m for the NGNP. For this analysis, a nominal value of 90 m was used. The working fluid in the loop is assumed to be helium.

In this analysis two configurations were used for the IHTL. The first configuration was used in the baseline cycle models and assumed one IHX between the primary and secondary side. The flow on the cold side of the IHX was divided with most of the flow going towards the PCU and the rest going towards the IHTL. For convenience, the heat exchanger connected to the IHTL will be referred to as the heat transport loop heat exchanger (HTLHX). The reheat option did not allow for this configuration so a new configuration was developed in which the HTLHX is in parallel with the IHXs in the primary loop.

Hydrogen production is achieved by HTSE. The HTSE plant receives the necessary process heat from the IHTL. This heat is transferred to the HTSE plant by means of three process heat exchangers (PHXs). The electrical power needed for the electrolyzer will come from the electrical power produced by the PCU.

The nominal reactor pressure was assumed to be 7 MPa (INEEL 2005). The cycle working pressure was also assumed to be 7 MPa. The pressure drop across the hot-side of the IHX was assumed to be 0.05 MPa. From the component sizing calculations the cold side pressure drop was then calculated. For the HTLHX the nominal cold side pressure drop was taken to be 0.139 MPa (Davis et al 2005). The recuperator was assumed to have a hot side pressure drop of 0.1 MPa. The precoolers and intercoolers in the three-shaft and reheated cycles were assumed to have a 0.05 MPa pressure drop.

## 3.0 METHODS

This section describes the methods that were used in coupling the HTSE plant to the reactor, determining the overall efficiency, component sizes and cycle sensitivity to varying working conditions. The design configurations that were studied are described in Section 3.1. The working fluids selection process is explained in Section 3.2. The optimization process that was used to determine maximum cycle efficiency is illustrated in Section 3.3. Section 3.4 establishes the processes for determining component sizes. Finally, parametric studies were performed on the various PCU configurations and are described in Section 3.5.

### 3.1 Design Configuration

The design of the NGNP power conversion unit is demonstrated using three-shaft, combined and reheated cycle designs to better understand the consequences of various cycle configurations. The primary side of the plant was kept constant for the three-shaft and combined cycles. The primary side working conditions for the NGNP are summarized in Table 1~~Table 1~~.

**Table 1. Summary of primary working conditions for three-shaft and combined cycles.**

| Parameter | Nominal Value |
|---|---|
| Power, MW | 600 |
| Inlet temperature, °C | 500 |
| Inlet Pressure, MPa | 7.05 |
| Outlet temperature, °C | 900 |
| Outlet pressure, MPa | 7 |
| IHX pressure drop, MPa | 0.05 |
| Mass Flow, kg/s | 289 |
| Working fluid | He |

In the reheated cycle, the primary side was altered to produce a more realistic model of the cycle. The reactor inlet temperature must be raised to take advantage of the reheat option. This was done by raising the mass flow through the primary side. The additional IHXs needed for the reheat cycle make the use of helium in the primary side infeasible. The additional pressure drop incurred by the heat exchangers offsets the benefits of reheating. Therefore to take advantage of reheating, a liquid salt, which has a very small pressure drop relative to helium, was used as the primary working fluid. Flibe, which is composed of 66% LiF and 42% $BeF_2$, by weight, was used for this study. Flibe is a nearly incompressible liquid. The pressure drop for this fluid is very low and was assumed to be negligible. The primary side working conditions for the reheat cycle are summarized in Table 2~~Table 2~~.

**Table 2. Summary of primary working conditions for reheated cycle.**

| Parameter | Nominal Value |
|---|---|
| Power, MW | 600 |
| Pressure, MPa | 0.1013 |
| Reactor outlet temperature, °C | 900 |
| IHX pressure drop, MPa | 0 |

The NGNP is envisioned to be a demonstration plant for hydrogen production and electrical generation. In order for hydrogen production to be possible, process heat from the reactor must be transported to the hydrogen production plant. To accomplish this, an IHTL was added to the NGNP design. This loop is coupled to the secondary side of the NGNP through the HTLHX. The loop that is used in this document was developed by Davis et al. (2005). The working conditions in that loop are summarized in Table 3~~Table 3~~. Both helium and liquid salts were considered as working fluids for the IHTL. The liquid salt $NaBF_4$-NaF in molar concentrations of 92% and 8% was used because of its low freezing temperature of 385 °C. The use of this liquid salts can potentially increase the heat transfer and reduce the pumping power; however it also introduces material problems such as compatibility and freezing. Davis et al. (2005) further detail the advantages and disadvantages of using a liquid salt in the IHTL.

**Table 3. Working conditions in the IHTL.**

| Parameter | Nominal Value | |
|---|---|---|
| | He | $NaBF_4$-NaF |
| Power, MW | 50.4 | 49.3 |
| Heat Loss, MW | 1.79 | 1.79 |
| Outlet temperature of HTLHX, °C | 875.1 | 875.1 |
| Pressure drop, kPa | 139.0 | 5.0 |
| Pressure, MPa | 2 | 2 |
| Mass Flow, kg/s | 27.5 | 94.8 |

The HTLHX is placed in the secondary side in parallel with the PCU for the three-shaft and combined cycles. In this configuration, which is illustrated in Figure 1~~Figure 1~~, the IHX cold-side outlet fluid is split, with most going towards the PCU and the remainder going towards the hydrogen production plant. A small circulator is required to compensate for the pressure loss across the HTLHX and allow the fluid streams to mix downstream of the PCU. For the reheated cycle, the HTLHX is placed in the primary side as illustrated in Figure 2~~Figure 2~~.

The coupling of the IHTL to the HTSE was accomplished by means of three PHXs. Figure 3~~Figure 3~~ details the configuration of the PHXs in the IHTL. Two heat exchangers in parallel are followed by one heat exchanger in series. This configuration was chosen to deliver high inlet temperatures on the hot side of the first two heat exchangers where high cold side outlet temperatures are needed for the HTSE plant. The third heat exchanger however, does not require high cold side outlet temperatures

and the hot side inlet temperature from the outlet of the prior heat exchangers is sufficient for heating the cold side fluid.

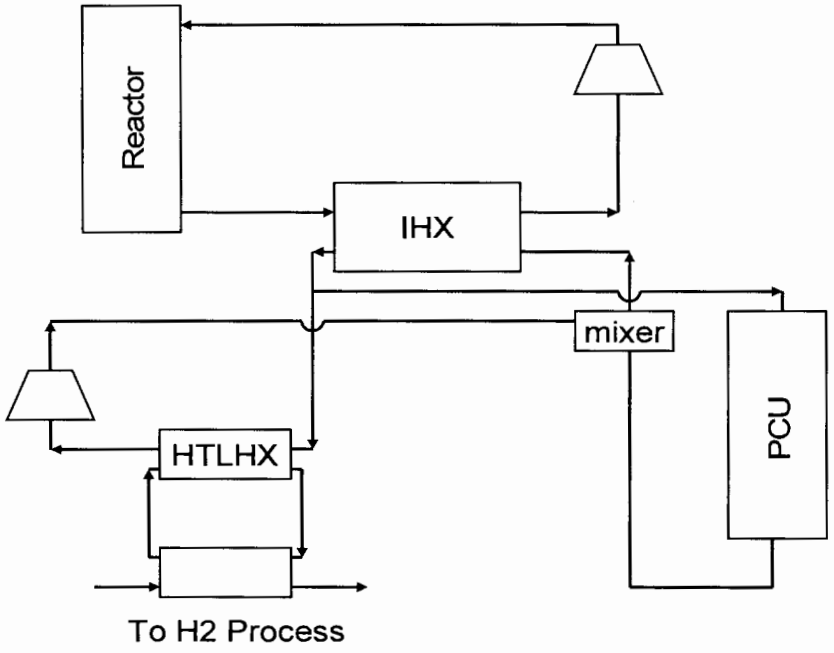


**Figure 1. Schematic of parallel HTLHX option for the three-shaft and combined cycle configurations.**

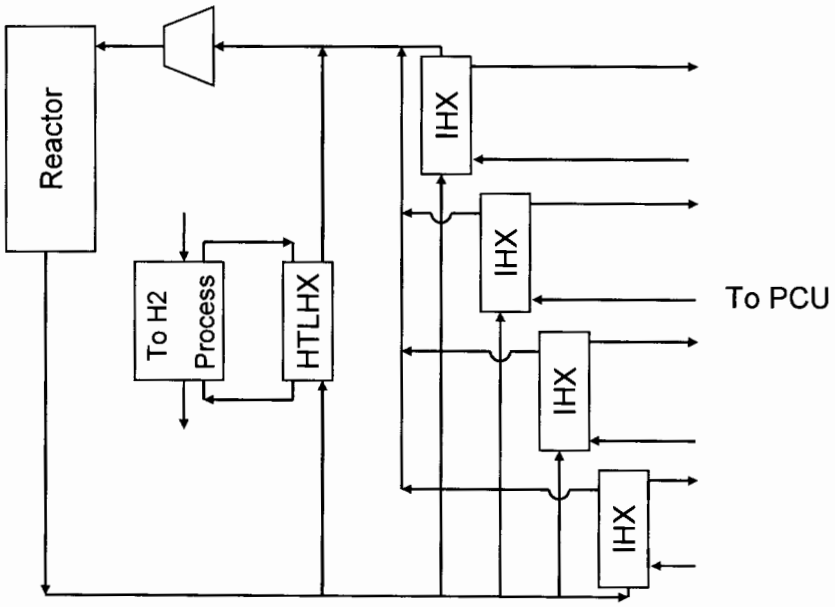


**Figure 2. Schematic of HTLHX configuration when using the reheat option.**

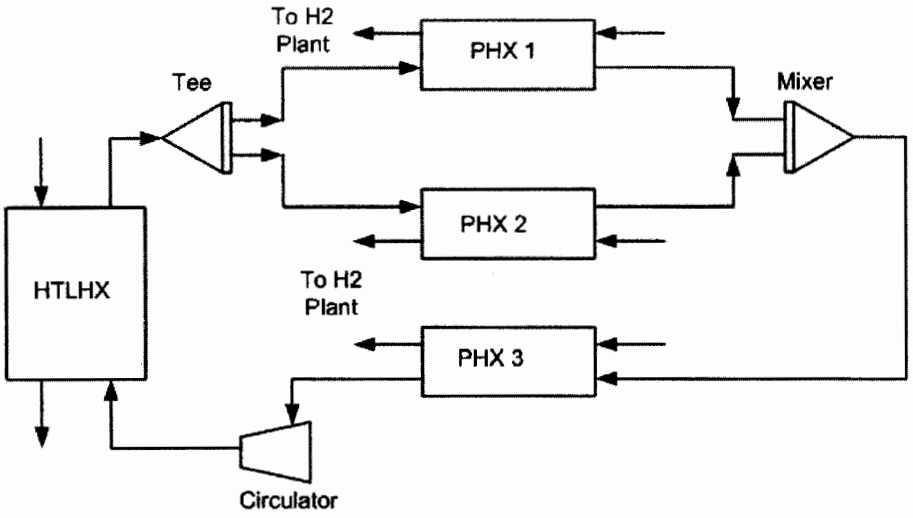


**Figure 3. IHTL process heat exchanger configuration.**

### 3.1.1 Three-Shaft Cycle

The three-shaft configuration, illustrated in Figure 4~~Figure 4~~, consists of: (1) a primary loop, (2) an IHTL in parallel with (3) the PCU with three turbines (high pressure turbine, low pressure turbine and power turbine), four compressors (one low pressure compressor, two medium pressure compressors, and one high pressure compressor), one precooler, three intercoolers, and a recuperator.

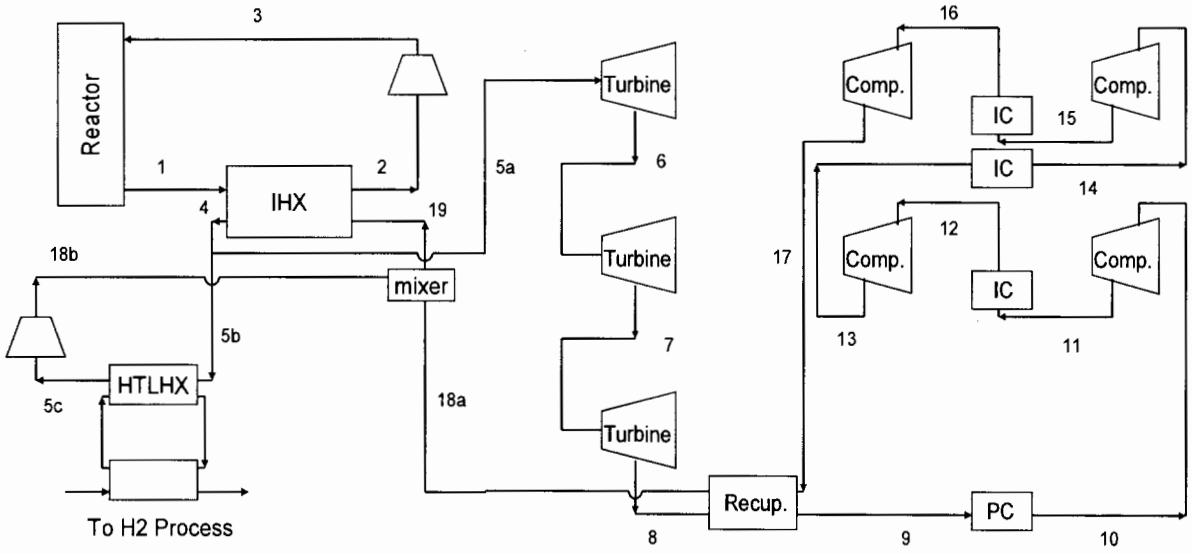


**Figure 4. Schematic of three-shaft cycle PCU configuration.**

### 3.1.2 Combined Cycle

The combined cycle configuration, illustrated in Figure 5~~Figure 5~~, consists of: (1) a primary loop (2) and an IHTL in parallel with (3) a PCU with a gas turbine, a gas compressor, a steam generator, a steam turbine, a condenser, and a pump.

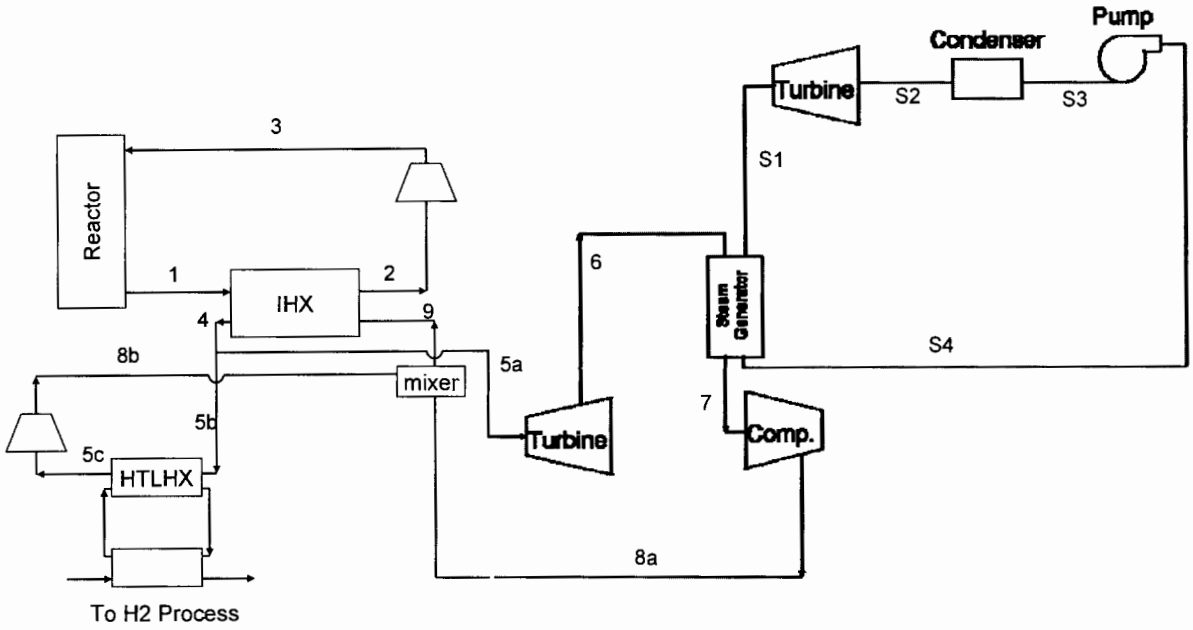


**Figure 5. Schematic of the combined cycle PCU configuration.**

### 3.1.3 Reheated Cycle

The reheat cycle, illustrated in Figure 6~~Figure 6~~ consists of: (1) a primary loop with four IHXs with three used for reheating, (2) an IHTL in series with the IHXs on the primary loop, and (3) the PCU with four turbines (one high pressure turbine, two medium pressure turbines, one low pressure turbine), four compressors (one low pressure compressor, two medium pressure compressors, and one high pressure compressor), one precooler, three intercoolers, and a recuperator.

A reheating option can increase the efficiency of a cycle by increasing the average temperature at which heat is added to the system. This effectively increases the equivalent Carnot temperature for the cycle. However, as more heat exchangers are added to the system the pressure drop increases as well as the cost. There is a trade-off between the efficiency gain due to increasing the average temperature and efficiency loss due to increasing the pressure drop. At some point the pressure drop overwhelms the temperature increase and an efficiency loss is realized. To help alleviate the effects of pressure drop a liquid salt working fluid can be used in the primary side of the cycle. Since the liquid salt is nearly incompressible, the pressure drop in the IHX is very small and assumed to be negligible.

To optimize the efficiency improvement from reheat, the inlet and outlet temperatures for the turbines should be kept the same (Dostal et al. 2004). For a cycle employing an ideal gas, an equal split of total pressure ratio is ideal. Since helium and $CO_2$ are very close to ideal gases in the turbines this same assumption was made in this study.

When using the reheat option, up to four IHXs could be used. This leads to an increase in pumping power required as compared to a single-IHX configuration. The mass flow rate must also be raised for the reheat option to be applicable, also leading to a higher pumping power. To decrease the pumping power required for a helium coolant, a liquid salt, Flibe, was studied as the working fluid.

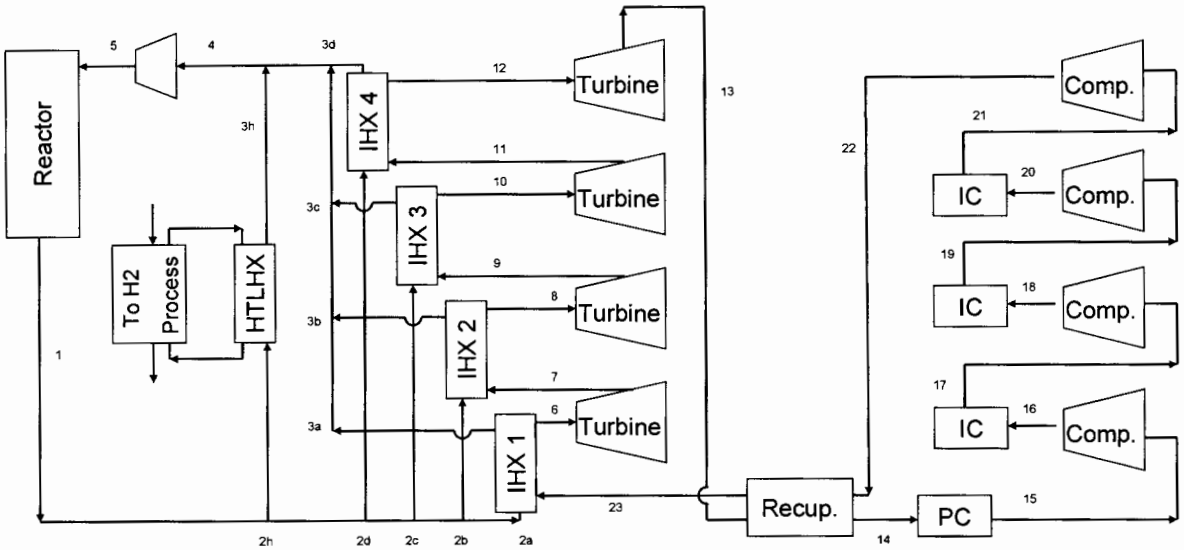


**Figure 6. Schematic of reheated cycle PCU configuration.**

### 3.1.4 HTSE Hydrogen Plant

A next generation high-temperature reactor could be envisioned as a single-purpose facility that produces electricity or hydrogen alone, or as a dual-purposed facility that produces both electricity and hydrogen. To act as a dual-purpose facility, a PCU and a hydrogen production plant must be coupled to the reactor. In this study a baseline HTSE plant will be coupled to the reactor by means of the IHTL. The HTSE model used here was adapted from the work done by Stoots et al. (2005). A model of the HTSE operations was developed at INL that includes all of the components that are actually present in a HTSE plant including pumps, compressors, heat exchangers, expanders and the electrolyzer. A one-dimensional electrolyzer model was developed for the HYSYS modeling code. A comparison of this model with a fully three-dimensional computational fluid dynamic model and experimental results was done by O'Brien et al. (2005).

Referring to Figure 7~~Figure 7~~, the process water enters on the left. The water is then pumped up to the operating pressure of 5 MPa. The efficiency of the pumps and circulators is assumed to be 75%. This water is then combined with water condensate returned from the hydrogen/water product stream. This stream then enters the low temperature recuperator. The pressure drop

through the heat exchangers is assumed to be 20 kPa. From there the steam is further heated by PHX 3. Upon leaving PHX 3 the steam is mixed with hydrogen from the product stream by a recirculator which works to overcome the pressure drops in the system. A mole fraction of 90% water and 10% hydrogen is maintained in this model. This hydrogen helps to maintain reducing conditions at the electrolysis stack to prevent oxidation. The mixed stream then enters the high temperature recuperator which takes advantage of the high temperature outlet from the electrolysis stack. The hydrogen/water stream is then heated to the operating temperature for the electrolysis stack, in this case 827 °C, in PHX 1.

The electrolyzer has another inlet stream that contains the sweep gas. This is used to sweep away the oxygen from the electrolysis process. A steam sweep gas is used in this model and enters the plant in the middle-bottom of Figure 7~~Figure 7~~. It is first pumped up to operating pressure and then heated in a heat exchanger using the hot sweep outlet from the electrolyzer. Before it enters the electrolysis stack it is heated to the operating temperature of 827 °C in PHX 2.

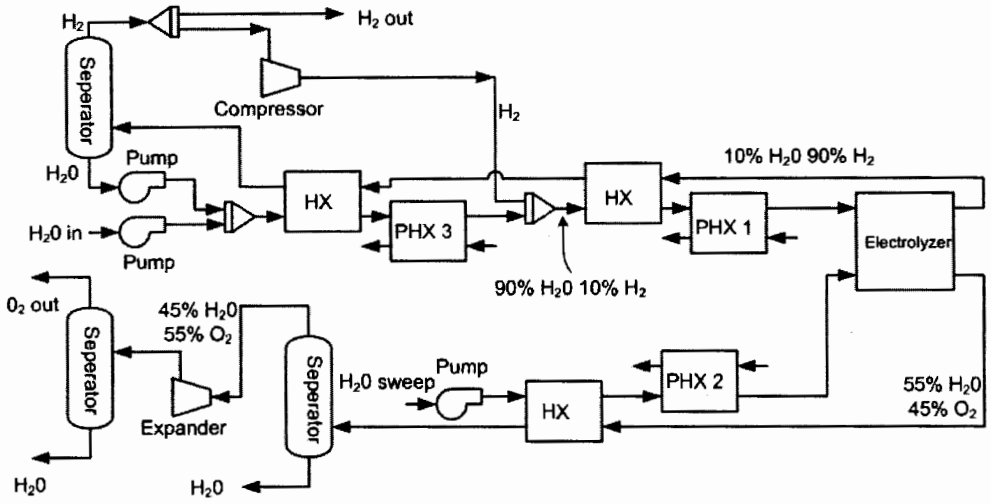


**Figure 7. Schematic of HTSE process.**

Upon leaving the electrolyzer, the product stream is 90% hydrogen and 10% water. This then passes through the high and low temperature recuperators. The steam condensate is then separated from the hydrogen and recycled back into the system. After leaving the electrolyzer, the sweep gas enters the recuperator to preheat the sweep inlet. The sweep outlet contains approximately 55% water and 45% oxygen. It is then partially separated before entering an expander to recuperate some of the power. The expander has an efficiency of 80%. Finally the sweep stream is further separated and high purity oxygen and water are produced.

The model developed by Stoots et al. (2005) was originally envisioned for a 300 MW HTSE plant. However, under the assumption of ~50 MW process heat, a 300 MW plant was not possible. Therefore the plant was scaled down to meet the needs of that assumption. To do this the balance of plant must still work and key working condition such as stream compositions, and electrolyzer inlet temperature must remain constant. This was accomplished by reducing the mass flow of the inlet process stream and the sweep stream while keeping the compositions and temperatures constant. The electrical power to the electrolyzer was reduced from 292 MW to 234.4 MW and 198.8 MW for the helium and liquid salt IHTL working fluids, respectively. This

was done to account for the smaller mass flow rate and to keep an outlet composition of 90% hydrogen and 10% water.

### 3.2 Working Fluids

Helium, $CO_2$, and 80% nitrogen, 20% helium mixture (by weight) were studied to determine the best PCU working fluid in terms cycle efficiency and development cost. Helium is a well understood fluid and has been used in numerous studies pertaining to nuclear power. $CO_2$ has been slow in developing due to material concerns with the fluid. $CO_2$ does possess some advantages over helium such as a higher density allowing for smaller velocities than helium for the same pressure drops (Perry et al. 1984). Despite the lower specific heat, the volumetric flow rates are smaller for $CO_2$ than for a helium cycle generating equivalent power. Therefore, the turbomachinery sizes are smaller for $CO_2$. Copsey et al. (2004) used this nitrogen-helium mixture for the working fluid in a combined cycle.

Helium was used as the working fluid in the primary side of the NGNP for the three-shaft and combined cycles and Flibe was used for the reheated cycle. The Peng-Robinson (1976) equation of state was used by HYSYS to calculate the fluid properties. HYSYS uses a modified NBS method developed by Ely and Hanley (1981 and 1983) to calculate the viscosity and thermal conductivity of the fluids. The values calculated by HYSYS were compared to the NIST database (NIST 2005) and the properties calculated by HYSYS for helium and nitrogen were not in agreement. The HYSYS Simulation Basis Manual (Aspen Technology 2002) recommends that these values be entered as tabulated data for more accurate properties. Therefore, the viscosity and thermal conductivity for helium and nitrogen from the NIST database were entered into HYSYS. HYSYS then performs a regression on the tabular data to get the fluid properties. HYSYS does not contain the properties of the liquid salts used in the primary side of the reheat cycle or the IHTL. This was overcome by entering the fluid properties of the salts in tabular form and allowing HYSYS to perform a regression.

### 3.3 Efficiency Optimization

Using the conditions established in Table 1~~Table 1~~ through 6, the cycles were modeled and optimized in HYSYS. To calculate the efficiency the spreadsheet function of HYSYS was used and values from the cycle were imported from the model. The efficiency of the power conversion unit was calculated as follows

$$\eta_{PCU} = \frac{\Sigma W_T - \Sigma W_C - \Sigma W_{CIR}}{Q_{th} - Q_{IHTL}}, \quad (1)$$

where $\Sigma W_T$ is the total turbine workload, $\Sigma W_C$ is the total compressor workload, $\Sigma W_{CIR}$ is the circulator workload in the primary and secondary side, $Q_{th}$ is the reactor thermal power and $Q_{IHTL}$ is the heat delivered to the IHTL through the HTLHX. The efficiency of the overall cycle including the HTSE plant was calculated as follows

$$\eta_{overall} = \frac{\Sigma W_T - \Sigma W_C - \Sigma W_{CIR} + \Sigma W_{H2} - Q_{EL} + Q_{H2}}{Q_{th}}, \quad (2)$$

where $\Sigma W_{H2}$ is the workload in the HTSE plant, $Q_{EL}$ is the power supplied to the electrolyzer, $Q_{H2}$ is the lower heating value of the produced hydrogen and $Q_{th}$ is the reactor thermal power.

A model to solve for the effectiveness ε of a heat exchanger is not defined in HYSYS and had to be developed. The effectiveness of a heat exchanger is defined as the ratio of the actual heat transfer rate to the maximum heat transfer rate. The spreadsheet function was used and the following equations were input:

$$\varepsilon = \frac{q}{q_{\max}} \tag{3}$$

$$q_{\max} = C_{\min}(T_{h,i} - T_{c,i}) \tag{4}$$

Where $C_{min}$ refers to the smaller of $C_{hot}$ or $C_{cold}$.

$$C_{hot} = c_{p,hot}\dot{m}_{hot} \tag{5}$$

$$C_{cold} = c_{p,cold}\dot{m}_{cold} \tag{6}$$

The log mean temperature difference (LMTD) and the minimum approach were calculated by HYSYS and used to determine heat exchanger performance. The effectiveness, LMTD, and minimum approach served as limits to the allowable working conditions within the cycle. An acceptable effectiveness, LMTD and minimum approach for each heat exchanger were determined and the working conditions were set to take advantage of these limits in order to maximize efficiency. The limits imposed on the cycles are summarized in Tables 4 through 6. The pressure drop for each heat exchanger was calculated using the methods described in Section 3.4.

The polytropic efficiency of the turbomachinery was used for efficiency calculation rather than the isentropic efficiency. The polytropic efficiencies for the turbines and the compressors were assumed to be 92% and 90%, respectively. These values are representative of expected efficiency that will be available for the NGNP project. For expansion the efficiency is calculated from

$$\frac{T_{0,ex}}{T_{0,in}} = \left(\frac{P_{0,ex}}{P_{0,in}}\right)^{\left(\frac{R}{C_p}\eta_{p,e}\right)}, \tag{7}$$

where $T_0$ is the stagnation temperature, $P_0$ is the stagnation pressure, R is the gas constant, $C_p$ is the specific heat, $\eta_{p,e}$ is the polytropic efficiency and the subscripts *in* and *ex* refer to the inlet and exit conditions. For compression, the efficiency is calculated as

$$\frac{T_{0,ex}}{T_{0,in}} = \left(\frac{P_{0,ex}}{P_{0,in}}\right)^{\left(\frac{R}{C_p}\frac{1}{\eta_{p,c}}\right)}. \tag{8}$$

Once the working conditions and limits were set the cycle pressure ratios were optimized. For the combined cycle the mass split between the PCU and HTLHX was also optimized.

**Table 4. Cycle conditions for three-shaft configuration.**

| Parameter | Nominal Value |
|---|---|
| IHX cold-side outlet temp, °C | 885 |
| IHX effectiveness limit | <97% |
| IHX temperature pinch limit, °C | 5 |
| IHX LMTD, °C | 15 |
| Compressor outlet pressure, MPa | 7.05 |
| Precooler outlet temperature, °C | 30 |
| Recuperator effectiveness | 95% |
| HTLHX effectiveness limit | <97% |
| HTLHX temperature pinch limit, °C | 5 |
| HTLHX LMTD, °C | 27 |

**Table 5. Cycle conditions for combined configuration.**

| Parameter | Nominal Value |
|---|---|
| IHX cold-side outlet temp, °C | 885 |
| IHX effectiveness limit | <97% |
| IHX temperature pinch limit, °C | 5 |
| IHX LMTD, °C | 15 |
| Compressor outlet pressure, MPa | 7.05 |
| Precooler outlet temperature, °C | 30 |
| Recuperator effectiveness | 95% |
| HTLHX effectiveness limit | <97% |
| HTLHX temperature pinch limit, °C | 5 |
| HTLHX LMTD, °C | 27 |
| steam generator temperature pinch, °C | 5 |
| Steam turbine outlet quality | >85% |
| Steam turbine outlet pressure, kPa | 20 |
| Pump outlet pressure, MPa | 15 |

**Table 6. Cycle conditions for the reheated configuration.**

| Parameter | Nominal Value |
|---|---|
| IHX cold-side outlet temp, °C | 885 |
| IHX effectiveness limit | <97% |
| IHX temperature pinch limit, °C | 5 |
| IHX LMTD, °C | 15 |
| Compressor outlet pressure, MPa | 7.05 |
| Precooler outlet temperature, °C | 30 |
| Recuperator effectiveness | 95% |
| HTLHX effectiveness limit | <97% |
| HTLHX temperature pinch limit, °C | 5 |
| HTLHX LMTD, °C | 27 |

## 3.4 Component Sizing and Pressure Drops

Once the cycle efficiencies had been calculated the relative sizes of the turbomachinery and heat exchangers were estimated. The actual size of the turbomachinery was not calculated but rather parameters that gave some indication to their relative size. The volume of the heat exchangers was calculated.

HYSYS was used to calculate the energy output of the turbines as well as the energy needed for each compressor. The energy required for each component gives some indication of the size of the component. These relative energies were compared to determine the relative size of the turbomachinery.

To determine the relative sizes of the heat exchanger, the UA values (overall heat transfer coefficient times the heat transfer area) of the heat exchangers were calculated by HYSYS. The U values were calculated, the heat transfer areas were determined, and the heat exchanger volume was calculated. This gives a relative estimation of the heat exchanger sizes for the different configurations.

The IHX, HTLHX, and recuperator were assumed to be printed circuit heat exchangers (PCHE) as designed by Heatric (2005). PCHE are composed of channels chemically etched into plates. The plates are then stacked and diffusion bonded together and headers are attached to form the heat exchanger. For this study Alloy 617 was used as the construction material for the heat exchangers. The thermal conductivity was assumed to be constant over the length of the heat exchangers and was obtained from www.specialmetals.com. The heat exchangers are assumed to be in counter flow to reduce the required surface area. The width and height of the heat exchangers were assumed to be equal. The flow channels are assumed to be semicircular with a diameter of 3 mm, which is a representative value. From the stress analysis by Davis et al. (2005), the pitch to diameter ratio was taken as 1.2 and the plate thickness to diameter ratio was taken as 0.57 for the IHX based on a maximum hot side pressure of 7 MPa and a minimum cold side pressure of 5 MPa. For the HTLHX and the recuperator, the pitch to diameter ratio was assumed as 1.7 and the plate thickness to diameter ratio was assumed as 1.19 based on a maximum pressure of 7 MPa on one side and a minimum of 2 MPa on the other.

The overall heat transfer coefficient for was calculated as

$$U = \left( 1/h_{hot} + 1/h_{cold} + t_{avg}/k_{metal} \right)^{-1}, \tag{9}$$

where $h_{hot}$ is the heat transfer coefficient for the hot channels, $h_{cold}$ is the heat transfer coefficient for the cold channels, $t_{avg}$ is the average thickness of the plates and $k_{metal}$ is the thermal conductivity of the metal. The heat transfer coefficients were calculated using the Dittus-Boelter correlation with a leading coefficient of 0.021, which is appropriate for turbulent flow of a gas (INEEL 2003),

$$Nu = 0.021 \mathrm{Re}^{0.8} \mathrm{Pr}^{0.4} \tag{10}$$

where

$$Nu = h \frac{D_{hy}}{k}. \tag{11}$$

For laminar flow, the heat transfer coefficients were calculated from the exact solution for fully developed flow with constant heat rate (Kayes and Crawford 1980),

$$Nu = 4.364. \tag{12}$$

The pressure drops in the heat exchangers were assumed to come from friction losses and were calculated using the following equation:

$$\Delta p = f \frac{L}{D_{hy}} \frac{G^2}{2\rho}, \tag{13}$$

where f is the friction factor, L is the length, $D_{hy}$ is the hydraulic diameter of the channels, $\rho$ is the density, and v is the velocity. The friction factor was determined using a correlation for turbulent and laminar flow. For turbulent flow f was calculated using

$$f = \frac{0.3164}{\mathrm{Re}^{.25}}, \tag{14}$$

and for laminar flow

$$f = \frac{64}{\mathrm{Re}}. \tag{15}$$

The sizing algorithm for the heat exchangers was adapted from the work by Davis et al. (2005) and entered into the spreadsheet function of HYSYS. The width, height, and pressure drops were assumed for the heat exchangers. Using the assumed channel diameter, pitch and thickness, the flow areas of the hot and cold streams were calculated. The values for $\rho$, $\mu$, k, $c_p$ and $\dot{m}$ for the inlet and outlet were obtained from HYSYS and averaged for the hot and cold side. The Reynolds number,

Prandlt number, heat transfer coefficient and friction factor were then calculated for the hot and cold sides. The overall heat transfer coefficient was then calculated. The heat transfer area was then calculated by dividing the UA value given by HYSYS by the calculated heat transfer coefficient. The length of the heat exchanger is then calculated from the heat transfer area and the wetted perimeter of the channels. Using the length the pressure drops can then be calculated. For each heat exchanger one pressure drop was assumed to be constant. For the IHX the hot side pressure drop was assumed to be 0.05 MPa, for the HTLHX the cold side pressure drop was assumed to be 0.139 MPa, and for the recuperator the hot side pressure drop was assumed to be 0.100 MPa. Next the width and height were adjusted to match the set pressure drops in the heat exchangers and the remaining pressure drops were calculated. Finally the input values for the remaining pressure drops were adjusted to match the calculated pressure drops. Once the pressure drops were obtained the volume of the heat exchangers were calculated.

The steam generator was assumed to be a counter flow shell and tube heat exchanger. For the steam generator the Brayton cycle working fluid was on the shell side and the Rankine cycle working fluid was on the tube side. Since the Brayton cycle working pressure, 7 MPa, is lower than that for the Rankine cycle, 15 MPa, the pressure boundary requirements on the shell will be reduced. Because the diameter of the tubes is small, normal tube thicknesses can endure the high pressure. A shell diameter of 4.5 m, an inner and outer diameter of 6 mm and 7.3 mm for the tubes, a pitch to outer diameter ratio of 1.3 and a triangular array were assumed for the steam generator. These values are typical of existing steam generator designs. Again Alloy 617 was used for the construction material of the steam generator.

The overall heat transfer coefficient was calculated as (Bird et al. 1960)

$$U = \left( 1/h_{cold} + d_{out}/2k_{metal} \ln\left( d_{out}/d_{in} \right) + d_{out}/d_{in} h_{hot} \right)^{-1}, \tag{16}$$

where $h_{hot}$ is the heat transfer coefficient for the hot channels, $h_{cold}$ is the heat transfer coefficient for the cold channels, $k_{metal}$ is the thermal conductivity of the metal and $d_{in}$ and $d_{out}$ are the inner and outer diameters of the tubes. The heat transfer coefficient on the hot side was calculated using Equation 10 for turbulent flow and for laminar flow Equation 12 was used.

To account for the phase change in the cold side the steam generator was divided into four heat transfer regions: subcooled, nucleate boiling, post critical heat flux and superheated. On the hot side there is no phase change and Equations 10 and 12 were used to calculate the heat transfer coefficient and Equations 13-15 were used for the pressure drop calculations.

The subcooled region begins at the inlet to the steam generator and ends where the water reaches saturation conditions. Here we have neglected subcooled boiling. Since this region is single phase flow, Equations 10-15 were used for the heat transfer coefficient and pressure drop calculations.

The nucleate boiling region begins at the saturation point and ends where the fluid reaches critical quality. The Chen correlation was used in this region to determine the convection heat transfer coefficient. Chen assumes that the total convection coefficient in this region can be thought of as the superposition of the convection and nucleate boiling heat transfer coefficient (Collier and Thome, 1994),

$$h_{2\phi} = h_c + h_{NB}\,. \tag{17}$$

Chen assumed that the convective component, $h_c$, could be represented by a Dittus-Boelter type equation.

$$h_c = .023\left(\frac{G(1-x)D_{hy}}{\mu_f}\right)^{0.8}\left(\frac{\mu c_p}{k}\right)_f^{0.4}\left(\frac{k_f}{D_{hy}}\right)F\,, \tag{18}$$

where F is an additional correction factor defined as,

$$F = \left(\frac{\mathrm{Re}_{2\phi}}{\mathrm{Re}_f}\right)^{0.8}\,. \tag{19}$$

Chen originally determined F empirically; however he later derived F using a Reynolds analogy as follows,

$$F = \left(\phi_f^2\right)^{0.444}\,. \tag{20}$$

Here $\phi_f^2$ is the two phase friction multiplier based on the pressure gradient from fluid alone. Using the Martinelli parameter $\phi_f^2$ is defined as,

$$\phi_f^2 = 1 + \frac{C}{X} + \frac{1}{X^2}\,, \tag{21}$$

where C = 20 for turbulent-turbulent flow. The Martinelli parameter is based on the fluid properties at the saturation point and is defined as,

$$X = \left(\frac{1-x}{x}\right)^{0.9}\left(\frac{\rho_g}{\rho_f}\right)^{0.5}\left(\frac{\mu_f}{\mu_g}\right)^{0.1}\,. \tag{22}$$

The nucleate boiling component of the Chen correlation also uses fluid properties at the saturation point and is defined as,

$$h_{NB} = 0.00122\left[\frac{\left(k^{0.79}c_p^{0.45}\rho^{0.49}\right)_f}{\sigma^{0.5}\mu_f^{0.29}h_{fg}^{0.24}\rho_g^{0.24}}\right]\Delta T_{sat}^{0.24}\Delta p_{sat}^{0.75}S\,, \tag{23}$$

where S is the suppression factor that takes into account the difference between the wall superheat and the mean superheat in the boundary layer. S can be calculated using (MacDonald and Buongiorno 2002),

$$S = \frac{1}{1 + 2.53\times10^{-6}\left(\mathrm{Re}_f F^{1.25}\right)^{1.17}}. \tag{24}$$

The Chen correlation determines the heat transfer coefficient at a point where the local quality is $x$. In this analysis a value of half the critical quality was chosen to give an average heat transfer coefficient over the entire region.

To determine the length and volume of the nucleate boiling region of the heat exchanger, the critical quality must be known. In order to determine the critical quality an iterative process must be implemented. First an initial guess of the critical quality must be made; in this case 0.75 was used. Using this initial guess the tube side heat transfer coefficient is determined along with the universal heat transfer coefficient. Using the ε-NTU method, the heat transfer area is determined. The effectiveness of the heat exchanger in this region was calculated using Equation 2. The NTU value was calculated using,

$$NTU = \frac{1}{C_r - 1}\ln\left(\frac{\varepsilon - 1}{\varepsilon C_r - 1}\right) \qquad C_r < 1 \tag{25}$$

$$NTU = \frac{\varepsilon}{1-\varepsilon} \qquad C_r = 1 \tag{26}$$

where $C_r = C_{min}/C_{max}$.

Next the heat transfer area and the length were calculated,

$$A = \frac{NTU}{U}C_{\min} \tag{27}$$

$$l = \frac{A}{\pi d_{in} N_t} \tag{28}$$

where $d_{in}$ is the inside diameter of the tubes and $N_t$ is the number of tubes in the heat exchanger. The number of tubes is given by the follow formula,

$$N_t = \frac{d_{in,shell}^2 \pi}{4p^2 \sin\left(\pi/3\right)}. \tag{29}$$

where $d_{in,shell}$ is the inner diameter of the shell and $p$ is the pitch. The length is then inserted into the CISE-4 correlation and a new critical quality is calculated and reiterated until it converges. The CISE-4 correlation is given by Todreas and Kazimi (1990),

$$x_{crit} = \frac{a_{CISE4} l_{crit}}{l_{crit} + b_{CISE4}} \tag{30}$$

$$a_{CISE4} = \frac{1}{1+1.481\times10^{-4}\left(1-\frac{p}{p_c}\right)^{-3} G} \qquad G < G^* \tag{31}$$

$$a_{CISE4} = \frac{1-\frac{p}{p_c}}{\left(\frac{G}{1000}\right)^{1/3}} \qquad G < G^* \tag{32}$$

$$b_{CISE4} = 0.199\left(\frac{p_c}{p}-1\right)^{0.4} G^* d_{in,tube}^{0.4} \tag{33}$$

$$G^* = 3375\left(1-\frac{p_c}{p}\right)^3 \tag{34}$$

where $p_c$ is the critical pressure of water. The pressure drop calculation was performed by multiplying the pressure drop calculated assuming that the total fluid was liquid, $\Delta p_{fo}$, and then multiplying by a two phase friction multiplier, $\phi_{fo}^2$.

$$\Delta p = \Delta p_{fo}\phi_{fo}^2 \tag{35}$$

$$\Delta p = f_{fo}\frac{L}{D_{hy}}\frac{G^2}{2\rho_f} \tag{36}$$

Collier and Thome (1994) recommend the Friedel correlation for the two phase friction multiplier for flows where,

$\mu_f / \mu_g < 1000$.

The Friedel correlation is given in Collier and Thome (1994) as,

$$\phi_{fo}^2 = A_1 + \frac{3.24 A_2 A_3}{Fr^{0.045} We^{0.035}} \tag{37}$$

where

$$A_1 = (1-x)^2 + x^2\left(\frac{\rho_f f_{go}}{\rho_g f_{fo}}\right) \tag{38}$$

$$A_2 = x^{0.78}(1-x)^{0.224} \tag{39}$$

$$A_3 = \left(\frac{\rho_f}{\rho_g}\right)^{0.91}\left(\frac{\mu_g}{\mu_f}\right)^{0.19}\left(1-\frac{\mu_g}{\mu_f}\right)^{.7} \tag{40}$$

$$Fr = \frac{G^2}{gD\overline{\rho}^2} \tag{41}$$

$$We = \frac{G^2 D}{\overline{\rho}\sigma} \tag{42}$$

In the post critical heat flux region which ranges from dry-out to saturation, the Groeneveld correlation was used. This is a common method used in calculating the heat transfer in the region (MacDonald and Buongiorno, 2002) and is given by the following equation,

$$Nu = 0.00109\left\{\mathrm{Re}_g\left[x+\frac{\rho_g}{\rho_f}(1-x)\right]\right\}^{0.989}\mathrm{Pr}_g^{1.41}\,Y \tag{43}$$

$$Y = \left[1-0.1\left(\frac{\rho_f-\rho_g}{\rho_g}\right)^{0.4}(1-x)^{0.4}\right]^{-1.15}. \tag{44}$$

Again an average quality is used to give an average heat transfer coefficient over the region. The pressure drop calculation in the region was performed using the Friedel correlation that was used in the nucleate boiling region.

For the superheat region the heat transfer becomes single phase and Equations 10-15 were used to calculate the heat transfer coefficient and the pressure drop. Average properties were used to calculate the heat transfer coefficient and the pressure drop.

A similar algorithm as before was used in the steam generator sizing. Using the assumed shell diameter, tube inner and outer diameter, pitch, triangular array and pressure drops the overall heat transfer coefficient and heat transfer area were found for each heat transfer region. The length of each region was then obtained from the heat transfer area and the shell diameter. The hot and cold side pressure drops were then calculated. The pressure drop was then iterated until the input and output values converged. Once all the regions were solved the total volume and pressure drop in the steam generator was calculated by summing the volume and pressure drops from each region.

### 3.5 Parametric Studies

Parametric studies away from the baseline values of the systems were performed on the three-shaft and combined cycles to determine the effect of varying conditions in the cycle. This gives some

insight into the sensitivity of these cycles to various operating. The parametric studies were carried out by isolating and varying a single working condition. Once the working condition was changed the cycle was optimized using the methods discussed in Section 3.3.

### 3.5.1 Reactor outlet temperature

The reactor outlet temperature for the NGNP is limited by material concerns. Current designs such as the Arbeitsgemeinschaft Versuchsreactok (AVR) have been operating at reactor outlet temperatures of 950°C. The Chinese HTR-10 was design to operate up to 950°C to investigate diverse power generation systems (e.g. gas turbine) and nuclear process heat applications. With current materials reactor outlet temperatures up to 1000°C can be realized, but with a limited lifetime of 15 to 20 years (*Generation IV Roadmap* 2001). Reactor outlet temperature was studied to determine the efficiency increase gained by using these higher temperatures. The reactor outlet temperature was varied from 900°C to 1000°C. At each reactor outlet temperature the cycles were optimized and were resized. However, the heat exchangers could not be easily resized if the reactor outlet temperature was raised after the plant had been constructed.

### 3.5.2 Mass flow

The mass flow was varied between 85-100%. The cycles were optimized at the lower flow rates, but the heat exchangers were not resized.

### 3.5.3 Pressure

The pressure in the secondary side was studied to establish the effects running the cycle at a lower pressure. The pressure was varied between 2 MPa and 7 MPa for the 3 configurations. The cycles were optimized at each pressure. The heat exchangers were resized to give the optimal plant design.

### 3.5.4 Turbine cooling

In high temperature systems turbine cooling may be needed prolong the life of the turbines. This is done by splitting the outlet flow of the high temperature compressor. Most of the flow continues through the cycle while a fraction goes towards cooling the turbines. The split flow then cools the turbines and returns to the main flow inside the turbine (Saravanamuttoo 1996).

A simplified model of turbine cooling was used to model the process. A single-stage turbine with cooling of the disc, stator blades and rotor blades was assumed. The mass flow to the stator blade and disc cooling add to the work in the turbine while the rotor cooling does not (Saravanamuttoo 1996). It was assumed that since the cooling mass flow was small, the reduction in temperature of the working fluid due to cooling is neglected. Therefore, since the mass flow of the stator blade and disc cooling add to the work and their temperature difference is neglected they can be ignored in the calculation of the turbine work. The rotor cooling can be modeled as a loss of flow through the turbine. The model splits the outlet flow from the high pressure compressor with a small fraction going towards the turbine cooling and the rest continues through the cycle. It was assumed that 4% of the flow was needed for the high temperature turbine and 2% was needed for each additional turbine. This gives 4% for cooling in the combined cycle and 8% for cooling in the three-shaft cycle. Turbine cooling was applied to the configurations, the cycles were optimized and the heat exchangers were resized.

## 4.0 CYCLE ANALYSIS RESULTS

The methods described in Section 3 were applied to the three configurations described previously. The PCU efficiency was calculated for each configuration. Sections 4.1 through 4.3 present the results for the three-shaft, combined and reheated cycles. The effects of the IHTL working fluid and the HTSE plant on total efficiency are presented in Section 4.4.

### 4.1 Three-Shaft Design

The three-shaft configuration is illustrated in Figure 4~~Figure 4~~. The conditions for this loop are summarized in Tables 1 and 3. This cycle was simulated using helium as the working fluid in the primary side of the NGNP and the IHTL. Helium, $CO_2$ and the $N_2$-He mixture were simulated in the PCU. Results are described in Sections 4.1.1, 4.1.2 and 4.1.3, respectively for these three fluids. Section 4.1.4 describes the results from the parametric studies.

A comparison of the working fluids in this cycle shows that helium working fluid produces the highest efficiency. However, it also has relatively large heat exchangers and turbomachinery. Using the $N_2$-He mixture produces a slightly lower efficiency, but results in smaller heat exchangers. The $CO_2$ working fluid has a much lower, approximately 4%, cycle efficiency. Using $CO_2$ results in the largest heat exchangers, but the smallest turbomachinery. Similar results were obtained by Bammert and Klein for the turbomachinery (1974).

#### 4.1.1 Helium Working Fluid

The helium working fluid was optimized for the three-shaft cycle with a pressure ratio of 3.432 and an PCU efficiency of 50.93%. The secondary mass flow rate was optimized at 289 kg/s. The HYSYS simulation is illustrated in Figure ~~Figure~~ 8, the T-S diagram is shown in Figure~~Figure~~ 9 and the state points are summarized in Table ~~Table~~ 7. The total heat exchanger volume was 242.5 $m^3$ and the total cycle work was 800.2 MW. Table 8 lists the individual component sizing results for the cycle.

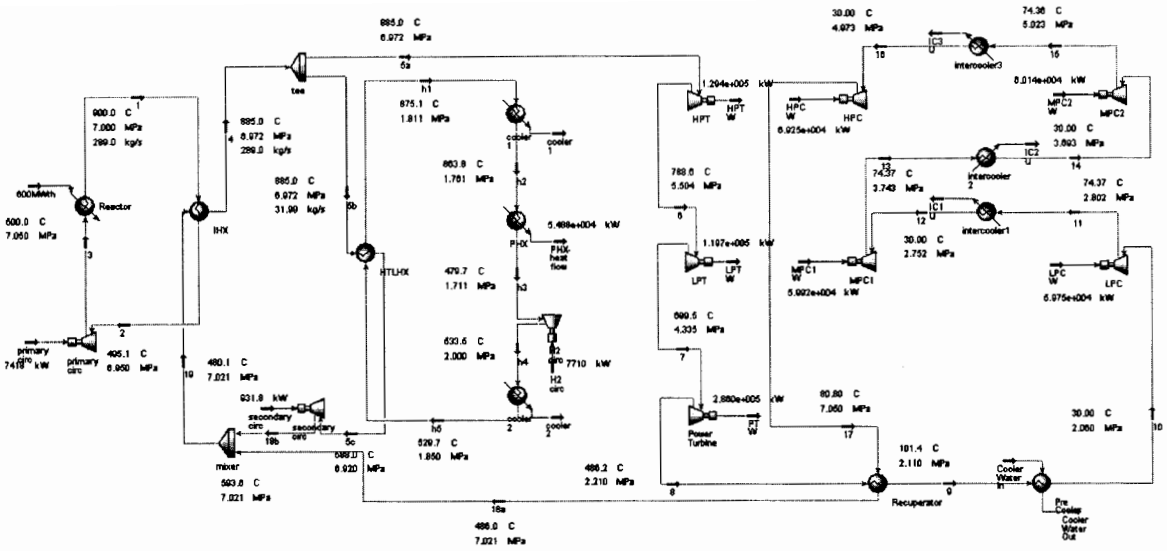

**Figure 8. HYSYS diagram of three-shaft configuration with helium working fluid.**

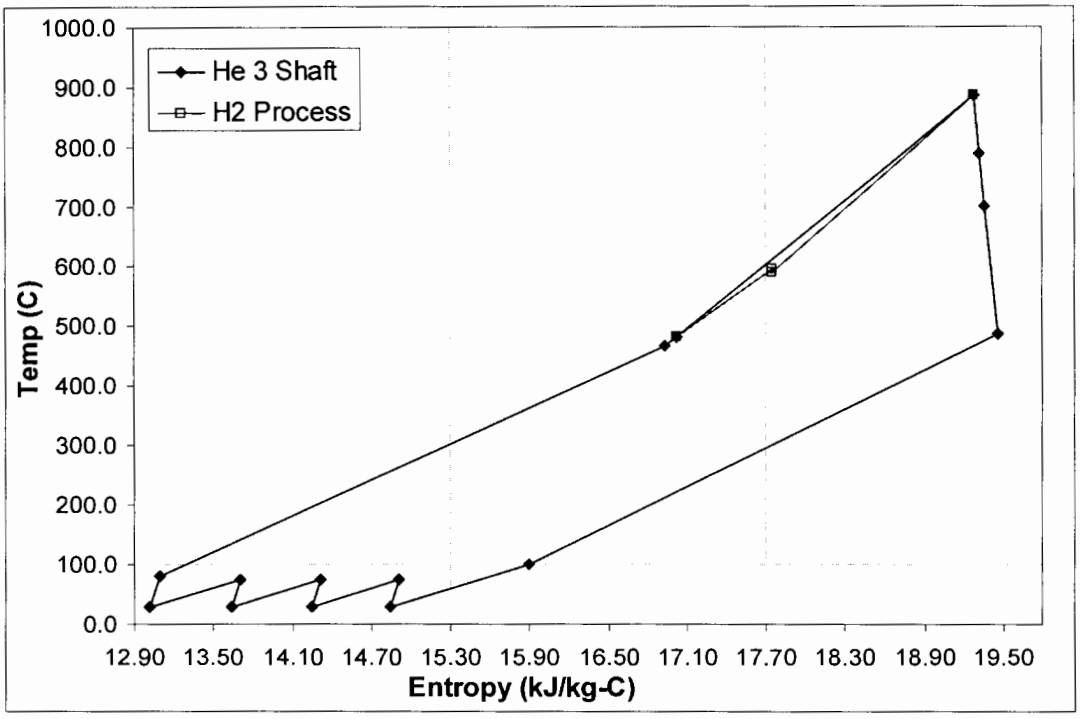


**Figure 9. T-S diagram for three-shaft configuration with helium working fluid.**

**Table 7. State points for three-shaft configuration with helium working fluid.**

| Point | Temp (°C) | Pressure (MPa) | Entropy (kJ/kg-K) | Enthalpy (kJ/kg) |
|---|---|---|---|---|
| 1 | 900.0 | 7.00 | 19.33 | 4561.1 |
| 2 | 495.1 | 6.95 | 17.15 | 2459.0 |
| 3 | 500.0 | 7.05 | 17.16 | 2484.7 |
| 4,5(a,b) | 885.0 | 6.97 | 19.28 | 4483.2 |
| 5c | 588.0 | 6.92 | 17.75 | 2941.3 |
| 6 | 788.6 | 5.50 | 19.32 | 3979.7 |
| 7 | 699.5 | 4.33 | 19.36 | 3514.0 |
| 8 | 486.2 | 2.21 | 19.47 | 2401.3 |
| 9 | 101.4 | 2.11 | 15.89 | 402.6 |
| 10 | 30.0 | 2.06 | 14.84 | 31.7 |
| 11 | 74.4 | 2.80 | 14.92 | 264.2 |
| 12 | 30.0 | 2.75 | 14.24 | 33.7 |
| 13 | 74.4 | 3.74 | 14.32 | 266.8 |
| 14 | 30.0 | 3.69 | 13.63 | 36.3 |
| 15 | 74.4 | 5.02 | 13.71 | 270.3 |
| 16 | 30.0 | 4.97 | 13.02 | 39.8 |
| 17 | 80.8 | 7.05 | 13.10 | 309.3 |
| 18a | 466.0 | 7.02 | 16.93 | 2307.9 |
| 18b | 593.6 | 7.02 | 17.76 | 2970.4 |
| 19 | 480.1 | 7.02 | 17.03 | 2381.3 |

**Table 8. Component sizing data for three-shaft configuration with helium working fluid.**

| Component | Value |
|---|---|
| Turbine work (MW) | 535.0 |
| Compressor work (MW) | 249.1 |
| Circulator work (MW) | 8.4 |
| IHX volume ($m^3$) | 80.5 |
| HTLHX volume ($m^3$) | 9.1 |
| Recuperator volume ($m^3$) | 153 |

### 4.1.2 $CO_2$ Working Fluid

The $CO_2$ working fluid was optimized for the three-shaft cycle with a pressure ratio of 22.57 and an PCU efficiency of 46.73%. The secondary mass flow rate was optimized at 1201 kg/s. The HYSYS simulation is illustrated in Figure 10, the T-S diagram is shown in Figure 11 and the state points are summarized in Table 9. The total heat exchanger volume was 285.2 $m^3$ and the total cycle work was 729.8 MW. Table 10 lists the individual component sizing results for the cycle.

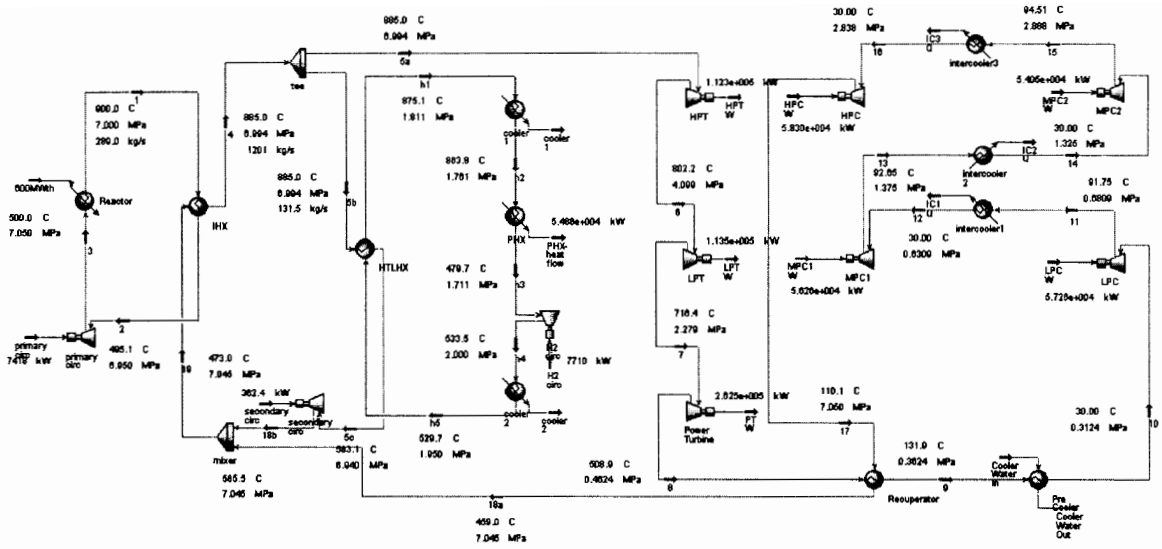

**Figure 10. HYSYS diagram of three-shaft configuration with $CO_2$ working fluid.**

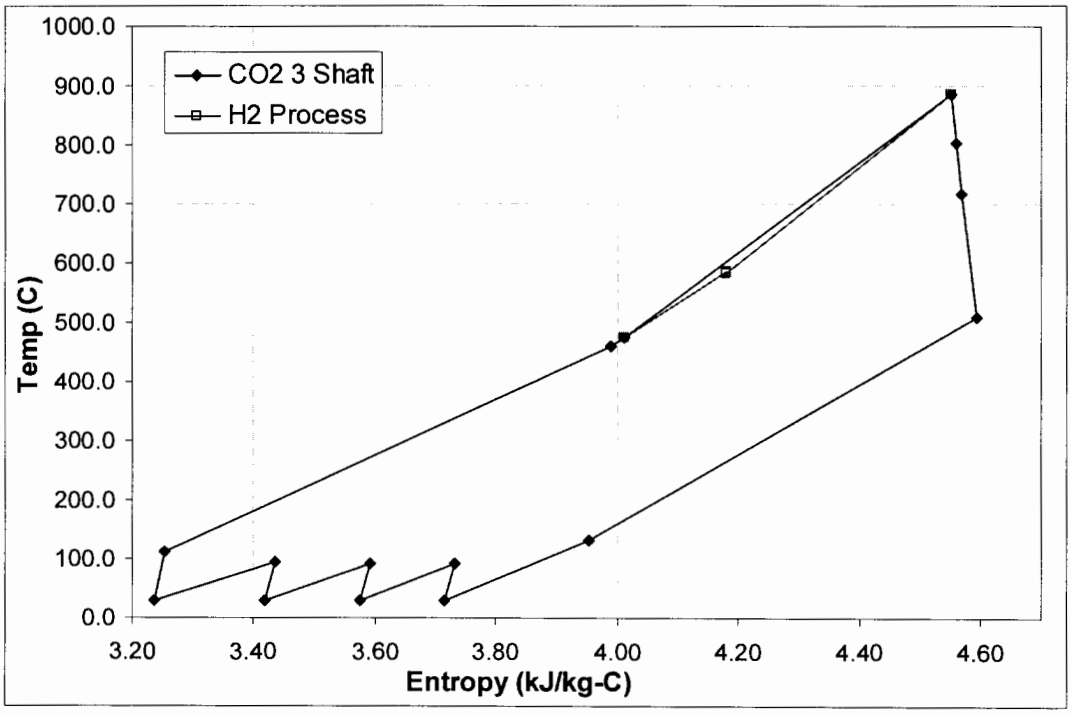


**Figure 11. T-S diagram of three-shaft configuration with $CO_2$ working fluid.**

**Table 9. State points for three-shaft configuration with $CO_2$ working fluid.**

| Point | Temp (°C) | Pressure (MPa) | Entropy (kJ/kg-K) | Enthalpy (kJ/kg) |
|---|---|---|---|---|
| 1 | 900.0 | 7.00 | 19.33 | 4561.1 |
| 2 | 495.1 | 6.95 | 17.15 | 2459.0 |
| 3 | 500.0 | 7.05 | 17.16 | 2484.7 |
| 4,5(a,b) | 885.0 | 6.99 | 4.55 | -7999.0 |
| 5c | 583.1 | 6.94 | 4.18 | -8374.2 |
| 6 | 802.2 | 4.10 | 4.56 | -8104.0 |
| 7 | 716.4 | 2.28 | 4.57 | -8210.1 |
| 8 | 508.9 | 0.46 | 4.59 | -8455.5 |
| 9 | 131.9 | 0.36 | 3.95 | -8852.9 |
| 10 | 30.0 | 0.31 | 3.71 | -8946.3 |
| 11 | 91.7 | 0.68 | 3.73 | -8892.8 |
| 12 | 30.0 | 0.63 | 3.57 | -8949.4 |
| 13 | 92.6 | 1.38 | 3.59 | -8896.8 |
| 14 | 30.0 | 1.33 | 3.42 | -8956.2 |
| 15 | 94.5 | 2.89 | 3.43 | -8905.7 |
| 16 | 30.0 | 2.84 | 3.24 | -8972.8 |
| 17 | 110.1 | 7.05 | 3.25 | -8918.3 |
| 18a | 459.0 | 7.05 | 3.99 | -8521.0 |
| 18b | 585.5 | 7.05 | 4.18 | -8371.5 |
| 19 | 473.0 | 7.05 | 4.01 | -8504.6 |

**Table 10. Component sizing data for three-shaft configuration with $CO_2$ working fluid.**

| Component | Value |
|---|---|
| Turbine work (MW) | 488.3 |
| Compressor work (MW) | 225.9 |
| Circulator work (MW) | 8.1 |
| IHX volume ($m^3$) | 107.3 |
| HTLHX volume ($m^3$) | 11.5 |
| Recuperator volume ($m^3$) | 166.3 |

### 4.1.3 Nitrogen-Helium Working Fluid

The $N_2$-He mixture was optimized for the three-shaft cycle with a pressure ratio of 4.436 and an PCU efficiency of 50.76%. The secondary mass flow rate was optimized at 759 kg/s. The HYSYS simulation is illustrated in Figure 12, the T-S diagram is shown in Figure 13 and the state points are summarized in Table 11. The total heat exchanger volume was 227.7 $m^3$ and the total cycle work was 799.4 MW. Table 12 lists the individual component sizing results for the cycle.

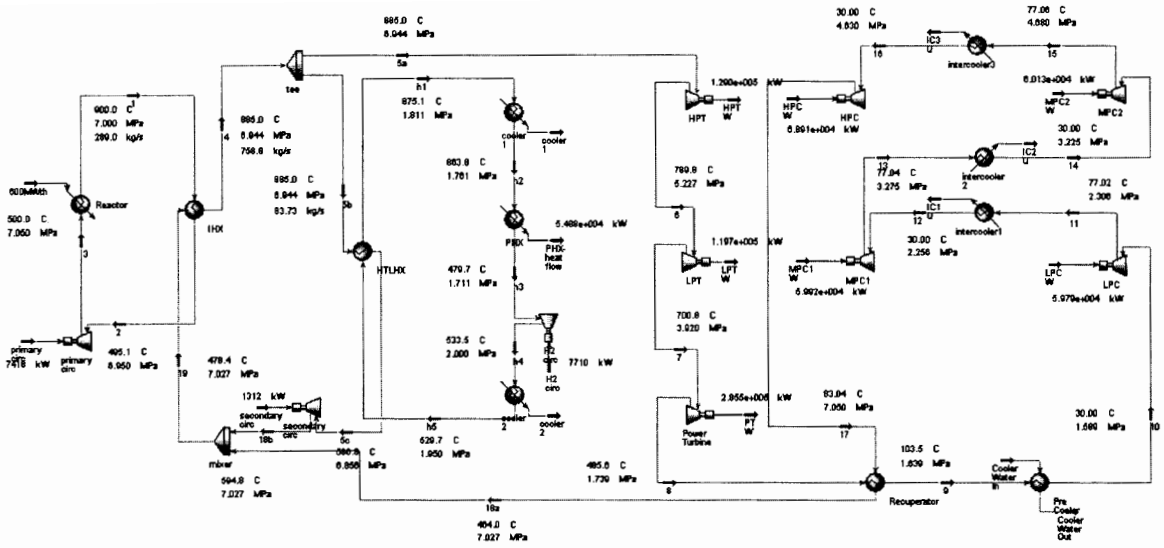

**Figure 12. HYSYS diagram of three-shaft configuration with a nitrogen-helium mixture working fluid.**

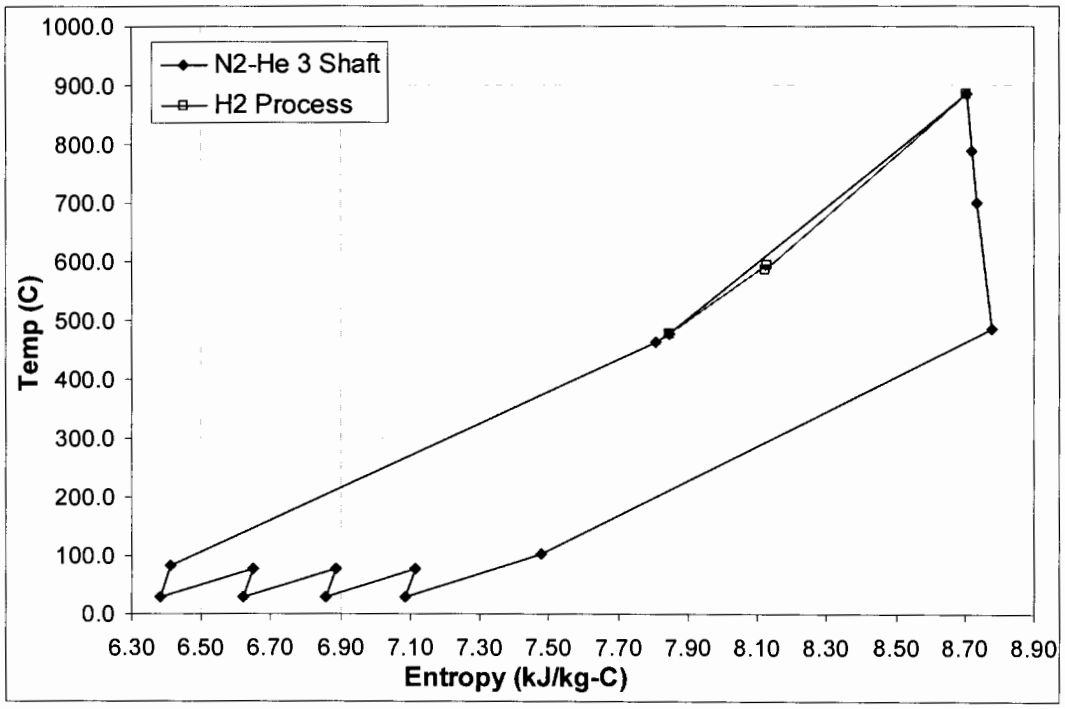


**Figure 13. T-S diagram of three-shaft configuration with a nitrogen-helium mixture working fluid.**

**Table 11. State points for three-shaft configuration with a nitrogen-helium mixture working fluid.**

| Point | Temp (°C) | Pressure (MPa) | Entropy (kJ/kg-K) | Enthalpy (kJ/kg) |
|---|---|---|---|---|
| 1 | 900.0 | 7.00 | 19.33 | 4561.1 |
| 2 | 495.1 | 6.95 | 17.15 | 2459.0 |
| 3 | 500.0 | 7.05 | 17.16 | 2484.7 |
| 4,5(a,b) | 885.0 | 6.94 | 8.71 | 1670.4 |
| 5c | 586.8 | 6.86 | 8.13 | 1081.3 |
| 6 | 789.8 | 5.23 | 8.72 | 1479.2 |
| 7 | 700.8 | 3.92 | 8.74 | 1301.9 |
| 8 | 485.6 | 1.74 | 8.78 | 879.0 |
| 9 | 103.5 | 1.64 | 7.48 | 147.5 |
| 10 | 30.0 | 1.59 | 7.09 | 8.8 |
| 11 | 77.0 | 2.31 | 7.12 | 97.4 |
| 12 | 30.0 | 2.26 | 6.86 | 8.6 |
| 13 | 77.0 | 3.27 | 6.88 | 97.4 |
| 14 | 30.0 | 3.22 | 6.62 | 8.4 |
| 15 | 77.1 | 4.68 | 6.65 | 97.4 |
| 16 | 30.0 | 4.63 | 6.38 | 8.1 |
| 17 | 83.6 | 7.05 | 6.41 | 110.2 |
| 18a | 464.0 | 7.03 | 7.81 | 841.7 |
| 18b | 594.8 | 7.03 | 8.13 | 1096.9 |
| 19 | 478.4 | 7.03 | 7.85 | 869.9 |

**Table 12. Component sizing data for three-shaft configuration with a nitrogen-helium mixture working fluid.**

| Component | Value |
|---|---|
| Turbine work (MW) | 534.2 |
| Compressor work (MW) | 248.7 |
| Circulator work (MW) | 8.7 |
| IHX volume ($m^3$) | 71.4 |
| HTLHX volume ($m^3$) | 8.2 |
| Recuperator volume ($m^3$) | 148.2 |

### 4.1.4 Parametric Studies

Parametric studies were performed on the reactor outlet temperature, secondary mass flow rate, pressure, and turbine for the three working fluids. The results are summarized in Figures 14 through 16 and Table 13. Helium and the $N_2$-He mixture behaved similarly under off-normal working conditions. The off-normal conditions had a greater influence on the $CO_2$. The effect of turbine cooling on the system was an approximately 3% efficiency decrease for all working fluids.

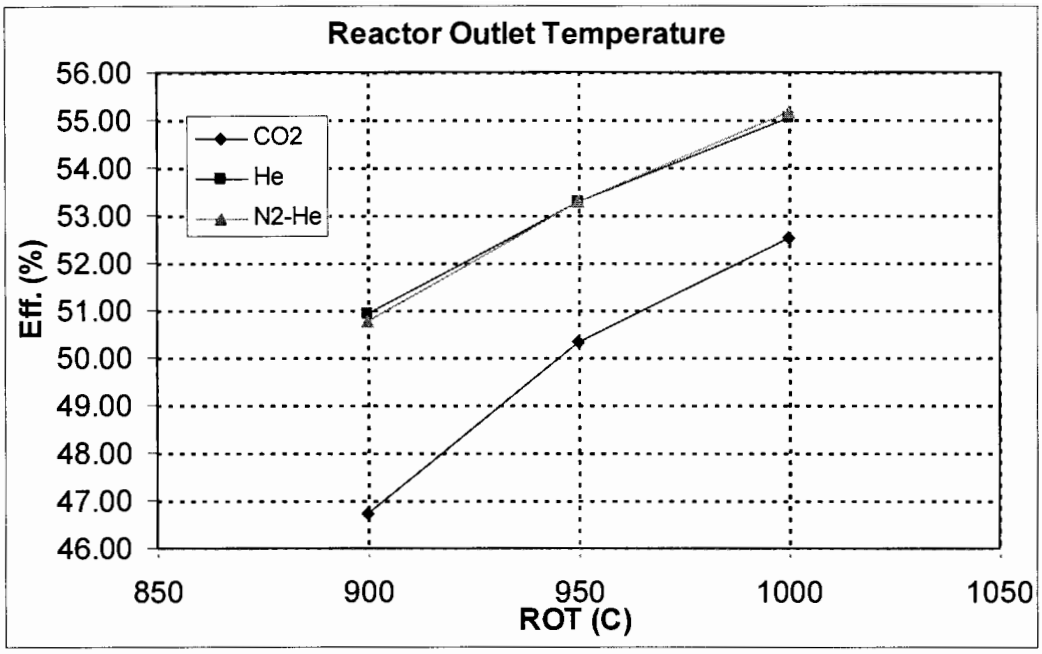


**Figure 14. Parametric study of the effects of reactor outlet temperature on three-shaft cycle efficiency.**

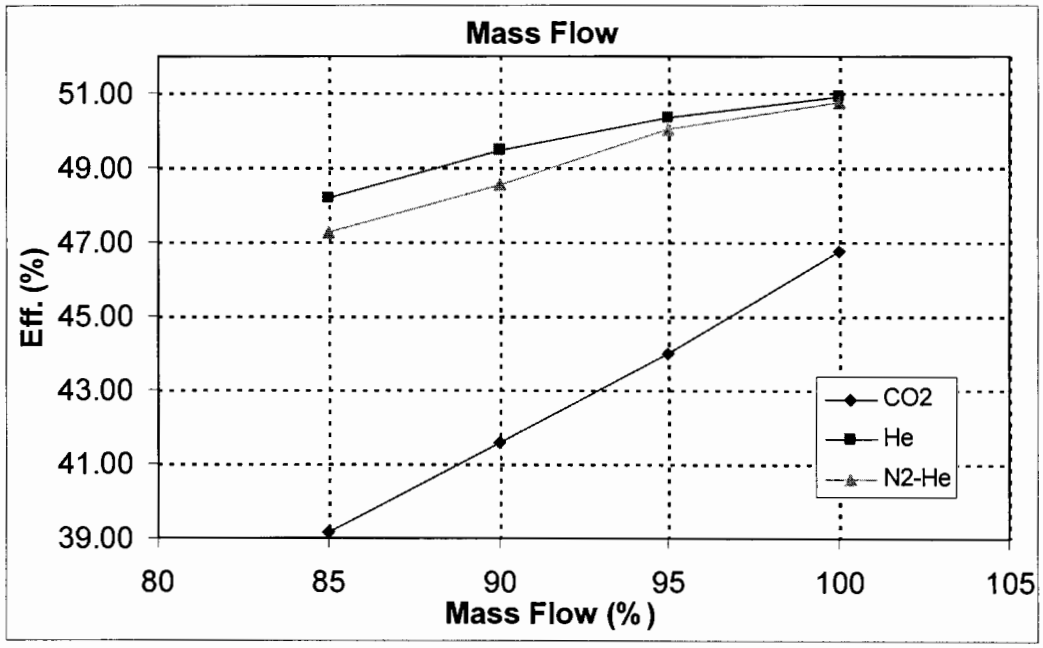


**Figure 15. Parametric study of the effects of secondary mass flow rate on three-shaft cycle efficiency.**

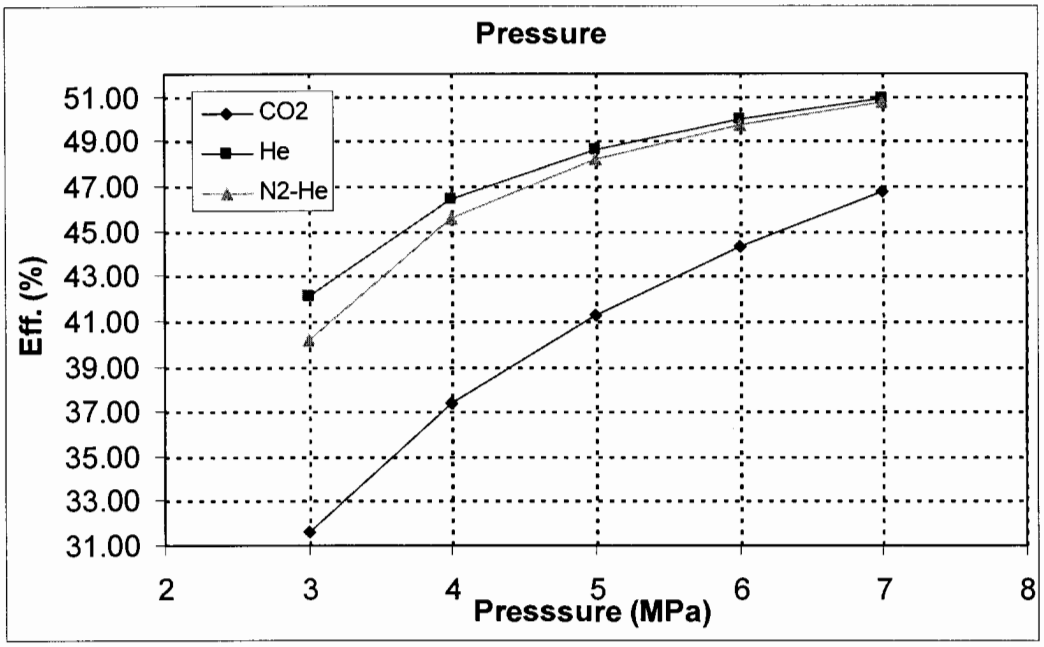


**Figure 16. Parametric study of the effects of working pressure on three-shaft cycle efficiency.**

**Table 13. Parametric study of the effects of turbine cooling on three-shaft cycle efficiency.**

| Turbine Cooling | | | |
|---|---|---|---|
| | CO2 | He | N2-He |
| None | 46.73 | 50.93 | 50.76 |
| 8% | 43.14 | 47.75 | 47.06 |

## 4.2 Combined Cycle

The combined cycle configuration is illustrated in Figure 5~~Figure 5~~. The conditions for this loop are summarized in Tables 1 and 3. This cycle was simulated using helium as the working fluid in the primary side of the NGNP and the INTL. Helium, $CO_2$ and the $N_2$-He mixture were simulated in the PCU. Results are described in Sections 4.2.1, 4.2.2, and 4.2.3, respectively. Section 4.2.4 describes the results from the parametric studies.

The same Rankine bottoming cycle was used for all three working fluids. This cycle gets heat from the Brayton cycle through a steam generator located between the gas turbine and compressor. The steam turbine inlet temperature was set at 575°C to take advantage of the superheat option and keep the turbine outlet quality at 85%. A T-S diagram of the cycle is illustrated in Figure 17 and the state points are summarized in Table 14.

A comparison of the working fluids in this cycle shows that the $CO_2$ working fluid produces the highest efficiency, the smallest turbomachinery, but the largest total heat exchanger volume. Helium and the $N_2$-He mixture produced similar turbomachinery sizes. A slightly higher efficiency was obtained with helium, but the total heat exchanger volume was smaller with the $N_2$-He mixture.

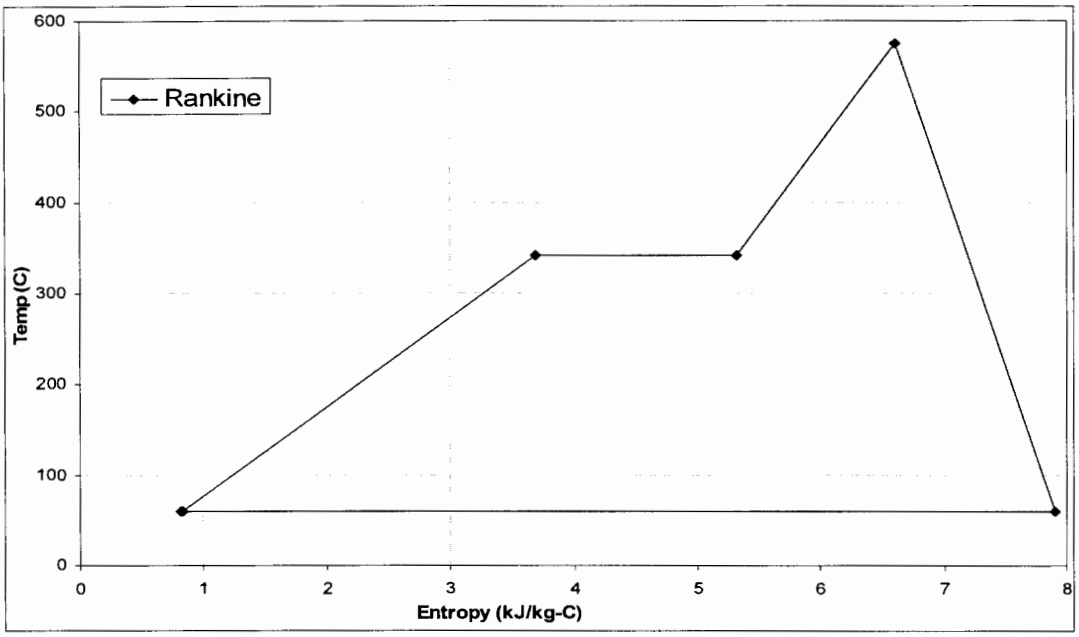


**Figure 17. T-S diagram for Rankine bottoming cycle.**

**Table 14. State points for Rankine bottoming cycle.**

| Point | Temp (°C) | Pressure (MPa) | Entropy (kJ/kg-K) | Enthalpy (kJ/kg) |
|---|---|---|---|---|
| S1 | 575.0 | 15.00 | 9.27 | -12428.8 |
| S2 | 60.2 | 0.02 | 9.52 | -13671.8 |
| S3 | 59.0 | 0.02 | 3.45 | -15695.9 |
| S4 | 59.8 | 15.00 | 3.44 | -15678.9 |

### 4.2.1 Helium Working Fluid

The helium working fluid was optimized for the combined cycle with a pressure ratio of 2.281 and an efficiency of 49.10%. The secondary mass flow rate was optimized at 289 kg/s. The HYSYS simulation is illustrated in Figure 18, the T-S diagram is shown in Figure 19 and the state points are summarized in Table 15. The total heat exchanger volume was 216.0 $m^3$ and the total cycle work was 700.1 MW. Table 16 lists the individual component sizing results for the cycle.

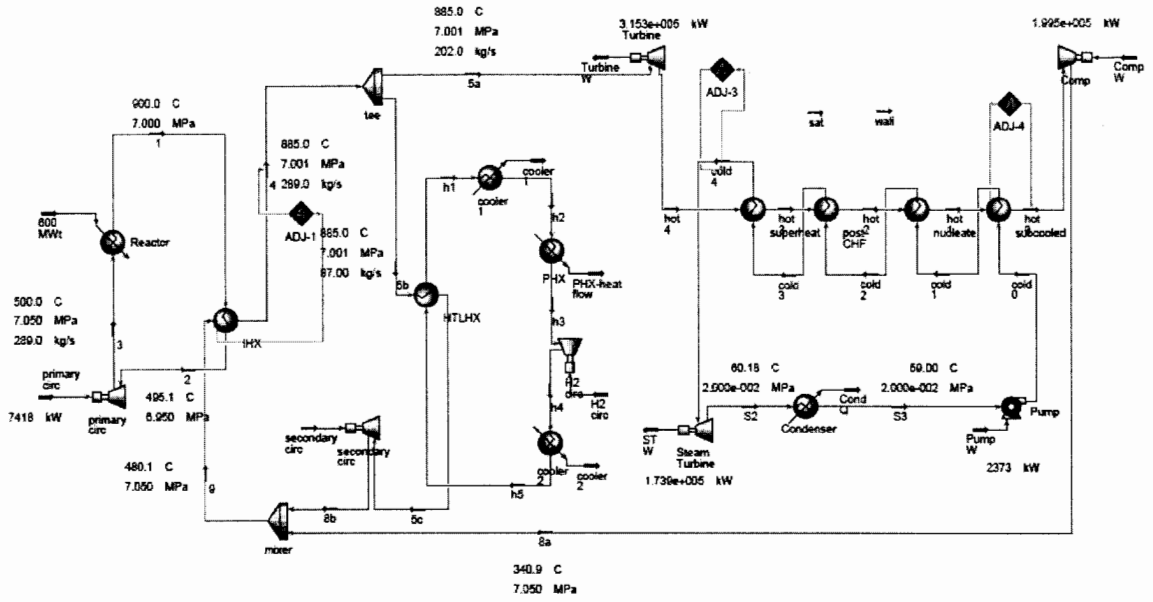


**Figure 18. HYSYS diagram of the combined cycle with helium working fluid.**

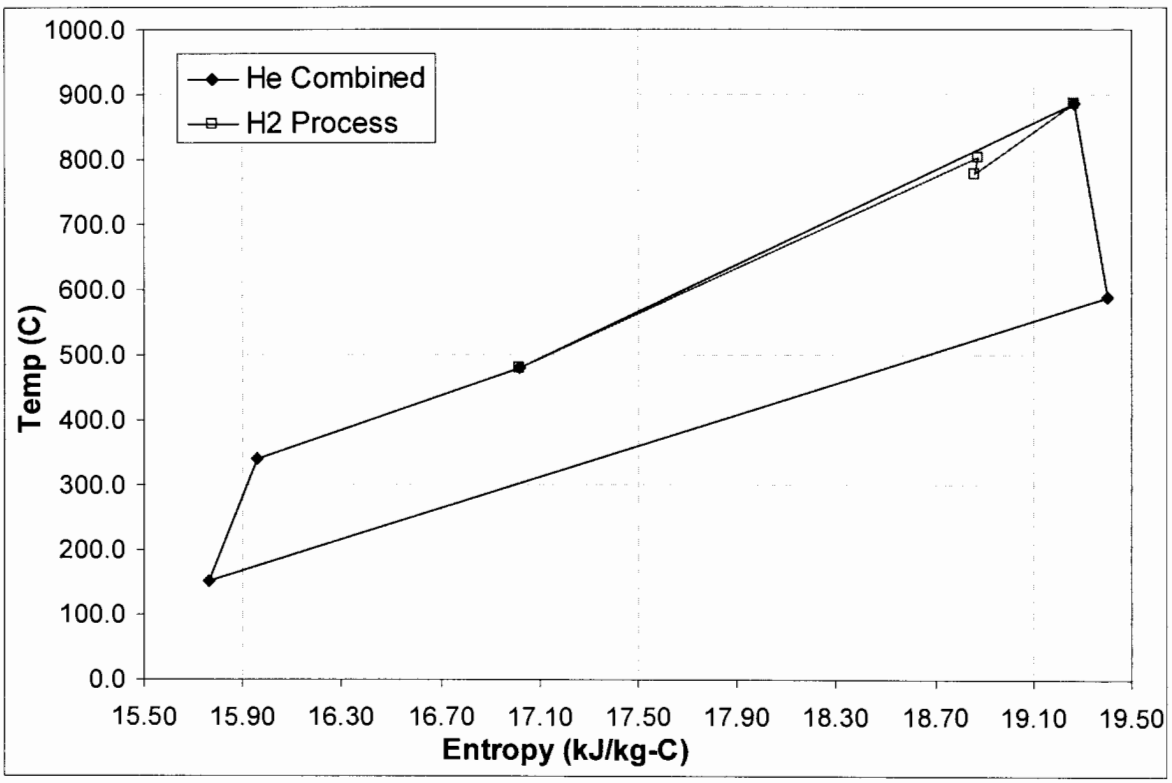


**Figure 19. T-S diagram for combined cycle with helium working fluid.**

**Table 15. State points for Brayton top cycle with helium working fluid.**

| Point | Temp (°C) | Pressure (MPa) | Entropy (kJ/kg-K) | Enthalpy (kJ/kg) |
|---|---|---|---|---|
| 1 | 900.0 | 7.00 | 19.33 | 4561.1 |
| 2 | 495.1 | 6.95 | 17.15 | 2459.0 |
| 3 | 500.0 | 7.05 | 17.16 | 2484.7 |
| 4,5(a,b) | 885.0 | 7.00 | 19.27 | 4483.2 |
| 5c | 775.9 | 6.65 | 18.86 | 3916.3 |
| 6 | 587.5 | 3.12 | 19.40 | 2929.8 |
| 7 | 151.5 | 3.07 | 15.77 | 665.4 |
| 8a | 340.9 | 7.05 | 15.96 | 1658.8 |
| 8b | 803.1 | 7.05 | 18.87 | 4058.3 |
| 9 | 480.1 | 7.05 | 17.02 | 2381.2 |

**Table 16. Component sizing data for combined cycle with helium working fluid.**

| Component | Value |
|---|---|
| Gas Turbine work (MW) | 315.3 |
| Steam Turbine work (MW) | 173.9 |
| Compressor work (MW) | 201.8 |
| Pump work (MW) | 2.4 |
| Circulator work (MW) | 9.4 |
| IHX volume ($m^3$) | 80.4 |
| HTLHX volume ($m^3$) | 1.7 |
| Steam generator volume ($m^3$) | 133.9 |

### 4.2.2 $CO_2$ Working Fluid

The $CO_2$ working fluid was optimized for the combined cycle with a pressure ratio of 7.62 and a PCU efficiency of 50.50%. The secondary mass flow rate was optimized at 1113 kg/s. The HYSYS simulation is illustrated in Figure 20, the T-S diagram is shown in Figure 21 and the state points are summarized in Table 17. The total heat exchanger volume was 218.6 $m^3$ and the total cycle work was 655.1 MW. Table 18 lists the individual component sizing results for the cycle.

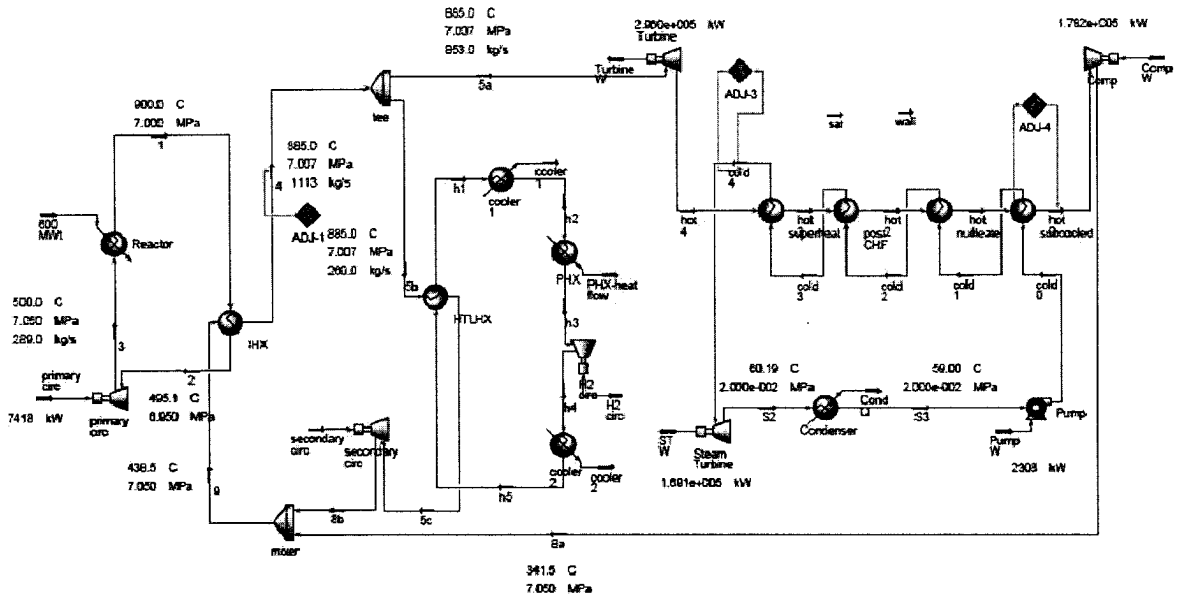


**Figure 20. HYSYS diagram of Brayton top cycle with $CO_2$ working fluid.**

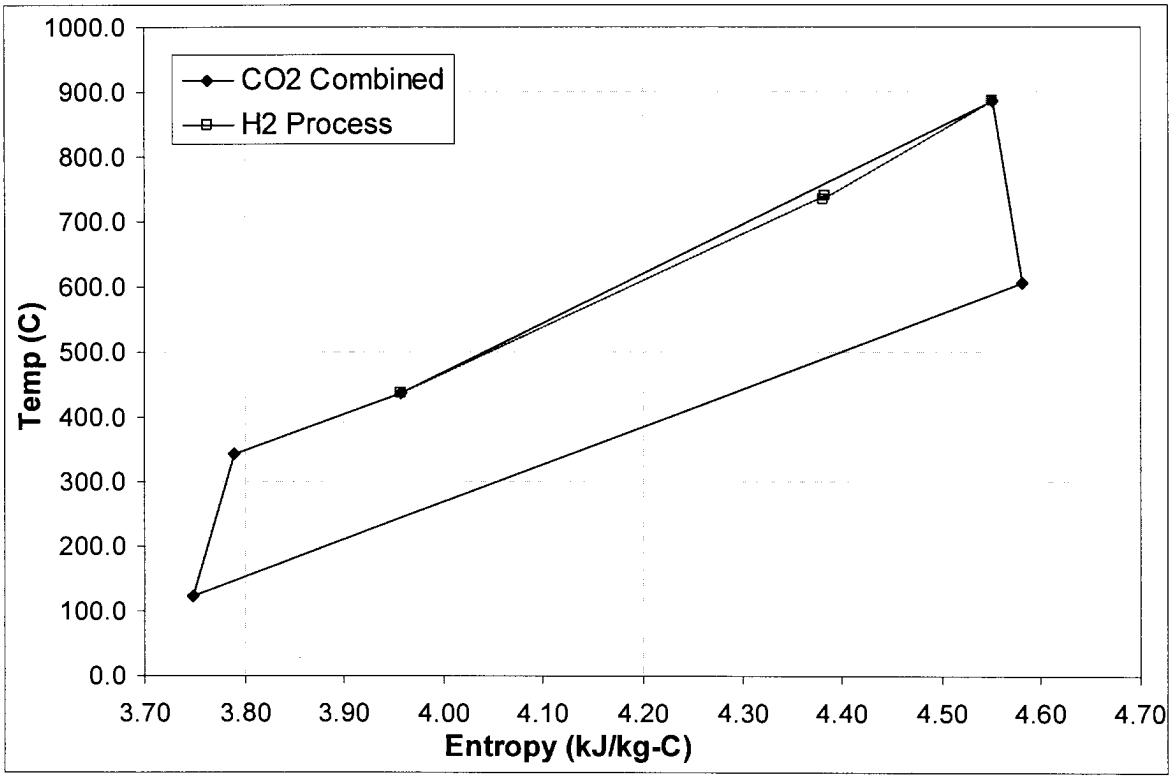


**Figure 21. T-S diagram of Brayton top cycle with $CO_2$ working fluid.**

**Table 17. State points for Brayton top cycle with $CO_2$ working fluid.**

| Point | Temp (°C) | Pressure (MPa) | Entropy (kJ/kg-K) | Enthalpy (kJ/kg) |
|---|---|---|---|---|
| 1 | 900.0 | 7.00 | 19.33 | 4561.1 |
| 2 | 495.1 | 6.95 | 17.15 | 2459.0 |
| 3 | 500.0 | 7.05 | 17.16 | 2484.7 |
| 4,5(a,b) | 885.0 | 7.01 | 4.55 | -7999.0 |
| 5c | 734.8 | 6.81 | 4.38 | -8188.7 |
| 6 | 609.0 | 1.04 | 4.58 | -8339.2 |
| 7 | 118.8 | 0.88 | 3.75 | -8868.4 |
| 8a | 341.6 | 7.05 | 3.79 | -8655.5 |
| 8b | 741.0 | 7.05 | 4.38 | -8181.1 |
| 9 | 438.5 | 7.05 | 3.96 | -8544.7 |

**Table 18. Component sizing data for combined cycle with $CO_2$ working fluid.**

| Component | Value |
|---|---|
| Gas Turbine work (MW) | 296.0 |
| Steam Turbine work (MW) | 169.1 |
| Compressor work (MW) | 178.2 |
| Pump work (MW) | 2.3 |
| Circulator work (MW) | 9.4 |
| IHX volume ($m^3$) | 48.5 |
| HTLHX volume ($m^3$) | 2.6 |
| Steam generator volume ($m^3$) | 167.5 |

### 4.2.3 Nitrogen-Helium Working Fluid

The $N_2$-He mixture was optimized for the combined cycle with a pressure ratio of 2.68 and an efficiency of 48.70%. The secondary mass flow rate was optimized at 759 kg/s. The HYSYS simulation is illustrated in Figure 22, the T-S diagram is shown in Figure 23 and the state points are summarized in Table 19. The total heat exchanger volume was 203.8 $m^3$ and the total cycle work was 719.1 MW. Table 20 lists the individual component sizing results for the cycle.

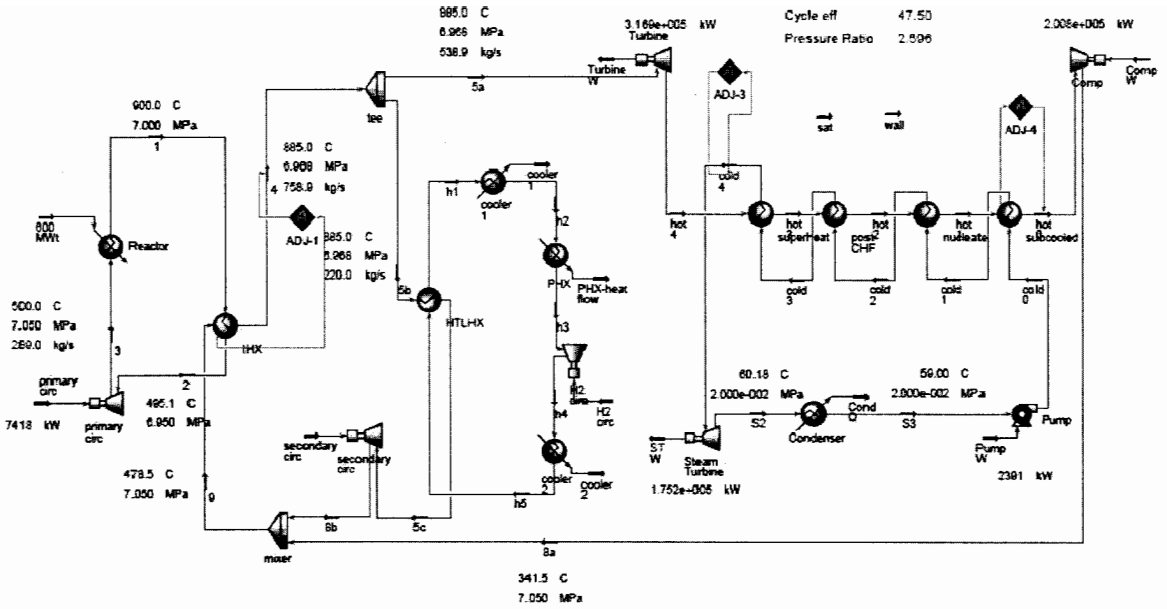


**Figure 22. HYSYS diagram of Brayton top cycle with a nitrogen-helium mixture working fluid.**

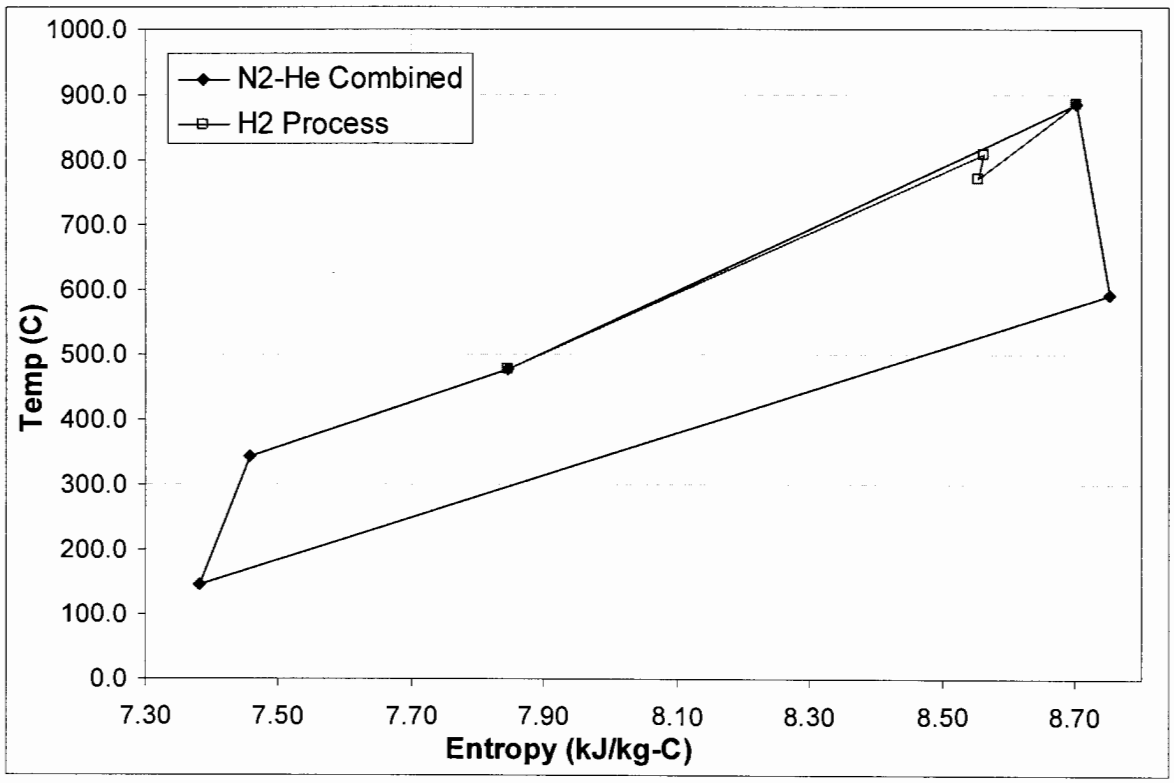


**Figure 23. T-S diagram of Brayton top cycle with a nitrogen-helium mixture working fluid.**

**Table 19. State points for Brayton top cycle with a nitrogen-helium mixture working fluid.**

| Point | Temp (°C) | Pressure (MPa) | Entropy (kJ/kg-K) | Enthalpy (kJ/kg) |
|---|---|---|---|---|
| 1 | 900.0 | 7.00 | 19.33 | 4561.1 |
| 2 | 495.1 | 6.95 | 17.15 | 2459.0 |
| 3 | 500.0 | 7.05 | 17.16 | 2484.7 |
| 4,5(a,b) | 885.0 | 6.97 | 8.70 | 1670.4 |
| 5c | 772.4 | 6.41 | 8.55 | 1446.2 |
| 6 | 592.2 | 2.67 | 8.75 | 1087.7 |
| 7 | 146.2 | 2.59 | 7.38 | 228.5 |
| 8a | 341.4 | 7.05 | 7.46 | 604.5 |
| 8b | 809.6 | 7.05 | 8.56 | 1520.6 |
| 9 | 478.5 | 7.05 | 7.85 | 870.1 |

**Table 20. Component sizing data for combined cycle with a nitrogen-helium mixture.**

| Component | Value |
|---|---|
| Gas Turbine work (MW) | 316.9 |
| Steam Turbine work (MW) | 175.2 |
| Compressor work (MW) | 200.8 |
| Pump work (MW) | 2.4 |
| Circulator work (MW) | 23.8 |
| IHX volume ($m^3$) | 71.7 |
| HTLHX volume ($m^3$) | 1.7 |
| Steam generator volume ($m^3$) | 130.4 |

### 4.2.4 Parametric Studies

Parametric studies were performed on the reactor outlet temperature, secondary mass flow rate, pressure, and turbine for the three working fluids. The results are summarized in Figures 24 through 26 and Table 21. All three working fluids behaved similarly under off-normal working conditions. However, helium was less affected by pressure that $CO_2$ and the $N_2$-He mixture. The effect of turbine cooling on the system was an approximately 0.5% efficiency decrease for all working fluids.

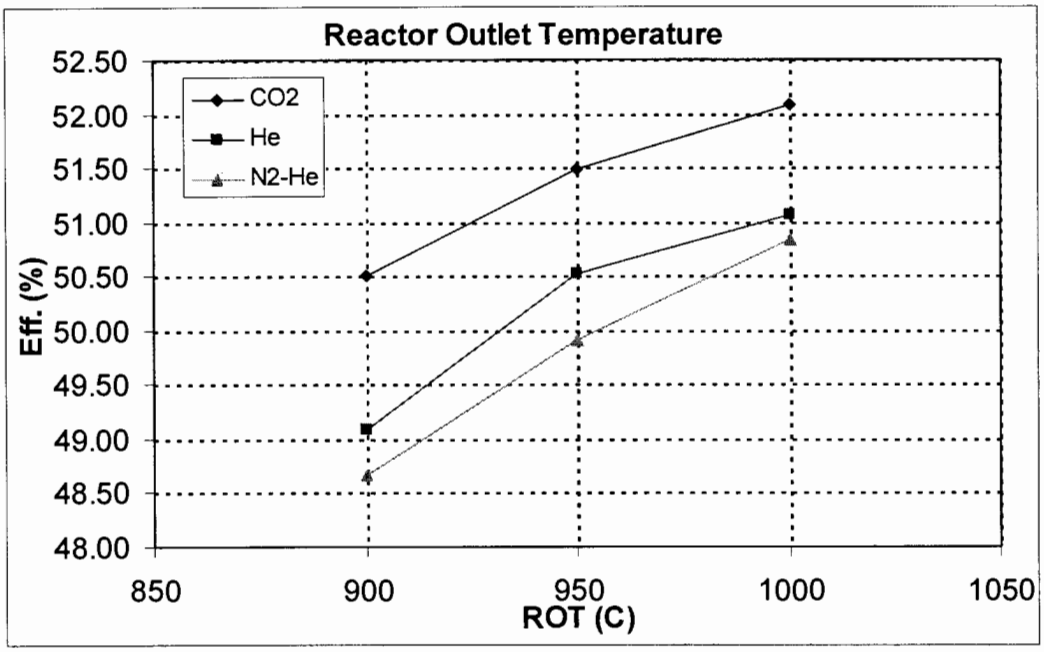


**Figure 24. Parametric study of the effects of reactor outlet temperature on combined cycle efficiency.**

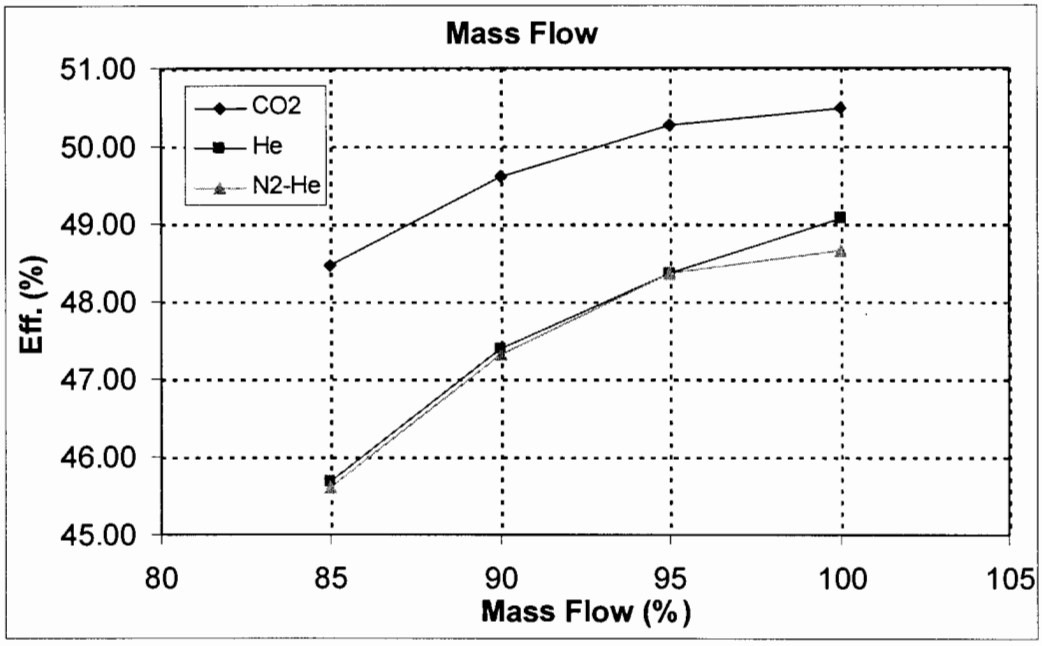


**Figure 25. Parametric study of the effects of secondary mass flow rate on combined cycle efficiency.**

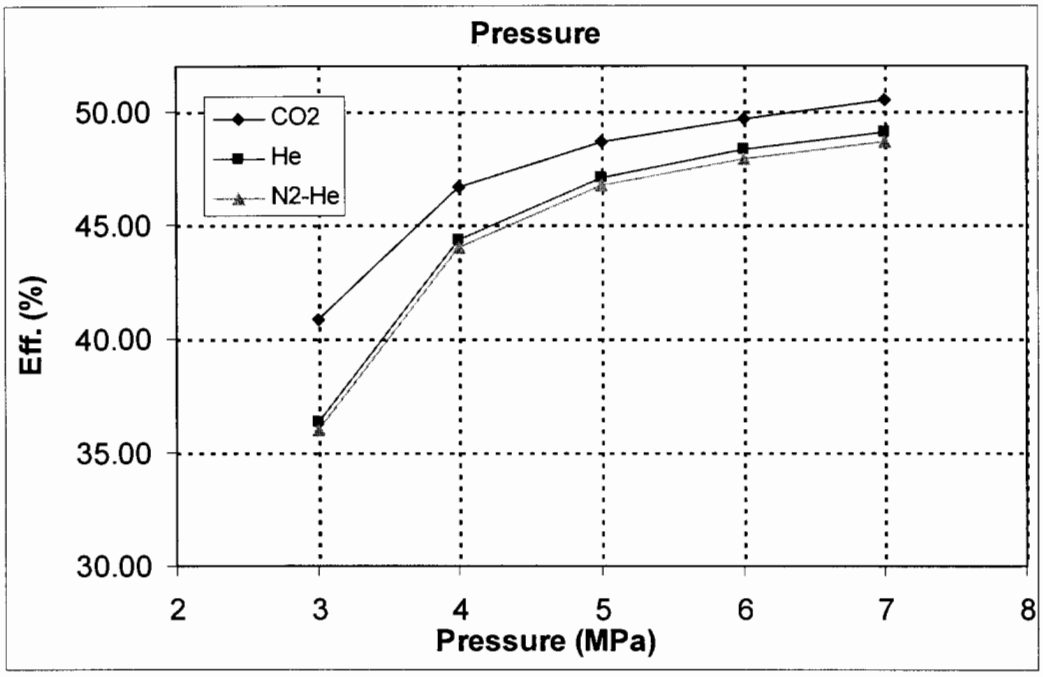


**Figure 26. Parametric study of the effects of working pressure on combined cycle efficiency.**

**Table 21. Parametric study of the effects of turbine cooling on combined cycle efficiency.**

| Turbine Cooling | | | |
|---|---|---|---|
| | CO2 | He | N2-He |
| None | 50.50 | 49.08 | 48.66 |
| 8% | 50.26 | 48.83 | 48.42 |

## 4.3 Reheated Cycle

The reheat cycle is illustrated in Figure 6~~Figure 6~~. This cycle was simulated using Flibe as the working fluid in the primary side of the NGNP and helium in the IHTL. Helium, $CO_2$ and the $N_2$-He mixture were simulated in the PCU and the results are described in Sections 4.3.1, 4.3.2 and 4.3.3, respectively.

A comparison of the working fluids in this cycle shows that helium results in the highest efficiency, but also produces the largest heat exchangers and turbomachinery. Using the $N_2$-He mixture produces a slightly lower efficiency, but significantly smaller heat exchangers. The $CO_2$ working fluid has a much lower, approximately 3%, cycle efficiency than the other fluids. $CO_2$ has the smallest turbomachinery and an intermediate value for heat exchanger volume.

### 4.3.1 Helium Working Fluid

The helium working fluid was optimized for the reheated cycle with a pressure ratio of 4.433 and an efficiency of 57.42%. The secondary mass flow rate was optimized at 200 kg/s. The HYSYS simulation is illustrated in Figure 27, the T-S diagram is shown in Figure 28 and the state points

are summarized in Table 22. The total heat exchanger volume was 373.2 $m^3$ and the total cycle work was 729.6 MW. Table 23 lists the individual component sizing results for the cycle.

A study was also performed to investigate the effects of using helium as the working fluid instead of Flibe on the primary side of the NGNP. Figure 29 shows the HYSYS simulation using a helium working fluid on the primary side. The efficiency of this cycle was 51.54% with a pressure ratio of 4.433. Comparing this to the three-shaft cycle, with an efficiency of 50.93%, there is only a 0.61% efficiency increase. This efficiency gain does not offset the cost of the additional complexity of the cycle. Therefore, using helium as a working fluid in the primary side was not a viable option and was not studied further.

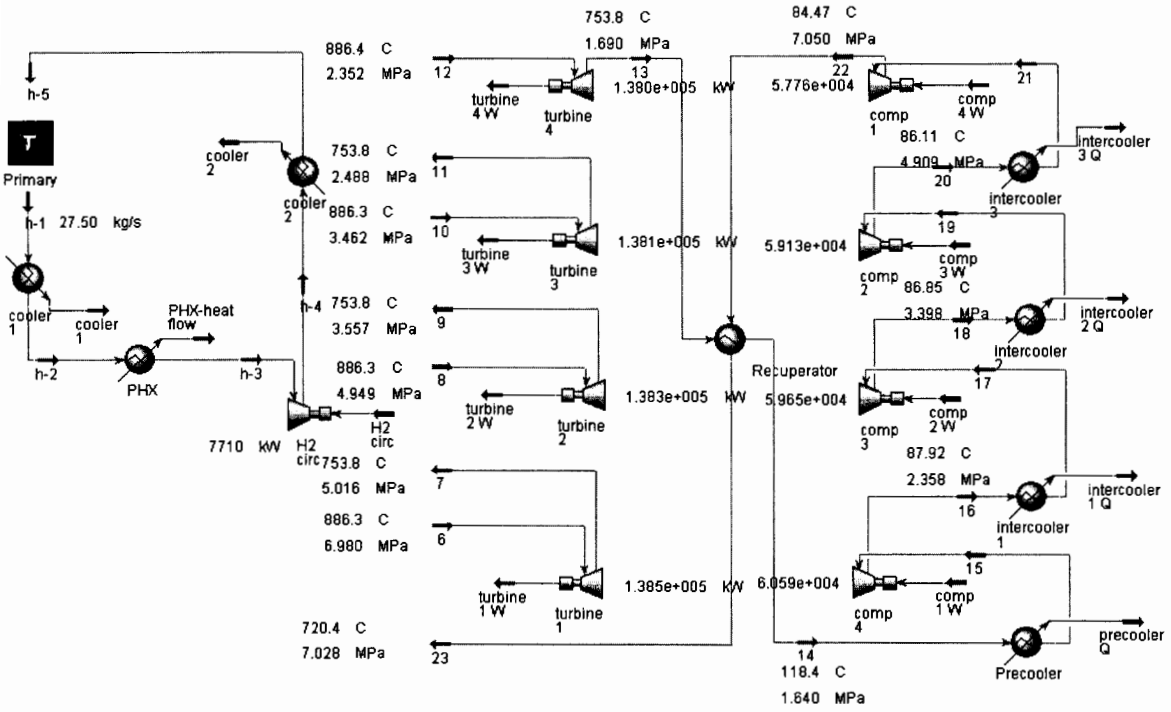


**Figure 27. HYSYS diagram of the reheated configuration with helium working fluid.**

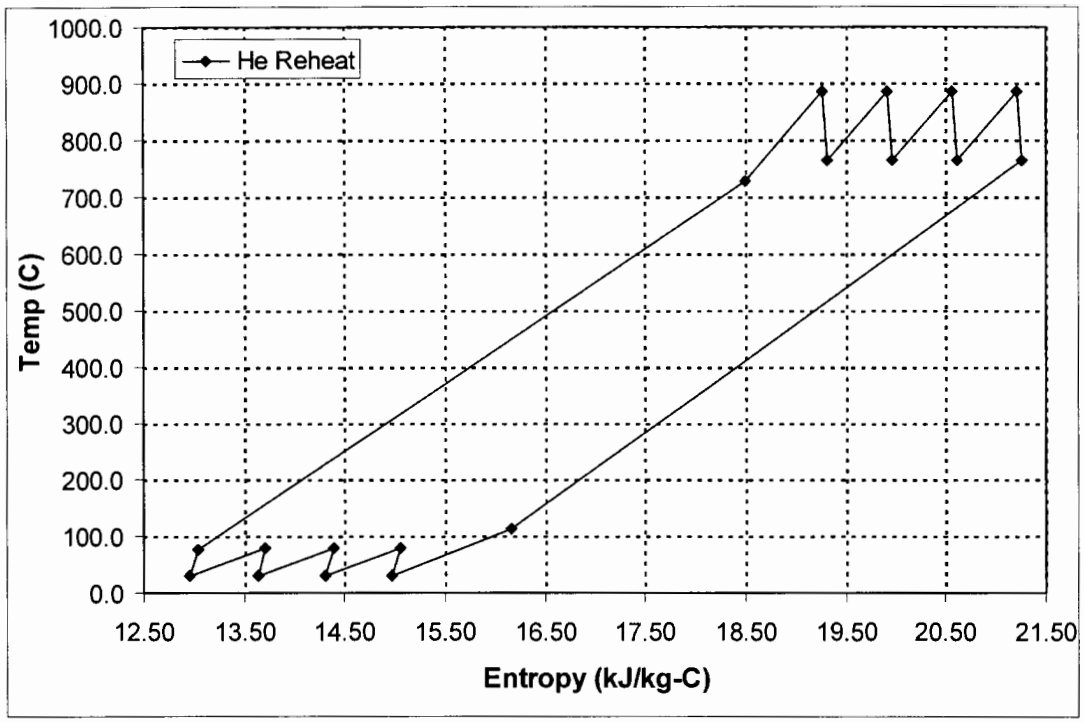


**Figure 28. T-S diagram for the reheated configuration with helium working fluid.**

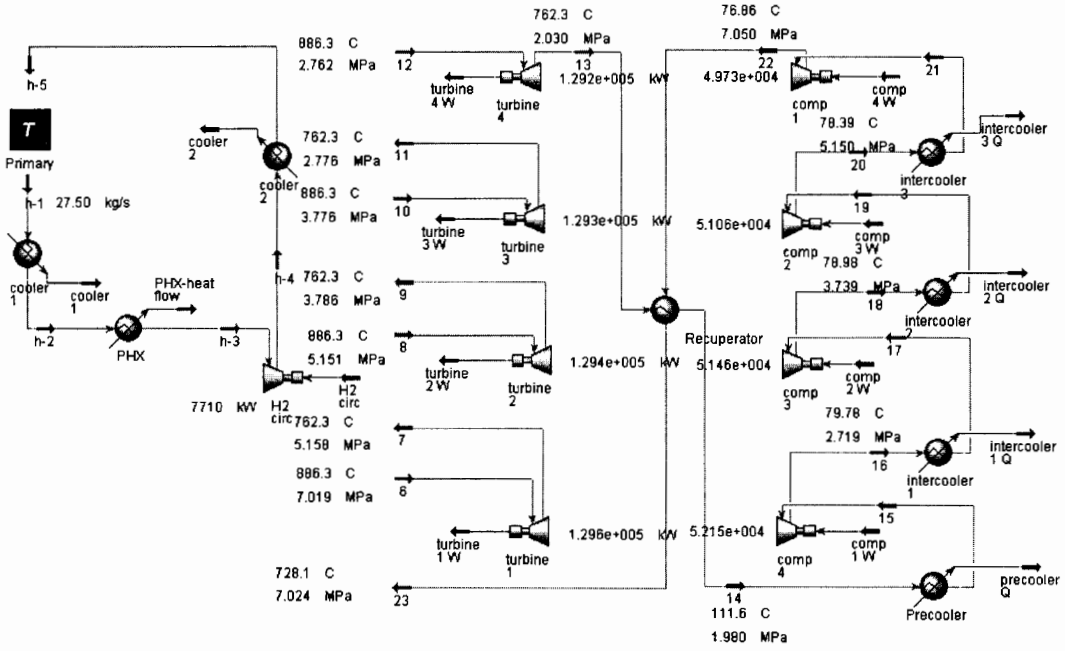


**Figure 29. HYSYS diagram of the reheated configuration with helium working fluid on primary and secondary sides.**

**Table 22. State points for the reheated configuration with helium working fluid.**

| Point | Temp (°C) | Pressure (MPa) | Entropy (kJ/kg-K) | Enthalpy (kJ/kg) |
|---|---|---|---|---|
| 1 | 900.0 | 0.1013 | -10.40 | -7374.1 |
| 2 | 900.0 | 0.1013 | -10.40 | -7374.1 |
| 3a | 744.6 | 0.1013 | -11.29 | -7744.8 |
| 3b | 778.7 | 0.1013 | -11.09 | -7663.4 |
| 3c | 778.7 | 0.1013 | -11.09 | -7663.4 |
| 3d | 778.7 | 0.1013 | -11.09 | -7663.4 |
| 3h | 559.4 | 0.1013 | -12.56 | -8186.5 |
| 4 | 763.3 | 0.1013 | -11.18 | -7700.3 |
| 5 | 763.3 | 0.1013 | -11.18 | -7700.3 |
| 6 | 886.3 | 7.02 | 19.27 | 4490.0 |
| 7 | 762.3 | 5.16 | 19.32 | 3842.0 |
| 8 | 886.3 | 5.15 | 19.91 | 4486.0 |
| 9 | 762.3 | 3.79 | 19.96 | 3839.0 |
| 10 | 886.3 | 3.78 | 20.55 | 4483.1 |
| 11 | 762.3 | 2.78 | 20.61 | 3836.8 |
| 12 | 886.3 | 2.76 | 21.20 | 4481.0 |
| 13 | 762.3 | 2.03 | 21.25 | 3835.2 |
| 14 | 111.6 | 1.98 | 16.16 | 455.3 |
| 15 | 30.0 | 1.93 | 14.98 | 31.4 |
| 16 | 79.8 | 2.72 | 15.06 | 292.1 |
| 17 | 30.0 | 2.67 | 14.31 | 33.4 |
| 18 | 79.0 | 3.74 | 14.39 | 290.7 |
| 19 | 30.0 | 3.69 | 13.64 | 36.3 |
| 20 | 78.4 | 5.15 | 13.71 | 291.6 |
| 21 | 30.0 | 5.10 | 12.97 | 40.2 |
| 22 | 76.9 | 7.05 | 13.04 | 288.8 |
| 23 | 728.1 | 7.02 | 18.51 | 3668.8 |

**Table 23. Component sizing data for reheated cycle with helium working fluid.**

| Component | Value |
|---|---|
| Turbine work (MW) | 517.5 |
| Compressor work (MW) | 204.4 |
| Circulator work (MW) | 7.7 |
| IHX volume ($m^3$) | 247.0 |
| HTLHX volume ($m^3$) | 4.7 |
| Recuperator volume ($m^3$) | 121.6 |

### 4.3.2 $CO_2$ Working Fluid

The $CO_2$ working fluid was optimized for the reheated cycle with a pressure ratio of 10.77 and a PCU efficiency of 53.72%. The secondary mass flow rate was optimized at 1050 kg/s. The HYSYS simulation is illustrated in Figure 30, the T-S diagram is shown in Figure 31 and the state

points are summarized in Table 24. The total heat exchanger volume was 354.6 $m^3$ and the total cycle work was 615.3 MW. Table 25 lists the individual component sizing results for the cycle.

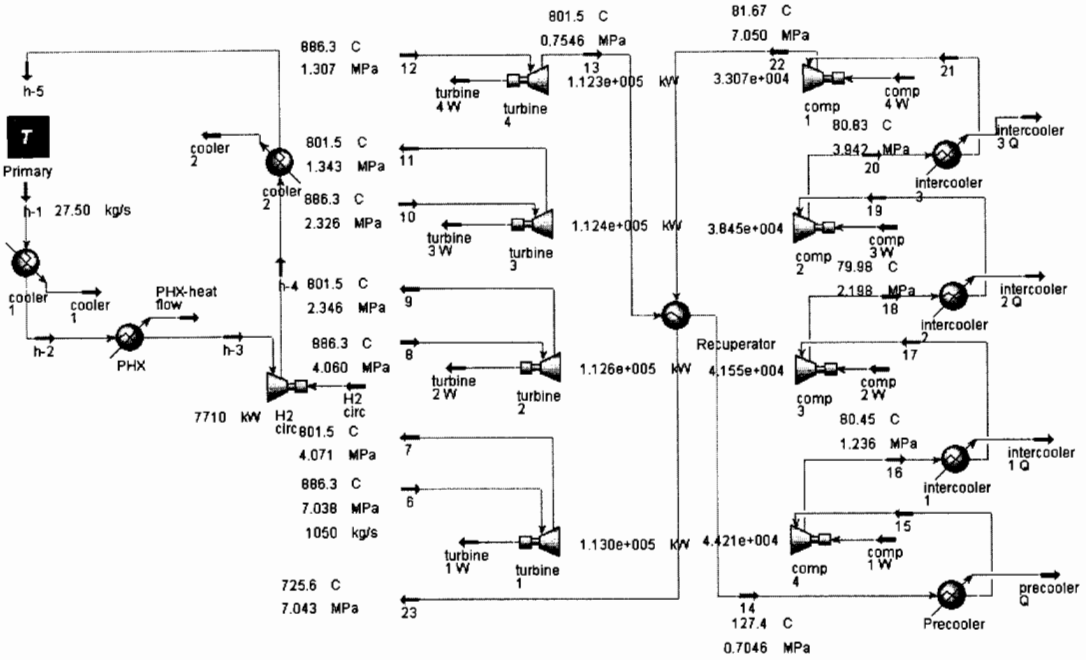


**Figure 30. HYSYS diagram of the reheated configuration with $CO_2$ working fluid.**

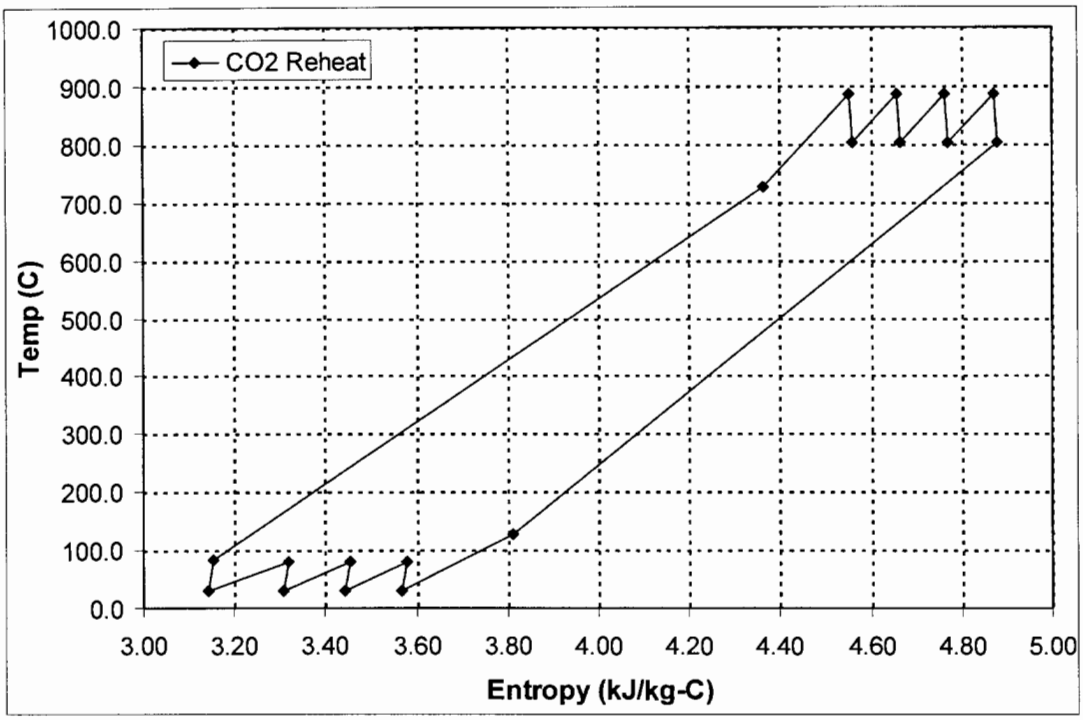


**Figure 31. T-S diagram of the reheated configuration with $CO_2$ working fluid.**

**Table 24. State points for the reheated configuration with $CO_2$ working fluid.**

| Point | Temp (°C) | Pressure (MPa) | Entropy (kJ/kg-K) | Enthalpy (kJ/kg) |
|---|---|---|---|---|
| 1 | 900.0 | 0.1013 | -10.40 | -7374.1 |
| 2 | 900.0 | 0.1013 | -10.40 | -7374.1 |
| 3a | 742.9 | 0.1013 | -11.30 | -7748.8 |
| 3b | 818.1 | 0.1013 | -10.85 | -7569.4 |
| 3c | 818.1 | 0.1013 | -10.85 | -7569.4 |
| 3d | 818.2 | 0.1013 | -10.85 | -7569.3 |
| 3h | 559.4 | 0.1013 | -12.56 | -8186.5 |
| 4 | 793.3 | 0.1013 | -11.00 | -7628.5 |
| 5 | 793.3 | 0.1013 | -11.00 | -7628.5 |
| 6 | 886.3 | 7.04 | 4.55 | -7997.3 |
| 7 | 801.5 | 4.07 | 4.56 | -8104.9 |
| 8 | 886.3 | 4.06 | 4.66 | -7997.5 |
| 9 | 801.5 | 2.35 | 4.67 | -8104.7 |
| 10 | 886.3 | 2.33 | 4.76 | -7997.6 |
| 11 | 801.5 | 1.34 | 4.77 | -8104.6 |
| 12 | 886.3 | 1.31 | 4.87 | -7997.6 |
| 13 | 801.5 | 0.75 | 4.88 | -8104.5 |
| 14 | 127.4 | 0.70 | 3.81 | -8859.1 |
| 15 | 30.0 | 0.65 | 3.57 | -8949.6 |
| 16 | 80.4 | 1.24 | 3.58 | -8907.5 |
| 17 | 30.0 | 1.19 | 3.44 | -8954.8 |
| 18 | 80.0 | 2.20 | 3.46 | -8915.2 |
| 19 | 30.0 | 2.15 | 3.31 | -8964.9 |
| 20 | 80.8 | 3.94 | 3.32 | -8928.3 |
| 21 | 30.0 | 3.89 | 3.14 | -8986.3 |
| 22 | 81.7 | 7.05 | 3.15 | -8954.8 |
| 23 | 725.6 | 7.04 | 4.36 | -8200.2 |

**Table 25. Component sizing data for reheated cycle with $CO_2$ working fluid.**

| Component | Value |
|---|---|
| Turbine work (MW) | 450.3 |
| Compressor work (MW) | 157.3 |
| Circulator work (MW) | 7.7 |
| IHX volume ($m^3$) | 218.1 |
| HTLHX volume ($m^3$) | 4.7 |
| Recuperator volume ($m^3$) | 131.8 |

### 4.3.3 Nitrogen-Helium Working Fluid

The $N_2$-He mixture was optimized for the reheated cycle with a pressure ratio of 3.87 and a PCU efficiency of 57.13%. The secondary mass flow rate was optimized at 600 kg/s. The HYSYS simulation is illustrated in Figure 32, the T-S diagram is shown in Figure 33 and the state points are summarized in Table 26. The total heat exchanger volume was 286.8 $m^3$ and the total cycle work was 717.9 MW. Table 27 lists the individual component sizing results for the cycle.

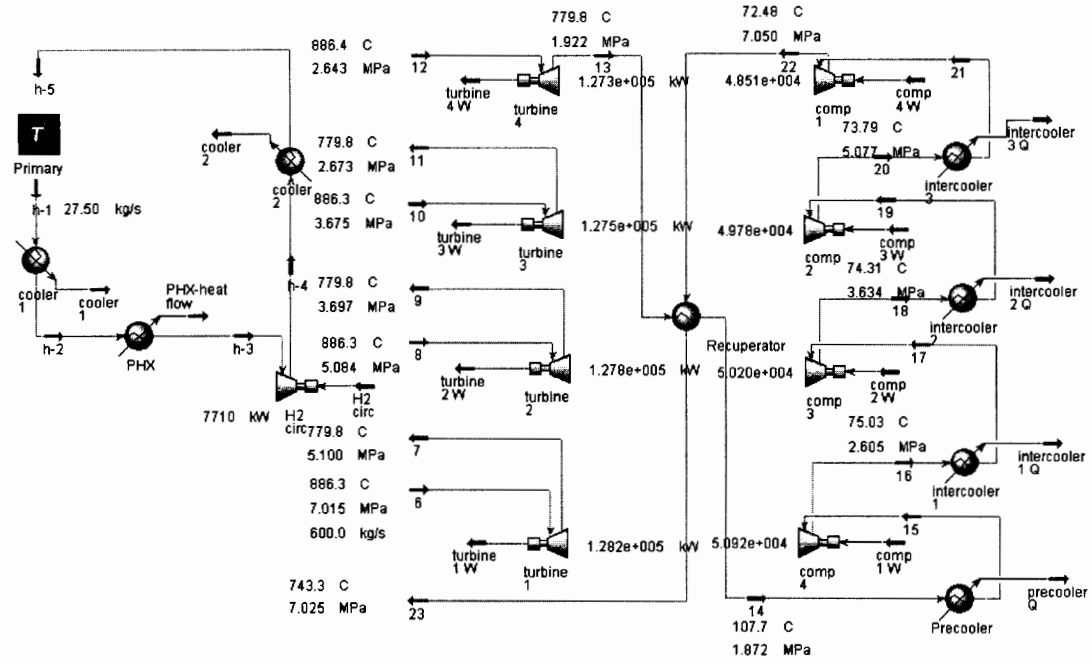


**Figure 32. HYSYS diagram of the reheated configuration with a nitrogen-helium mixture working fluid.**

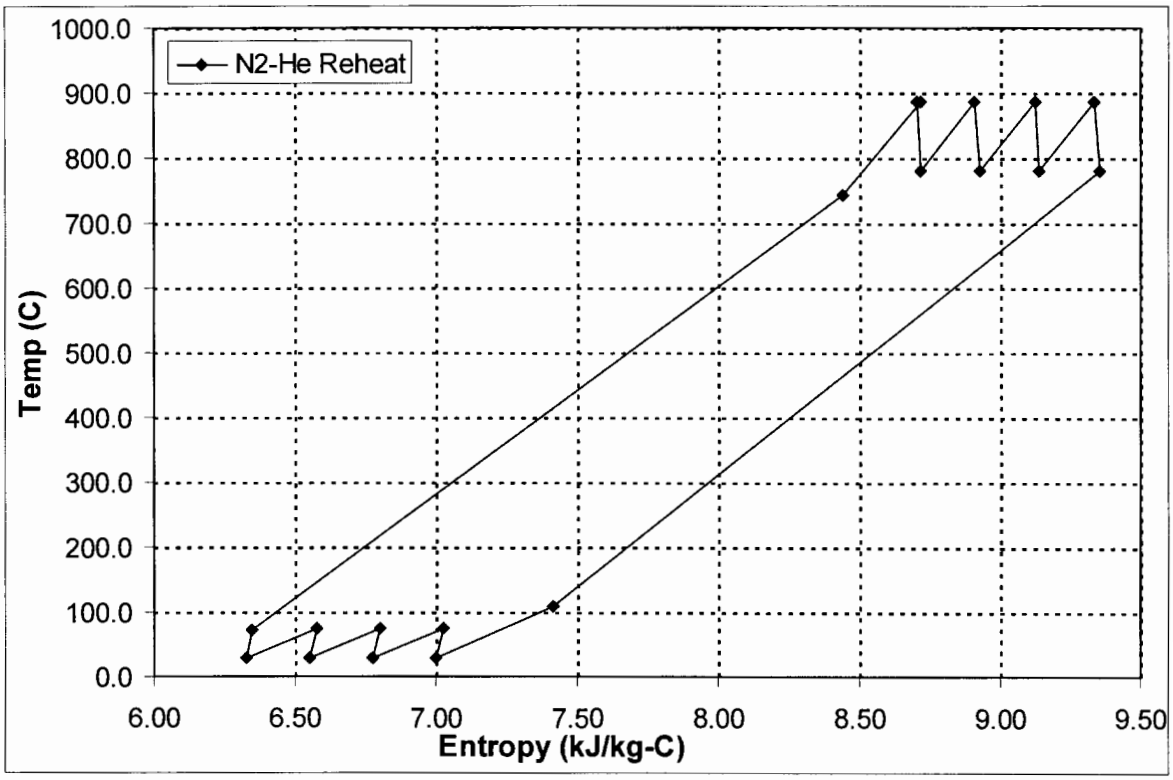


**Figure 33. T-S diagram of the reheated configuration with a nitrogen-helium mixture working fluid.**

**Table 26. State points for the reheated configuration with a nitrogen-helium mixture working fluid.**

| Point | Temp (°C) | Pressure (MPa) | Entropy (kJ/kg-K) | Enthalpy (kJ/kg) |
|---|---|---|---|---|
| 1 | 900.0 | 0.1013 | -10.40 | -7374.1 |
| 2 | 900.0 | 0.1013 | -10.40 | -7374.1 |
| 3a | 759.9 | 0.1013 | -11.20 | -7708.3 |
| 3b | 796.3 | 0.1013 | -10.98 | -7621.4 |
| 3c | 796.3 | 0.1013 | -10.98 | -7621.4 |
| 3d | 796.4 | 0.1013 | -10.98 | -7621.1 |
| 3h | 559.4 | 0.1013 | -12.56 | -8186.5 |
| 4 | 780.7 | 0.1013 | -11.07 | -7658.6 |
| 5 | 780.7 | 0.1013 | -11.07 | -7658.6 |
| 6 | 886.3 | 7.02 | 8.70 | 1673.1 |
| 7 | 779.8 | 5.10 | 8.72 | 1459.4 |
| 8 | 886.3 | 5.08 | 8.91 | 1670.7 |
| 9 | 779.8 | 3.70 | 8.93 | 1457.8 |
| 10 | 886.3 | 3.68 | 9.12 | 1669.0 |
| 11 | 779.8 | 2.67 | 9.14 | 1456.6 |
| 12 | 886.4 | 2.64 | 9.34 | 1668.0 |
| 13 | 779.8 | 1.92 | 9.35 | 1455.7 |
| 14 | 107.7 | 1.87 | 7.41 | 155.3 |
| 15 | 30.0 | 1.82 | 7.00 | 8.8 |
| 16 | 75.0 | 2.61 | 7.02 | 93.6 |
| 17 | 30.0 | 2.56 | 6.78 | 8.6 |
| 18 | 74.3 | 3.63 | 6.80 | 92.2 |
| 19 | 30.0 | 3.58 | 6.55 | 8.3 |
| 20 | 73.8 | 5.08 | 6.58 | 91.3 |
| 21 | 30.0 | 5.03 | 6.33 | 8.0 |
| 22 | 72.5 | 7.05 | 6.35 | 88.9 |
| 23 | 743.3 | 7.03 | 8.44 | 1389.3 |

**Table 27. Component sizing data for reheated cycle with a nitrogen-helium mixture working fluid.**

| Component | Value |
|---|---|
| Turbine work (MW) | 510.8 |
| Compressor work (MW) | 199.4 |
| Circulator work (MW) | 7.7 |
| IHX volume ($m^3$) | 153.1 |
| HTLHX volume ($m^3$) | 4.7 |
| Recuperator volume ($m^3$) | 129 |

## 4.4 Effects of IHTL and HTSE

The HTSE plant was coupled to the reactor and the PCU by means of the IHTL. Helium and liquid salt were investigated as working fluids in the IHTL. Figure 34 depicts the HYSYS simulation of the entire plant including a three-shaft PCU and the HTSE plant. The overall efficiency was calculated

for the various PCU and IHTL working fluids and PCU configurations using Equation 2. Table 28 summarizes the overall efficiency of the plant for the various configurations and working fluids. The overall efficiency of the facility is ~4-5% lower than the PCU efficiency. This is due to the addition of the pumping power in the IHTL and HTSE.

The HTSE facility requires electrical power from the PCU to operate the electrolysis cell. Therefore much of the electrical power produced by the PCU is required by the HTSE. The excess power from the PCU can be used for electrical generation. The amount of excess power available for electrical generation varies for each configuration. Table 29 summarizes the electrical power generation for each configuration. When using a helium working fluid in the IHTL, hydrogen can be produced at a rate of 113.7 kg/hr, while using the liquid salt working fluid produces 96.42 kg/hr of hydrogen. The difference in these values is due to the amount of heat that is being transferred to the HTSE facility by the working fluids. This is due to the assumptions made in the design of the IHTL. The amount of hydrogen produced can be adjusted by increasing the heat flow through the IHTL and increasing the electrical power sent to the electrolysis cell. These are competing values, as the heat transfer to the IHTL increases the power to PCU and electrical generation decreases.

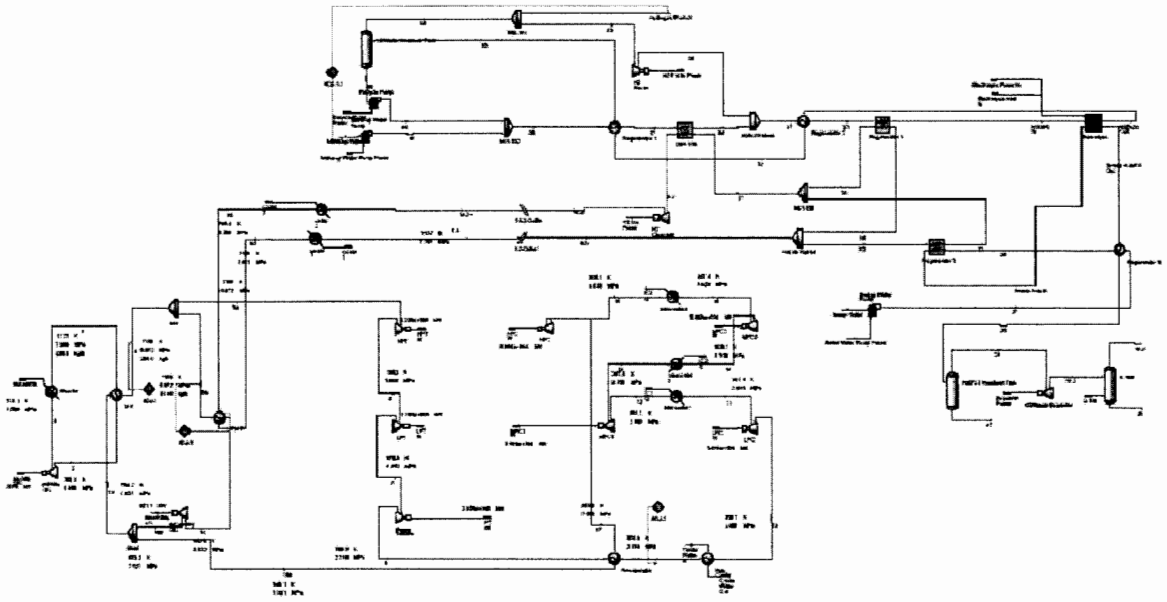

**Figure 34. HYSYS model of entire plant with a three-shaft PCU and HTSE plant.**

**Table 28. Summary of overall plant efficiency for each PCU configuration and IHTL working fluid.**

| PCU configuration and working fluid | Efficiency (Helium) | PCU configuration and working fluid | Efficiency ($NaBF_4$-NaF) |
|---|---|---|---|
| 3-Shaft | | 3-Shaft | |
| He | 44.83 | He | 46.02 |
| $CO_2$ | 41.09 | $CO_2$ | 42.26 |
| $N_2$-He | 44.78 | $N_2$-He | 45.94 |
| Combined | | Combined | |
| He | 43.07 | He | 44.40 |
| $CO_2$ | 44.35 | $CO_2$ | 45.69 |
| $N_2$-He | 42.69 | $N_2$-He | 44.02 |
| Reheat | | Reheat | |
| He | 50.80 | He | 51.99 |
| $CO_2$ | 47.45 | $CO_2$ | 48.64 |
| $N_2$-He | 50.52 | $N_2$-He | 51.71 |

**Table 29. Excess power available for electrical generation for each PCU configuration and IHTL working fluid.**

| PCU configuration and working fluid | Electrical Power (Helium) | PCU configuration and working fluid | Electrical Power ($NaBF_4$-NaF) |
|---|---|---|---|
| 3-Shaft | MW | 3-Shaft | MW |
| He | 43.29 | He | 84.62 |
| $CO_2$ | 20.87 | $CO_2$ | 62.07 |
| $N_2$-He | 42.97 | $N_2$-He | 84.12 |
| Combined | | Combined | |
| He | 32.71 | He | 74.91 |
| $CO_2$ | 40.43 | $CO_2$ | 82.63 |
| $N_2$-He | 30.45 | $N_2$-He | 72.65 |
| Reheat | | Reheat | |
| He | 79.13 | He | 120.45 |
| $CO_2$ | 59.03 | CO2 | 100.35 |
| $N_2$-He | 77.43 | $N_2$-He | 118.75 |

# 5.0 ENGINEERING ANALYSES OF THE IHTL

Engineering analyses were performed for several configurations of the IHTL piping of the NGNP. This loop transports heat from the nuclear reactor to the hydrogen production plant. The analyses included thermal-hydraulic, mechanical, and economic evaluations. The configurations evaluated included parallel, concentric, and jacketed arrangements. Two different working fluids were evaluated including high-pressure helium and a liquid salt.

A next generation high-temperature reactor could be envisioned as a single-purpose facility that produces hydrogen or a dual-purpose facility that produces hydrogen and electricity. At the current time, it is anticipated that early plants may be dual-purpose facilities that demonstrate both hydrogen and efficient electrical generation, and that later plants could be single-purpose facilities. The engineering analyses were generally performed for both single and dual-purpose facilities.

The thermal-hydraulic, mechanical, and economic evaluations are described in Sections 5.1 through 5.3, respectively, respectively.

## 5.1 Thermal-Hydraulic Analyses

Thermal-hydraulic analyses were performed to size the hot and cold legs of the IHTL for two geometric configurations and two working fluids. The two geometric configurations shown in Figure 35 were studied. The first used a parallel configuration in which separate hot and cold legs were utilized. The hot leg transported hot fluid from the IHX to the PHX. The cooled fluid then returned to the IHX through the cold leg, which contained a circulator. The second geometry utilized a concentric configuration in which the hot leg was contained within an annular cold leg. This configuration, which was inspired by the cross vessel of the Gas-Turbine Modular Helium Reactor (General Atomics 1996), results in a relatively small pressure difference across the hot leg metal and relatively low stresses.

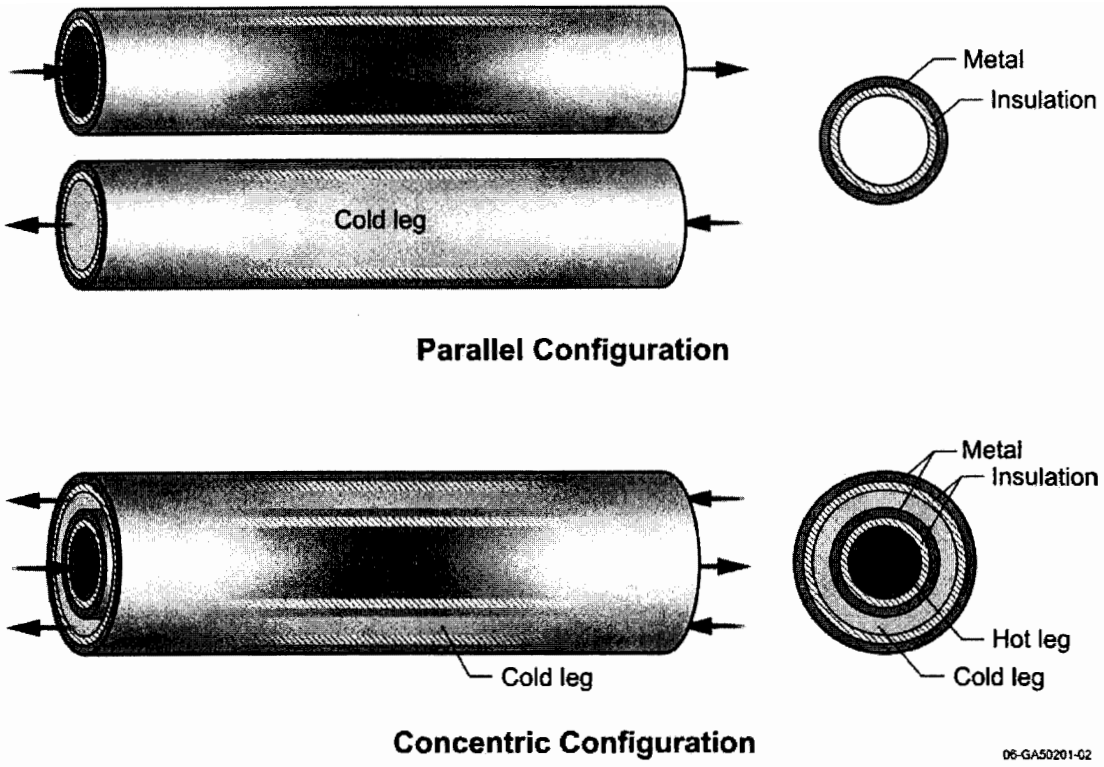


**Figure 35. Parallel and concentric piping configurations for the IHTL.**

Both the parallel and concentric configurations modeled here were similar to the design described by Richards et al. (2006) in that a ceramic insulating blanket was used on the inside of the pipes to reduce the operating temperature of the metal. The reduced operating temperature increases the stress rupture strength and reduces concerns relative to creep. For the purposes of this analysis, the insulation was assumed to be perfect and have a constant thermal conductivity of 0.2 W/m-K. Detailed thermal analyses will eventually have to be performed to determine the effects of flaws in the insulation on localized temperatures in the metal. Detailed stress analyses will also be required to determine the effects of hot spots on the behavior of the metal and the effects of thermal expansion on the structural integrity of the piping and insulation. The insulation may also have to be lined to reduce concerns relative to corrosion and erosion, but such lining was not modeled here.

The general parameters used in the analysis were based on those given by Davis et al. (2005) and are summarized in Table 30. As shown in the table, the loop thermal power was varied between 50 and 600 MW, corresponding to dual- and single-purpose hydrogen production facilities, respectively. The separation distance between the nuclear and hydrogen production plants was varied between 60 and 500 m, with 90 m considered to be a best-estimate value based on the recommendation of Smith et al. (2005).

**Table 30. Engineering analysis parameters.**

| Parameter | Value |
|---|---|
| | |
| NGNP: | |
| Power, MW | 600 |
| Outlet temperature, °C | 900 |
| Core temperature rise, °C | 400 |
| Pressure, MPa | 7 |
| | |
| IHTL: | |
| Power, MW | 50 - 600 |
| Separation distance, m | 60 - 500 |
| Pressure, MPa | 7 |
| | |
| Hydrogen plant: | |
| Maximum delivered temperature, °C | 850 |
| Inlet fluid temperature, °C | 341 |

The thermal-hydraulic analysis was based on the methods described by Davis et al. (2005). Analyses were performed for two working fluids, including helium and a liquid salt ($NaBF_4$-NaF in molar concentrations of 92 and 8%). The $NaBF_4$-NaF liquid salt was selected because of its relatively low freezing point of 385 °C. The inner diameters of the hot and cold legs were sized to produce a given pressure drop during normal operating conditions. The pressure drops were assumed to be 0.05 MPa with helium and 0.30 MPa with the $NaBF_4$-NaF. The thickness of the insulation was determined based on two criteria. The first criterion was to limit the total heat loss to 1.5 MW or less. The heat losses through the hot and cold legs were limited to 0.8 and 0.7 MW, respectively. The second criterion limited the metal temperature to less than 355 °C. This relatively low operating temperature enabled carbon steel to be considered as the piping material because its allowable stress intensity does not begin to decrease sharply until the temperature exceeds 380 °C (Ulrich 1984). The required amount of insulation was generally set by the temperature criterion when the separation distance between the nuclear and hydrogen plants was small and was set by the heat loss criterion at larger separation distances. The thickness of the piping metal was taken as 6% of the inner diameter, except for the hot leg in the concentric configuration, where the thickness was reduced to 2% to account for the reduced stress in the hot leg pipe for this configuration. The 6% thickness-to-diameter ratio roughly corresponds to that for Schedule-80 pipe for the parallel dual-purpose designs at the nominal separation distance of 90 m.

Thermal-hydraulic conditions for the IHTL for four separate cases are shown in Figures 36 through 39. Figures 36 and 37 are for a working fluid of helium at loop thermal powers of 50 and 600 MW, respectively. Figures 38 and 39 are for a working fluid of $NaBF_4$-NaF. The minimum loop temperatures shown in Figures 38 and 39 exceed the freezing temperature of $NaBF_4$-NaF by nearly 90 °C, which should provide a reasonable margin for operation. Although the figures show various components of the PCU, only the compressor would actually be required for the 600-MW cases because all of the reactor power was transported to the hydrogen production plant, with none left for electricity production.

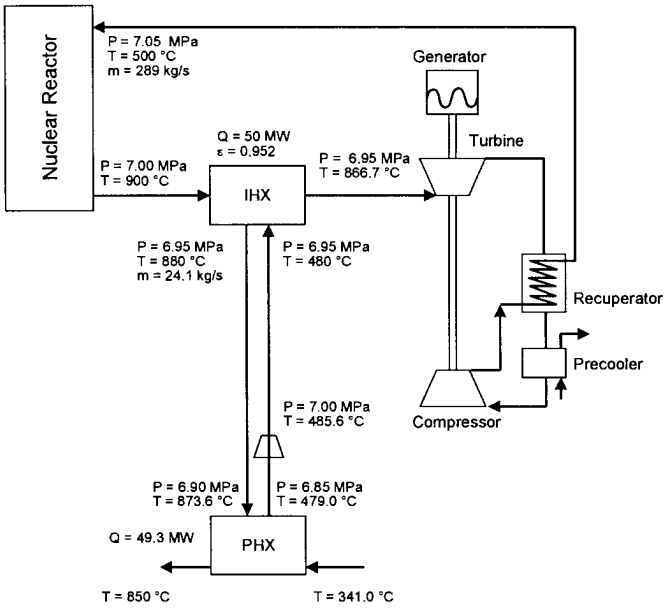


**Figure 36. Thermal-hydraulic conditions for a 50-MW loop with helium working fluid.**

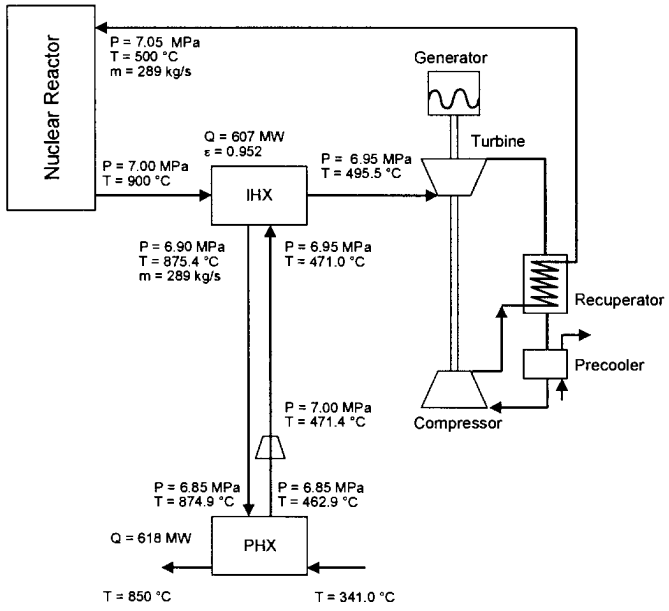


**Figure 37. Thermal-hydraulic conditions for a 600-MW loop with helium working fluid.**

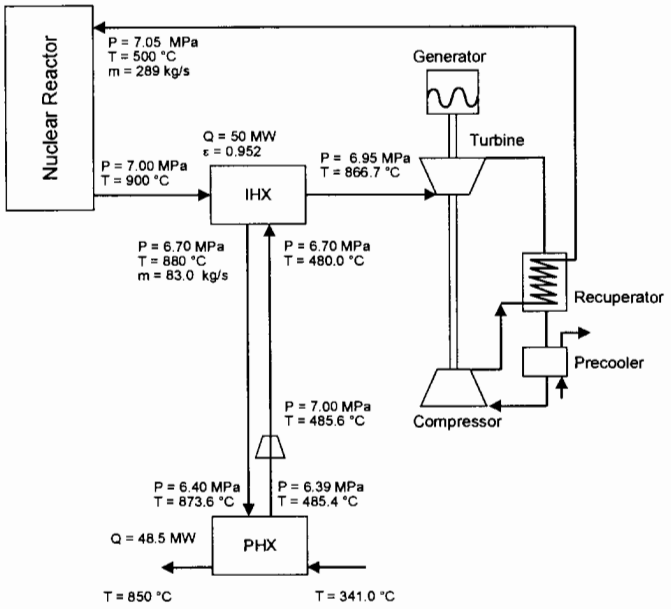


**Figure 38. Thermal-hydraulic conditions for a 50-MW loop with $NaBF_4$-NaF working fluid.**

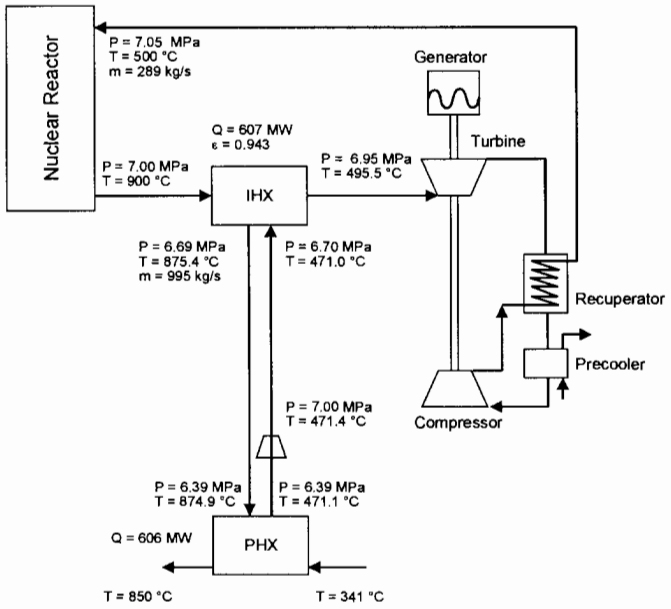


**Figure 39. Thermal-hydraulic conditions for a 600-MW loop with $NaBF_4$-NaF working fluid.**

Figure 40 shows the calculated inner diameter of the cold leg as a function of separation distance for both the parallel and concentric configurations of dual- and single-purpose facilities with helium as the working fluid. The diameter required to provide a given pressure drop increased with separation distance, loop power, and when the configuration changed from parallel to concentric. Increasing the separation distance from 90 to 500 m increased the diameter by 40% in the parallel configuration and by 60% in the concentric configuration. Increasing the loop power from 50 to 600 MW increased the

diameter by a factor of 2.6. The diameter was 70 to 100% larger with the concentric configuration. These results show that all three parameters have a significant effect on the size of the piping and, as will be shown later, on the cost. Although not shown, the diameter of the hot leg was about 10% greater than the diameter of the cold leg in the parallel configuration.

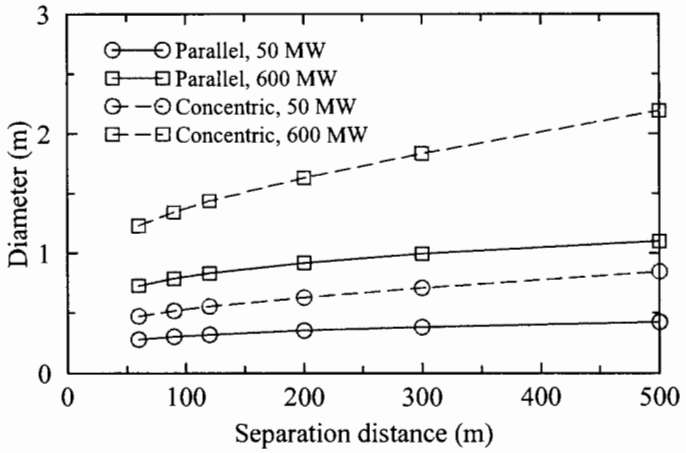


**Figure 40. The effect of configuration, power, and separation distance on cold leg diameter with helium as the working fluid.**

The amount of insulation required to meet the heat loss and metal temperature criteria was a strong function of the separation distance and, to a lesser extent, power. Figure 41 shows the effects of various parameters on the required insulation in the cold leg. Increasing the separation distance from 90 to 500 m increased the insulation thickness by a factor of 20 while increasing the power from 50 to 600 MW caused the thickness to increase by a factor of three. Slightly less insulation was required with the concentric configuration. Although the total heat loss was the same in both configurations, the heat loss was divided between the hot and cold legs in the parallel configuration whereas the entire heat loss passed through the cold leg wall in the concentric configuration. Thus, the heat loss through the cold leg was nearly two times higher in the concentric configuration. The larger heat loss resulted in less insulation and more than compensated for the additional insulation required because of the larger diameter in the concentric configuration. Note that the thickness required for the hot leg in the parallel configuration was more than twice the thickness shown for the cold leg. The amount of insulation required was relatively modest except for the cases at high power and large separation distances. For these cases, more reasonable thicknesses could be achieved by relaxing the heat loss criterion. The heat loss could be increased by a factor of four and still represent only 1% of the 600 MW of loop power.

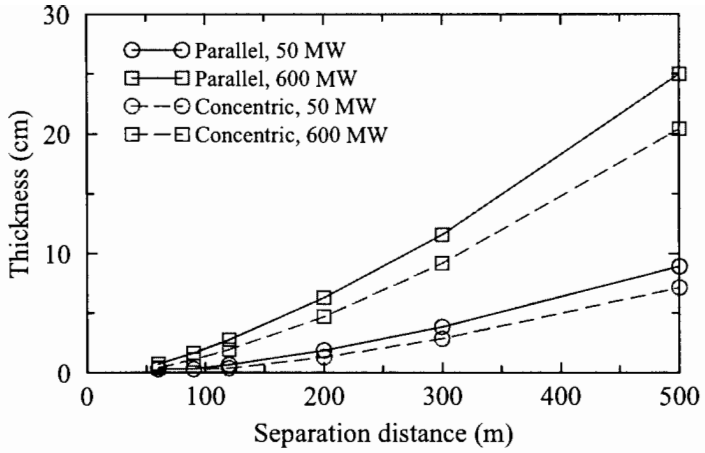


**Figure 41. The effect of configuration, power, and separation distance on the cold leg insulation thickness with helium as the working fluid.**

Figure 42 shows the effects of the working fluid on the inner diameter of the cold leg. The superior heat transport characteristics of the liquid salt significantly reduce the size of the heat transport loop piping compared to that needed with helium. The diameter with liquid salt was only 36% of that required with helium. In fact, the diameter of the 600-MW single-purpose facility with liquid salt was slightly smaller than the 50-MW dual-purpose facility with helium.

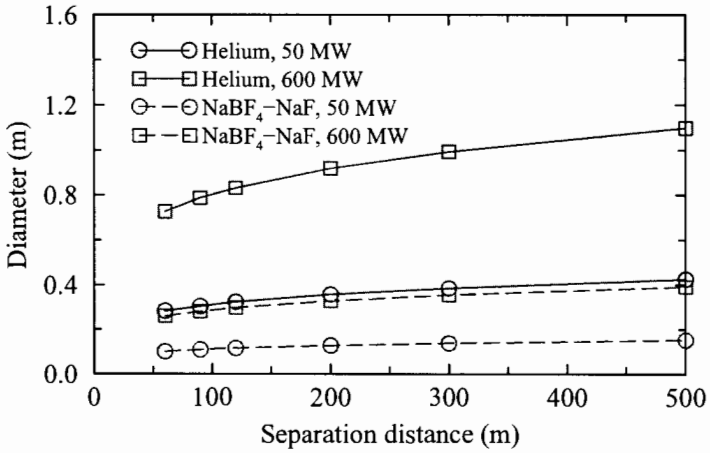


**Figure 42. The effect of working fluid on the cold leg diameter for the parallel configuration.**

Figure 43 shows the effect of the working fluid on the amount of insulation required in the cold leg for the parallel configuration. The amount of insulation required with the liquid salt was significantly less than that required with helium at the larger separation distances, where the heat loss was the same with both working fluids. The insulation thickness was nearly the same with both fluids at small separation distances, such as at 90 m in the 50-MW case, where the thickness was determined by the metal temperature criterion. However, when the metal temperature was the same, the heat loss was much less with the liquid salt because of the smaller heat transfer area due to the smaller pipe diameter.

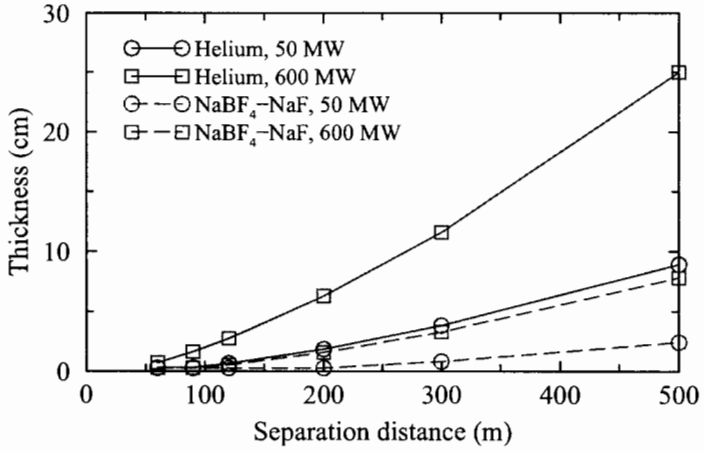


**Figure 43. The effect of working fluid on the insulation thickness in the cold leg for the parallel configuration.**

## 5.2 Mechanical Analyses

Simple stress calculations were performed for three configurations of the IHTL piping. The configurations included the parallel and concentric arrangements described in Section 5.1 and a jacketed arrangement, in which a pressurized pipe was placed outside of the hot leg.

The stress evaluations were based on the case with helium working fluid, 50-MW of loop power, and a separation distance of 90 m. The evaluations determined the hoop stress arising from the maximum pressures presented in Figure 36. The evaluations used thin-walled approximations in the metal and neglected the strength of the insulation. The assumed conditions and geometry are summarized in Table 31. In the jacketed configuration, the pressure in the jacket was half of that of the hot leg. The thickness-to-diameter ratios of the hot leg and the jacket were half of the value used for the legs in the parallel configuration.

**Table 31. Stress analysis parameters.**

| Parameter | Value |
|---|---|
| | |
| Hot / cold leg pressure, MPa | 6.95 / 7.0 |
| Metal temperature, °C | 355 |
| Metal material | Carbon steel |
| | |
| Parallel configuration: | |
| Hot / cold leg inner diameter, m | 0.330 / 0.304 |
| Hot / cold leg insulation thickness, m | 0.0125 / 0.00305 |
| Metal thickness-to-inner-diameter ratio | 0.06 |
| | |
| Concentric configuration: | |
| Hot / cold leg inner diameter, m | 0.3300 / 0.5186 |
| Hot / cold leg insulation thickness, m | 0.00920 / 0.00305 |
| Hot leg metal thickness-to-inner-diameter ratio | 0.02 |
| Cold leg metal thickness-to-inner-diameter ratio | 0.06 |
| | |
| Jacketed configuration: | |
| Jacket pressure, MPa | 3.45 |
| Hot leg inner diameter, m | 0.330 |
| Hot leg insulation thickness, m | 0.0125 |
| Hot leg metal thickness-to-inner-diameter ratio | 0.03 |
| Jacket inner diameter, m | 0.400 |
| Jacket metal thickness-to-inner-diameter ratio | 0.03 |

The hoop stress calculated for each configuration was then compared to 132 MPa, the allowable value for Class C carbon steel seamless pipe at 355 °C (ASME 2002). Ratios of the allowable stress to the calculated stress are presented in Table 32. In each case, the allowable stress was slightly more than two times the calculated stress. The difference between the allowable and calculated values provides some margin for increases in stress at elbows and fittings and reductions in strength at welds.

**Table 32. Stress analysis results.**

| Configuration | Allowable stress/ calculated stress |
|---|---|
| | |
| Parallel configuration: | |
| Hot leg | 2.16 |
| Cold leg | 2.14 |
| | |
| Concentric configuration: | |
| Cold leg | 2.14 |
| | |
| Jacketed configuration: | |
| Hot leg | 2.22 |
| Jacket | 2.22 |

The stress evaluation indicates that the design appears feasible if the insulation is effective in reducing the temperature of the metal to 355 °C.

## Parallel Configuration

The thermal expansion characteristics of the hot leg in the parallel configuration shown in Figure 35 were analyzed using PipeStress (DST Computer Services 2004) software. The hot leg was assumed to be anchored at both ends. Calculations were performed for two materials, Inconel 617 and carbon steel (SA-106 Grade B). The operating temperature was assumed to be either 355 °C, which represents a case in which the internal insulation is effective in reducing the temperature of the metal, or 850 °C, which represents a case without internal insulation. Piping parameters are listed in Table 33.

**Table 33. Hot leg parameters.**

| Parameter | Value |
|---|---|
| | |
| Pipe outside diameter, mm | 394.6 |
| Pipe wall thickness, mm | 19.8 |
| Pipe length, m | 90 |
| Operating temperature, °C | 355 |
| Operating pressure, MPa | 6.9 |
| Ambient temperature, °C | 20 |

The internal layer of insulation was omitted from this analysis because it is assumed that it adds no strength to the pipe. This analysis did not include any dynamic effects (seismic, wind loads, vibrations, etc.). Only pressure and thermal stresses were calculated. The weight of the insulation should not materially influence these results.

Material properties for Inconel 617 were taken from the ASME Boiler and Pressure Vessel Code 2004 with Addenda (ASME 2004) and the Special Metals website (Special Metals 2005). Material properties for carbon steel were taken from ASME Boiler and Pressure Vessel Code 2004 with Addenda (ASME 2004).

This pipeline was modeled in either an expansion loop or semi-circular configuration. The lengths of the expansion loops were adjusted so the maximum calculated stress is about equal to the maximum allowable stress. No length adjustments were made to the semi-circular configuration. The semi-circular configuration was used because it required less pipe length for the high temperature cases. It was chosen as one possible configuration that would meet the requirements and eliminate the expansion loops. Industry typically uses expansion loops to build in some compliance in high temperature piping.

Four cases were evaluated using different materials, configurations, and operating temperatures. Results are summarized in Table 34. Results for individual cases are shown in pairs beginning with Figures 44 and 45 for Case 1. The black line in Figure 44 shows the pipe at ambient temperature. The red line shows the pipe at the operating temperature. The displacement due to thermal expansion is exaggerated for clarity. Figure 45 lists the elements with the highest stresses. The far right column shows the ratio of the calculated stress to the allowable stress. Results for the other cases are also

presented in pairs, beginning with Figures 46 and 47 for Case 2 and ending with Figures 50 and 51 for Case 4.

**Table 34. Results of the thermal expansion calculations (Parallel Configuration).**

| Case | Material | Configuration | Temperature (°C) | Pipe Length (m) | Max. Code Stress Ratio | Max. Deformation (mm) |
|---|---|---|---|---|---|---|
| 1 | Inconel | Semi-circular | 355 | 141.4 | 0.188 | 386.7 |
| 2 | Inconel | Exp. loop | 355 | 114 | 1.000 | 131.1 |
| 3 | Carbon steel | Semi-circular | 355 | 141.4 | 0.309 | 391.5 |
| 4 | Carbon steel | Exp. loop | 355 | 122 | 0.953 | 129.2 |

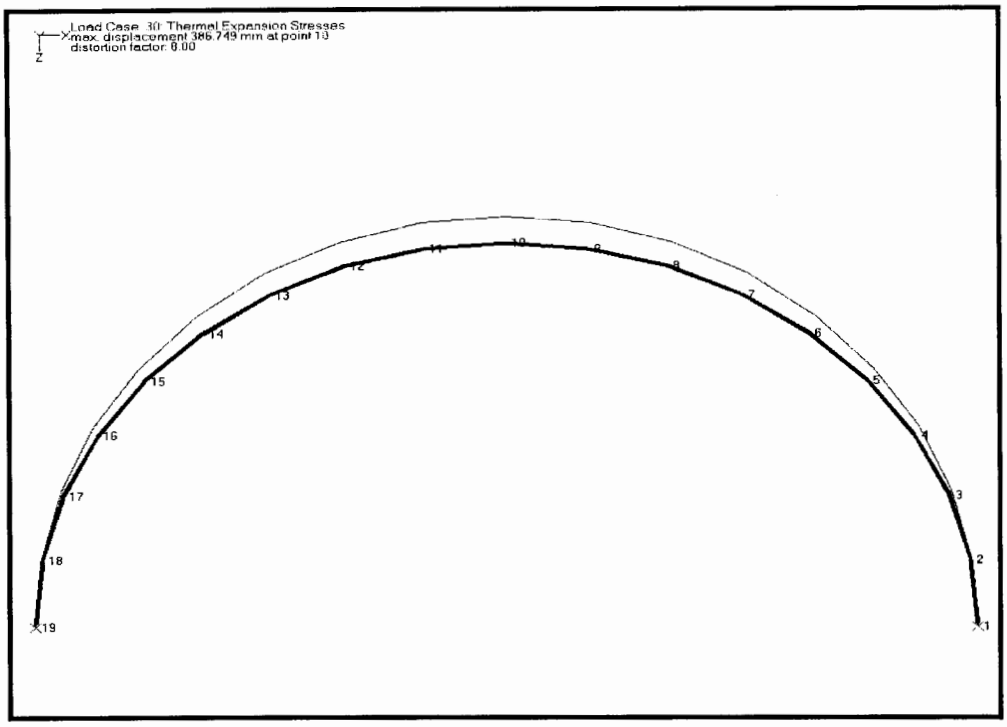


**Figure 44. Deformation for Inconel in the semi-circular configuration at 355°C operating temperature.**

Highest Stress Tables - ngnp_inconel_circ.fre

30

LOADING CASE NO: 30 THERMAL ANALYSIS - Thermal Expansion Stresses
EQUATION 10 PRIMARY + SECONDARY STRESS INTENSITY RANGE

| RANK | --POINTS-- FROM | AT | ELEMENT | EC/EH | C1 | PRESS. STRESS N/MM**2 | C2 | MOMENT STRESS N/MM**2 | STRESS RATIO |
|---|---|---|---|---|---|---|---|---|---|
| 1 | 2 | 1 | TANGENT | 1.106 | 1.000 | 68.76 | 1.000 | 17.79 | 0.188 |
| 2 | 18 | 19 | TANGENT | 1.106 | 1.000 | 68.76 | 1.000 | 17.79 | 0.188 |
| 3 | 1 | 2 | TANGENT | 1.106 | 1.000 | 68.76 | 1.000 | 12.92 | 0.178 |
| 4 | 17 | 18 | TANGENT | 1.106 | 1.000 | 68.76 | 1.000 | 12.92 | 0.178 |
| 5 | 11 | 10 | TANGENT | 1.106 | 1.000 | 68.76 | 1.000 | 10.22 | 0.172 |
| 6 | 8 | 9 | TANGENT | 1.106 | 1.000 | 68.76 | 1.000 | 9.80 | 0.171 |
| 7 | 7 | 8 | TANGENT | 1.106 | 1.000 | 68.76 | 1.000 | 8.53 | 0.168 |
| 8 | 11 | 12 | TANGENT | 1.106 | 1.000 | 68.76 | 1.000 | 8.53 | 0.168 |
| 9 | 2 | 3 | TANGENT | 1.106 | 1.000 | 68.76 | 1.000 | 8.21 | 0.168 |
| 10 | 16 | 17 | TANGENT | 1.106 | 1.000 | 68.76 | 1.000 | 8.21 | 0.168 |
| 11 | 12 | 13 | TANGENT | 1.106 | 1.000 | 68.76 | 1.000 | 6.47 | 0.164 |
| 12 | 6 | 7 | TANGENT | 1.106 | 1.000 | 68.76 | 1.000 | 6.47 | 0.164 |
| 13 | 3 | 4 | TANGENT | 1.106 | 1.000 | 68.76 | 1.000 | 3.78 | 0.158 |
| 14 | 15 | 16 | TANGENT | 1.106 | 1.000 | 68.76 | 1.000 | 3.78 | 0.158 |
| 15 | 13 | 14 | TANGENT | 1.106 | 1.000 | 68.76 | 1.000 | 3.67 | 0.158 |
| 16 | 5 | 6 | TANGENT | 1.106 | 1.000 | 68.76 | 1.000 | 3.67 | 0.158 |
| 17 | 14 | 15 | TANGENT | 1.106 | 1.000 | 68.76 | 1.000 | 0.22 | 0.150 |
| 18 | 4 | 5 | TANGENT | 1.106 | 1.000 | 68.76 | 1.000 | 0.22 | 0.150 |

**Figure 45. Highest calculated stresses for Inconel in the semi-circular configuration at 355°C operating temperature.**

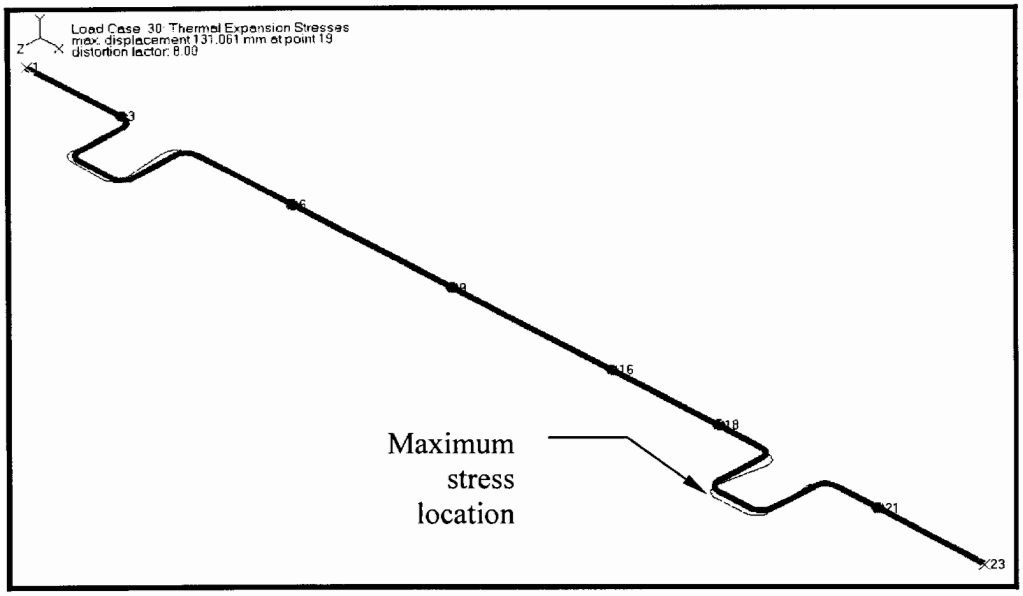


**Figure 46. Deformation for Inconel in the expansion loop configuration at 355°C operating temperature.**

Highest Stress Tables - ngnp_inconel_exp_loop.fre

30

LOADING CASE NO. 30 THERMAL ANALYSIS - Thermal Expansion Stresses
EQUATION 10 PRIMARY + SECONDARY STRESS INTENSITY RANGE

| RANK | --POINTS-- FROM | AT | ELEMENT | EC/EH | C1 | PRESS. STRESS N/MM**2 | C2 | MOMENT STRESS N/MM**2 | STRESS RATIO |
|---|---|---|---|---|---|---|---|---|---|
| 1 | 19BB | 19C | BEND | 1.106 | 1.115 | 76.68 | 2.857 | 382.69 | 1.000 |
| 2 | 19D | 20 | BEND | 1.106 | 1.115 | 76.68 | 2.857 | 379.40 | 0.993 |
| 3 | 4D | 5 | BEND | 1.106 | 1.115 | 76.68 | 2.857 | 366.52 | 0.965 |
| 4 | 4A | 3 | BEND | 1.106 | 1.115 | 76.68 | 2.857 | 351.16 | 0.931 |
| 5 | 4BB | 4C | BEND | 1.106 | 1.115 | 76.68 | 2.857 | 301.12 | 0.822 |
| 6 | 5 | 4D | BEND | 1.106 | 1.115 | 76.68 | 2.857 | 286.87 | 0.791 |
| 7 | 19C | 19BB | BEND | 1.106 | 1.115 | 76.68 | 2.857 | 282.34 | 0.781 |
| 8 | 20 | 19D | BEND | 1.106 | 1.115 | 76.68 | 2.857 | 276.85 | 0.769 |
| 9 | 19EE | 19F | BEND | 1.106 | 1.115 | 76.68 | 2.857 | 231.49 | 0.671 |
| 10 | 3 | 4A | BEND | 1.106 | 1.115 | 76.68 | 2.857 | 227.91 | 0.663 |
| 11 | 19A | 19 | BEND | 1.106 | 1.115 | 76.68 | 2.857 | 223.80 | 0.654 |
| 12 | 4EE | 4F | BEND | 1.106 | 1.115 | 76.68 | 2.857 | 198.57 | 0.599 |
| 13 | 4C | 4BB | BEND | 1.106 | 1.115 | 76.68 | 2.857 | 177.88 | 0.554 |
| 14 | 19F | 19EE | BEND | 1.106 | 1.115 | 76.68 | 2.857 | 128.94 | 0.448 |
| 15 | 20 | 19C | TANGENT | 1.106 | 1.000 | 68.76 | 1.000 | 133.94 | 0.441 |
| 16 | 19C | 20 | TANGENT | 1.106 | 1.000 | 68.76 | 1.000 | 132.78 | 0.439 |
| 17 | 19 | 19A | BEND | 1.106 | 1.115 | 76.68 | 2.857 | 123.45 | 0.436 |
| 18 | 4C | 5 | TANGENT | 1.106 | 1.000 | 68.76 | 1.000 | 128.28 | 0.429 |
| 19 | 4F | 4EE | BEND | 1.106 | 1.115 | 76.68 | 2.857 | 118.92 | 0.426 |
| 20 | 2 | 3 | TANGENT | 1.106 | 1.000 | 68.76 | 1.000 | 122.90 | 0.417 |

**Figure 47. Highest calculated stresses for Inconel in the expansion loop configuration at 355°C operating temperature.**

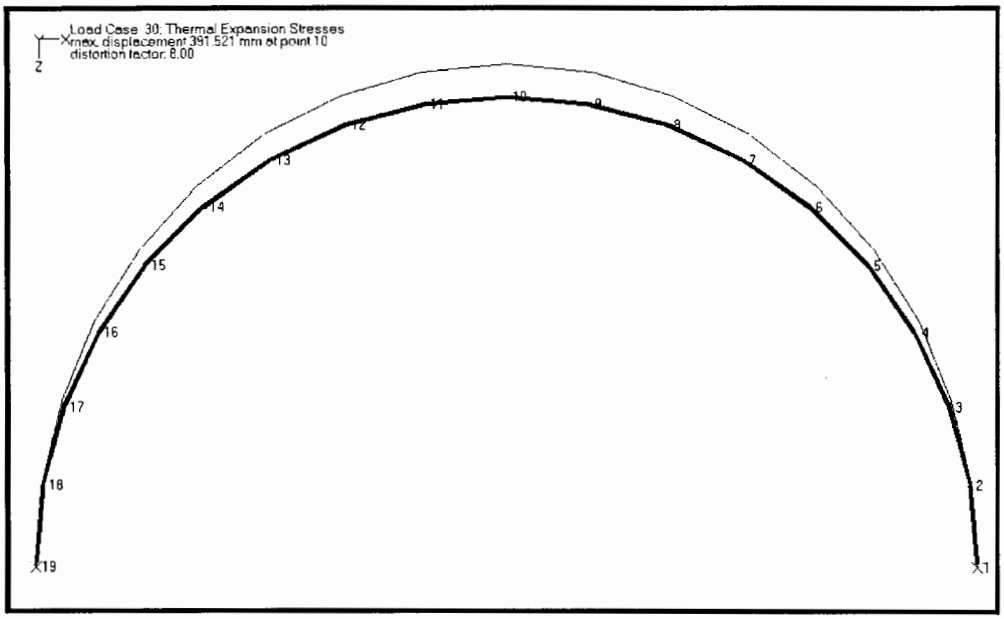


**Figure 48. Deformation for carbon steel in the semi-circular configuration at 355°C operating temperature.**

Highest Stress Tables - ngnp_steel_circ.fre

30

LOADING CASE NO. 30 THERMAL ANALYSIS - Thermal Expansion Stresses
EQUATION 10 PRIMARY + SECONDARY STRESS INTENSITY RANGE

| RANK | --POINTS-- FROM | AT | ELEMENT | EC/EH | C1 | PRESS. STRESS N/MM**2 | C2 | MOMENT STRESS N/MM**2 | STRESS RATIO |
|---|---|---|---|---|---|---|---|---|---|
| 1 | 2 | 1 | TANGENT | 1.133 | 1.000 | 68.76 | 1.000 | 17.25 | 0.309 |
| 2 | 18 | 19 | TANGENT | 1.133 | 1.000 | 68.76 | 1.000 | 17.25 | 0.309 |
| 3 | 1 | 2 | TANGENT | 1.133 | 1.000 | 68.76 | 1.000 | 12.53 | 0.292 |
| 4 | 17 | 18 | TANGENT | 1.133 | 1.000 | 68.76 | 1.000 | 12.53 | 0.292 |
| 5 | 9 | 10 | TANGENT | 1.133 | 1.000 | 68.76 | 1.000 | 9.91 | 0.283 |
| 6 | 8 | 9 | TANGENT | 1.133 | 1.000 | 68.76 | 1.000 | 9.50 | 0.281 |
| 7 | 10 | 11 | TANGENT | 1.133 | 1.000 | 68.76 | 1.000 | 9.50 | 0.281 |
| 8 | 7 | 8 | TANGENT | 1.133 | 1.000 | 68.76 | 1.000 | 8.27 | 0.277 |
| 9 | 11 | 12 | TANGENT | 1.133 | 1.000 | 68.76 | 1.000 | 8.27 | 0.277 |
| 10 | 2 | 3 | TANGENT | 1.133 | 1.000 | 68.76 | 1.000 | 7.96 | 0.276 |
| 11 | 16 | 17 | TANGENT | 1.133 | 1.000 | 68.76 | 1.000 | 7.96 | 0.276 |
| 12 | 12 | 13 | TANGENT | 1.133 | 1.000 | 68.76 | 1.000 | 6.27 | 0.270 |
| 13 | 6 | 7 | TANGENT | 1.133 | 1.000 | 68.76 | 1.000 | 6.27 | 0.270 |
| 14 | 3 | 4 | TANGENT | 1.133 | 1.000 | 68.76 | 1.000 | 3.67 | 0.260 |
| 15 | 15 | 16 | TANGENT | 1.133 | 1.000 | 68.76 | 1.000 | 3.67 | 0.260 |
| 16 | 5 | 6 | TANGENT | 1.133 | 1.000 | 68.76 | 1.000 | 3.56 | 0.260 |
| 17 | 13 | 14 | TANGENT | 1.133 | 1.000 | 68.76 | 1.000 | 3.56 | 0.260 |
| 18 | 14 | 15 | TANGENT | 1.133 | 1.000 | 68.76 | 1.000 | 0.21 | 0.248 |
| 19 | 4 | 5 | TANGENT | 1.133 | 1.000 | 68.76 | 1.000 | 0.21 | 0.248 |

**Figure 49. Highest calculated stresses for carbon steel in the semi-circular configuration at 355°C operating temperature.**

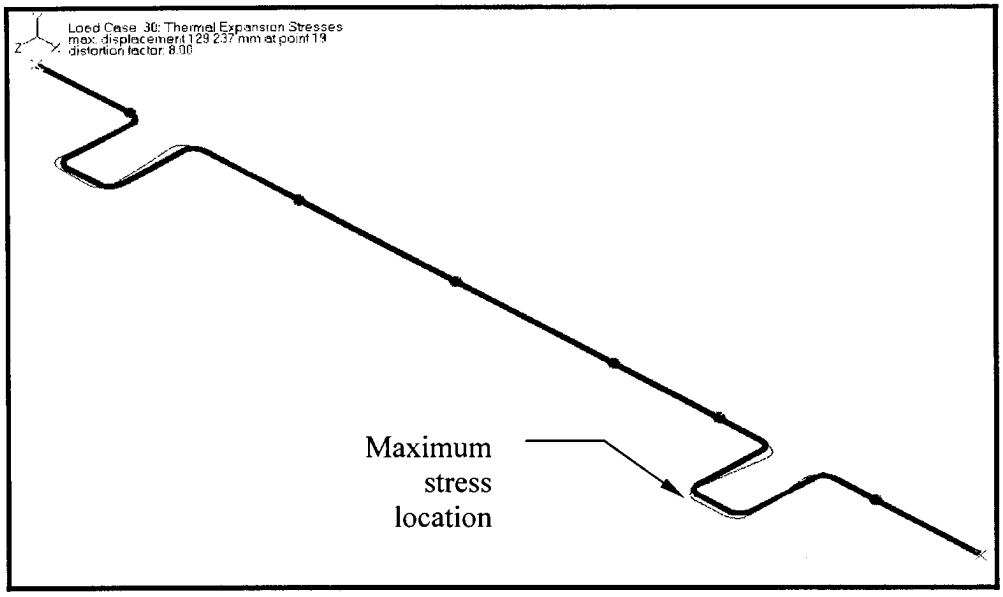


**Figure 50. Deformation for carbon steel in the expansion loop configuration at 355°C operating temperature.**

Highest Stress Tables - ngnp_steel_exp_loop.fre

30

LOADING CASE NO. 30 THERMAL ANALYSIS - Thermal Expansion Stresses
EQUATION 10 PRIMARY + SECONDARY STRESS INTENSITY RANGE

| RANK | --POINTS-- FROM | AT | ELEMENT | EC/EH | C1 | PRESS. STRESS N/MM**2 | C2 | MOMENT STRESS N/MM**2 | STRESS RATIO |
|---|---|---|---|---|---|---|---|---|---|
| 1 | 19BB | 19C | BEND | 1.133 | 1.115 | 76.68 | 2.857 | 188.16 | 0.953 |
| 2 | 19D | 20 | BEND | 1.133 | 1.115 | 76.68 | 2.857 | 186.49 | 0.947 |
| 3 | 4D | 5 | BEND | 1.133 | 1.115 | 76.68 | 2.857 | 184.05 | 0.938 |
| 4 | 4A | 3 | BEND | 1.133 | 1.115 | 76.68 | 2.857 | 179.43 | 0.921 |
| 5 | 5 | 4D | BEND | 1.133 | 1.115 | 76.68 | 2.857 | 163.99 | 0.866 |
| 6 | 19C | 19BB | BEND | 1.133 | 1.115 | 76.68 | 2.857 | 157.80 | 0.843 |
| 7 | 20 | 19D | BEND | 1.133 | 1.115 | 76.68 | 2.857 | 155.02 | 0.833 |
| 8 | 4BB | 4C | BEND | 1.133 | 1.115 | 76.68 | 2.857 | 151.46 | 0.821 |
| 9 | 3 | 4A | BEND | 1.133 | 1.115 | 76.68 | 2.857 | 137.65 | 0.771 |
| 10 | 19EE | 19F | BEND | 1.133 | 1.115 | 76.68 | 2.857 | 123.78 | 0.721 |
| 11 | 19A | 19 | BEND | 1.133 | 1.115 | 76.68 | 2.857 | 119.89 | 0.707 |
| 12 | 4C | 4BB | BEND | 1.133 | 1.115 | 76.68 | 2.857 | 109.68 | 0.670 |
| 13 | 4EE | 4F | BEND | 1.133 | 1.115 | 76.68 | 2.857 | 103.39 | 0.648 |
| 14 | 19F | 19EE | BEND | 1.133 | 1.115 | 76.68 | 2.857 | 92.31 | 0.608 |
| 15 | 19 | 19A | BEND | 1.133 | 1.115 | 76.68 | 2.857 | 89.53 | 0.598 |
| 16 | 4F | 4EE | BEND | 1.133 | 1.115 | 76.68 | 2.857 | 83.34 | 0.576 |
| 17 | 20 | 19C | TANGENT | 1.133 | 1.000 | 68.76 | 1.000 | 65.85 | 0.484 |
| 18 | 19C | 20 | TANGENT | 1.133 | 1.000 | 68.76 | 1.000 | 65.27 | 0.482 |
| 19 | 4C | 5 | TANGENT | 1.133 | 1.000 | 68.76 | 1.000 | 64.41 | 0.479 |
| 20 | 2 | 3 | TANGENT | 1.133 | 1.000 | 68.76 | 1.000 | 62.80 | 0.473 |

**Figure 51. Highest calculated stresses for carbon steel in the expansion loop configuration at 355°C operating temperature.**

Inconel 617 has a much higher allowable temperature range than carbon steel. Consequently, the high temperature cases were not performed for carbon steel. The results with carbon steel and

Inconel 617 are reasonably comparable for the lower temperature cases. Because of its lower cost and similar performance, carbon steel is preferred over Inconel 617 for the IHTL if the internal insulation can keep the metal operating temperatures sufficiently low.

The lengths of the IHTL legs must be increased over the required separation distance between the nuclear and hydrogen plants to accommodate the stresses associated with thermal expansion. For the cases with carbon steel and an operating temperature of 355 °C, the increase in length varies from 35 to 60%.

The semi-circular configuration has a lower maximum stress than the expansion loop configuration.

**Concentric Configuration**

This concentric pipe configuration was modeled with the hot and cold leg piping lines overlaid (coincident nodes). The relative displacement between the two legs was limited to the free space available in the cold leg (calculated as half the difference between the inner diameter of the cold leg and the outer diameter of the hot leg, 78.5 mm). With the only load considered for this model being thermal expansion, no spacers were needed between the two legs to keep the pipes from colliding (the calculated relative displacement between the two pipes was less than the allowable value). However it is believed that the inclusion of additional loads in the analysis, such as dead and seismic, will conclude that spacers between the two legs will be required to keep the pipes from colliding. Spacers that act as 2-way restraints, allowing axial displacement of the inner hot leg, are recommended.

The piping parameters used for the concentric configuration are listed in Table 35.

**Table 35.** Parameters of Concentric Pipe

| Parameter | Value |
|---|---|
| Inner Pipe (hot leg) outside diameter | 361.6 mm |
| Outer Pipe (cold leg) outside diameter | 586.9 mm |
| Inner Pipe (hot leg) wall thickness | 6.6 mm |
| Outer Pipe (cold leg) wall thickness | 31.1 mm |
| Pipe length | 90 m |
| Inner Pipe (hot leg) Operating temperature | 488 °C |
| Outer Pipe (cold leg) Operating temperature | 354 °C |
| Inner Pipe (hot leg) Operating pressure | 6.9 MPa |
| Outer Pipe (cold leg) Operating pressure | 7.0 MPa |
| Ambient temperature | 20°C |

Concentric configuration was modeled only with Inconel 617 due to the high operating temperature of the hot leg (488°C). A model with the hot leg made of Inconel 617 and the cold leg made of carbon steel was not modeled since it was considered important to have both legs made of the same materials in order to get similar expansions.

Expansion loops were included in the model and the lengths of the loops were adjusted so the maximum calculated stress is about equal to the maximum allowable stress. Industry typically uses expansion loops to build in some compliance in high temperature piping.

*Concentric Pipe Case 1 – Inconel 617 with Expansion Loops*

The results are presented below; Figure 52 shows the deformation and Figure 53 lists the maximum stress locations. In Figure 52, the purple line shows the exaggerated displacement of the hot and cold legs (distortion factor of 32) and the black line shows the undeformed pipes. The high stress table in Figure 53 ranks the elements with the highest calculated stress values; the far right column in this table shows the ratio of the calculated stress to the allowable stress.

There are three expansion loops starting at 10 m, 45 m and 75 m from the first anchor; all are 5 m long and jog 12 m from the main pipeline. The total estimated pipe length is 162 m for each leg. The high stress locations occur at the elbows of the expansion loops.

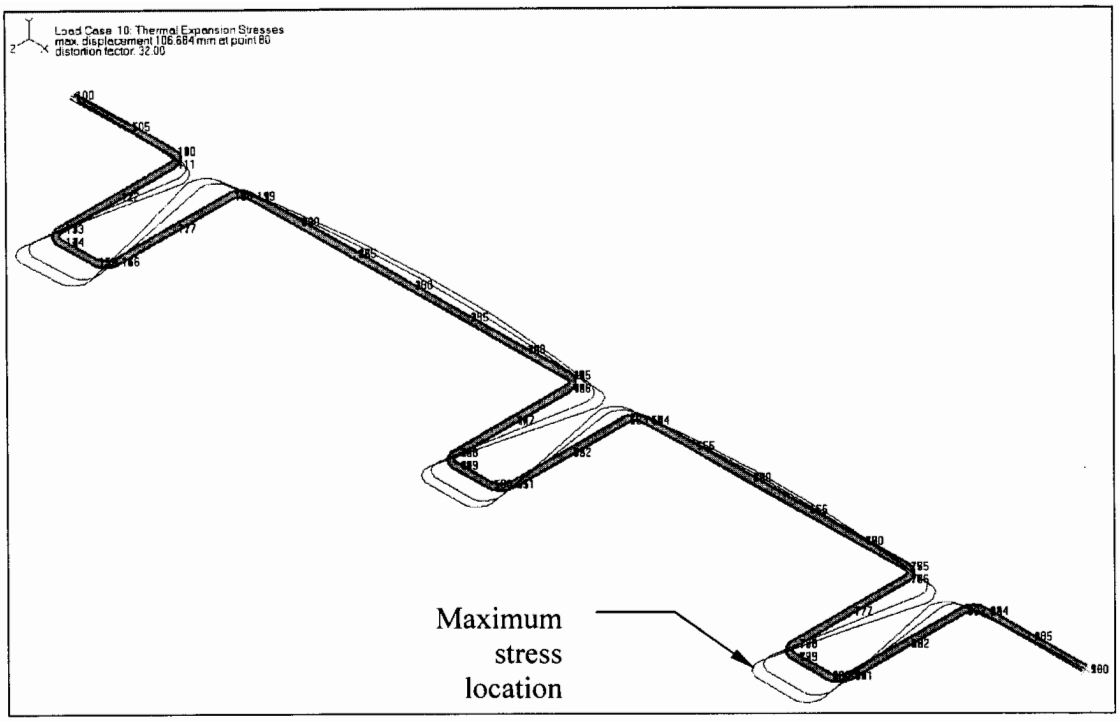


**Figure 52. Deformation Plot for Concentric Configuration with Inconel.**

Highest Stress Tables - ngnp_sit2_3loop.fre

10

LOADING CASE NO. 10 THERMAL ANALYSIS - Thermal Expansion Stresses
EQUATION 10 PRIMARY + SECONDARY STRESS INTENSITY RANGE

| RANK | --POINTS-- FROM | AT | ELEMENT | EC/EH | C1 | PRESS. STRESS N/MM**2 | C2 | MOMENT STRESS N/MM**2 | STRESS RATIO |
|---|---|---|---|---|---|---|---|---|---|
| 1 | 13 | 14 | BEND | 1.160 | 1.108 | 209.41 | 5.528 | 181.74 | 0.895 |
| 2 | 16 | 15 | BEND | 1.160 | 1.108 | 209.41 | 5.528 | 181.59 | 0.895 |
| 3 | 48 | 49 | BEND | 1.160 | 1.108 | 209.41 | 5.528 | 179.97 | 0.891 |
| 4 | 51 | 50 | BEND | 1.160 | 1.108 | 209.41 | 5.528 | 179.82 | 0.891 |
| 5 | 78 | 79 | BEND | 1.160 | 1.108 | 209.41 | 5.528 | 178.45 | 0.888 |
| 6 | 81 | 80 | BEND | 1.160 | 1.108 | 209.41 | 5.528 | 178.30 | 0.888 |
| 7 | 14 | 13 | BEND | 1.160 | 1.108 | 209.41 | 5.528 | 158.29 | 0.842 |
| 8 | 15 | 16 | BEND | 1.160 | 1.108 | 209.41 | 5.528 | 158.04 | 0.841 |
| 9 | 49 | 48 | BEND | 1.160 | 1.108 | 209.41 | 5.528 | 156.52 | 0.838 |
| 10 | 50 | 51 | BEND | 1.160 | 1.108 | 209.41 | 5.528 | 156.26 | 0.837 |
| 11 | 79 | 78 | BEND | 1.160 | 1.108 | 209.41 | 5.528 | 155.00 | 0.834 |
| 12 | 80 | 81 | BEND | 1.160 | 1.108 | 209.41 | 5.528 | 154.75 | 0.834 |
| 13 | 83 | 84 | BEND | 1.160 | 1.108 | 209.41 | 5.528 | 103.83 | 0.717 |
| 14 | 76 | 75 | BEND | 1.160 | 1.108 | 209.41 | 5.528 | 103.48 | 0.716 |
| 15 | 53 | 54 | BEND | 1.160 | 1.108 | 209.41 | 5.528 | 102.32 | 0.714 |
| 16 | 46 | 45 | BEND | 1.160 | 1.108 | 209.41 | 5.528 | 101.96 | 0.713 |
| 17 | 18 | 19 | BEND | 1.160 | 1.108 | 209.41 | 5.528 | 100.54 | 0.710 |
| 18 | 11 | 10 | BEND | 1.160 | 1.108 | 209.41 | 5.528 | 100.19 | 0.709 |
| 19 | 84 | 83 | BEND | 1.160 | 1.108 | 209.41 | 5.528 | 80.28 | 0.663 |
| 20 | 75 | 76 | BEND | 1.160 | 1.108 | 209.41 | 5.528 | 80.03 | 0.663 |

**Figure 53. Highest Stress Table for Concentric Configuration with Inconel**

## Jacketed Configuration

The piping lines in the jacketed configuration were modeled similarly to the concentric configuration with the two lines overlaid. Similar to the concentric configuration, the results for the two cases modeled below also showed that no spacers were needed between the hot leg and jacket to limit their relative displacement. See this previous discussion for more details and recommendations for further analysis.

The piping parameters used for the jacketed configuration are listed in Table 36.

**Table 36.** Jacketed Configuration

| Parameter | Value |
|---|---|
| Inner Pipe (hot leg) outside diameter | 369.6 mm |
| Jacket outside diameter | 450.5 mm |
| Inner Pipe (hot leg) wall thickness | 19.8 mm |
| Jacket wall thickness | 12.75 mm |
| Pipe length | 90 m |
| Inner Pipe (hot leg) Operating temperature | 355 °C |
| Jacket Operating temperature | 355 °C |
| Inner Pipe (hot leg) Operating pressure | 6.9 MPa |
| Jacket Operating pressure | 3.45 MPa |
| Ambient temperature | 20°C |

Since it was noted that geometry and operating conditions of the legs can be assumed to be the same as in the parallel configuration , the cold leg geometry was not modeled since the results would be the same for this case as those found for the parallel configuration (if a parallel arrangement is desired, the cold leg can use the same layout shown below for the jacketed hot leg since this latter leg has the less conservative parameters). The hot leg behaves differently in this configuration (compared to the parallel configuration) due to the presence of the jacket (this larger pipe needed larger expansion loops in order to meet the stress criteria).

The geometry and operating conditions of the jacket were specified in Table 31. These included the following: the wall thickness of the jacket is 3% of its inner diameter, the operating pressure is half of the value in the hot leg, and the operating temperature will be the same as the hot leg. The jacket inner diameter was assumed to be 400 mm which would only have allowed 2.7 mm of differential displacement between the hot leg and jacket. For this model, the jacket inner diameter was increased to 425 mm to allow 15.2 mm of differential displacement.

The jacketed configuration was modeled using both Inconel 617 and carbon steel (SA-106 Grade B) with expansion loops. Each of these cases is presented below; the first is modeled with Inconel 617 and the second is modeled with carbon steel.

*Jacketed Pipe Case 1 – Inconel 617 with Expansion Loops*

Figure 54 shows the deformation using Inconel 617 pipe for both the hot leg and jacket. There are two expansion loops starting at 10 m and 75 m from the first anchor; both are 5 m long and jog 7 m from the main pipeline. The total estimated pipe length is 118 m for each leg. Figure 55 shows the maximum stress table for this case.

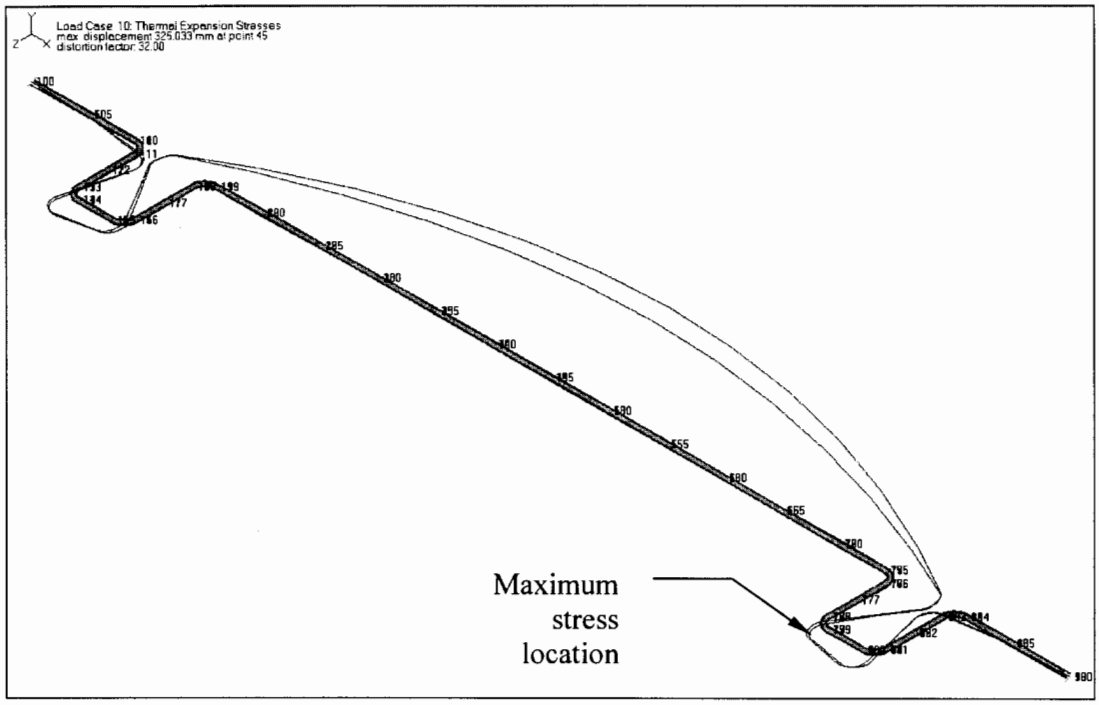


**Figure 54. Deformation Plot for Jacketed Configuration with Inconel 617 Pipe**

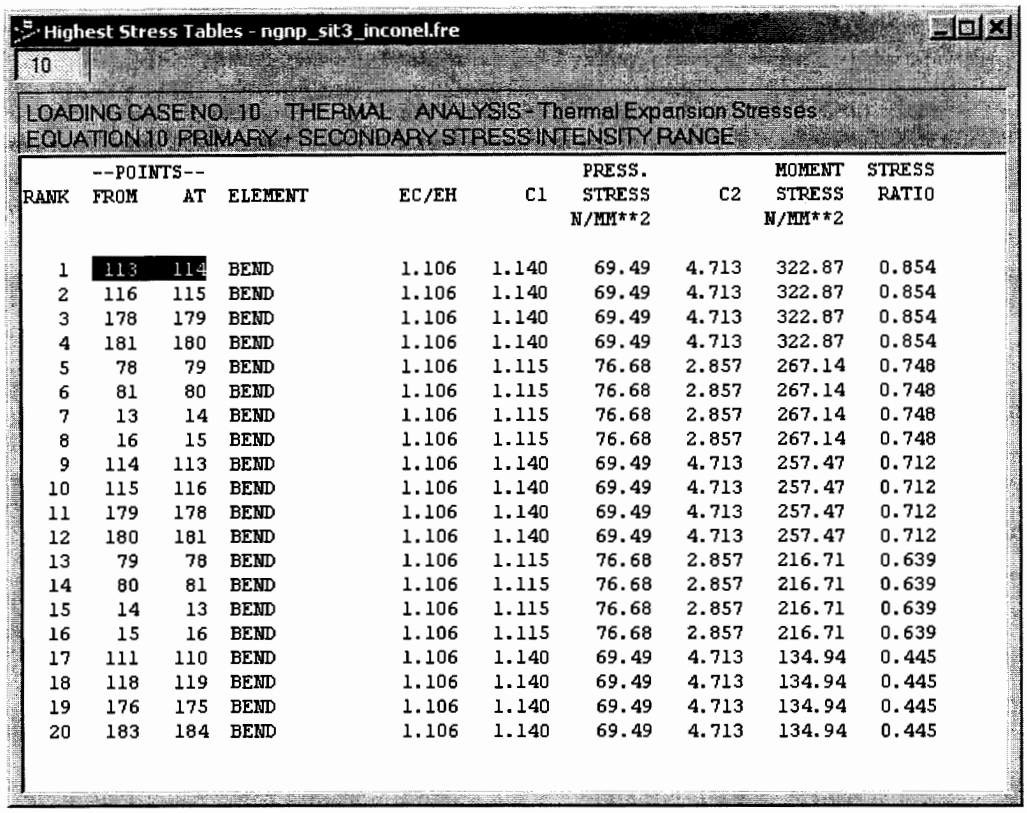

Highest Stress Tables - ngnp_sit3_inconel.fre

10

LOADING CASE NO. 10 THERMAL ANALYSIS - Thermal Expansion Stresses
EQUATION 10 PRIMARY + SECONDARY STRESS INTENSITY RANGE

| RANK | --POINTS-- FROM | AT | ELEMENT | EC/EH | C1 | PRESS. STRESS N/MM**2 | C2 | MOMENT STRESS N/MM**2 | STRESS RATIO |
|---|---|---|---|---|---|---|---|---|---|
| 1 | 113 | 114 | BEND | 1.106 | 1.140 | 69.49 | 4.713 | 322.87 | 0.854 |
| 2 | 116 | 115 | BEND | 1.106 | 1.140 | 69.49 | 4.713 | 322.87 | 0.854 |
| 3 | 178 | 179 | BEND | 1.106 | 1.140 | 69.49 | 4.713 | 322.87 | 0.854 |
| 4 | 181 | 180 | BEND | 1.106 | 1.140 | 69.49 | 4.713 | 322.87 | 0.854 |
| 5 | 78 | 79 | BEND | 1.106 | 1.115 | 76.68 | 2.857 | 267.14 | 0.748 |
| 6 | 81 | 80 | BEND | 1.106 | 1.115 | 76.68 | 2.857 | 267.14 | 0.748 |
| 7 | 13 | 14 | BEND | 1.106 | 1.115 | 76.68 | 2.857 | 267.14 | 0.748 |
| 8 | 16 | 15 | BEND | 1.106 | 1.115 | 76.68 | 2.857 | 267.14 | 0.748 |
| 9 | 114 | 113 | BEND | 1.106 | 1.140 | 69.49 | 4.713 | 257.47 | 0.712 |
| 10 | 115 | 116 | BEND | 1.106 | 1.140 | 69.49 | 4.713 | 257.47 | 0.712 |
| 11 | 179 | 178 | BEND | 1.106 | 1.140 | 69.49 | 4.713 | 257.47 | 0.712 |
| 12 | 180 | 181 | BEND | 1.106 | 1.140 | 69.49 | 4.713 | 257.47 | 0.712 |
| 13 | 79 | 78 | BEND | 1.106 | 1.115 | 76.68 | 2.857 | 216.71 | 0.639 |
| 14 | 80 | 81 | BEND | 1.106 | 1.115 | 76.68 | 2.857 | 216.71 | 0.639 |
| 15 | 14 | 13 | BEND | 1.106 | 1.115 | 76.68 | 2.857 | 216.71 | 0.639 |
| 16 | 15 | 16 | BEND | 1.106 | 1.115 | 76.68 | 2.857 | 216.71 | 0.639 |
| 17 | 111 | 110 | BEND | 1.106 | 1.140 | 69.49 | 4.713 | 134.94 | 0.445 |
| 18 | 118 | 119 | BEND | 1.106 | 1.140 | 69.49 | 4.713 | 134.94 | 0.445 |
| 19 | 176 | 175 | BEND | 1.106 | 1.140 | 69.49 | 4.713 | 134.94 | 0.445 |
| 20 | 183 | 184 | BEND | 1.106 | 1.140 | 69.49 | 4.713 | 134.94 | 0.445 |

**Figure 55. Highest Stress Table for Jacketed Configuration with Inconel 617 Pipe**

*Jacketed Pipe Case 2 – Carbon Steel with Expansion Loops*

Figure 56 shows deformation using carbon steel pipe for both the hot leg and jacket. There are two expansion loops starting at 10 m and 75 m from the first anchor; both are 5 m long and jog 10 m from the main pipeline. The total estimated pipe length is 130 m. Figure 57 shows the maximum stress table for this case.

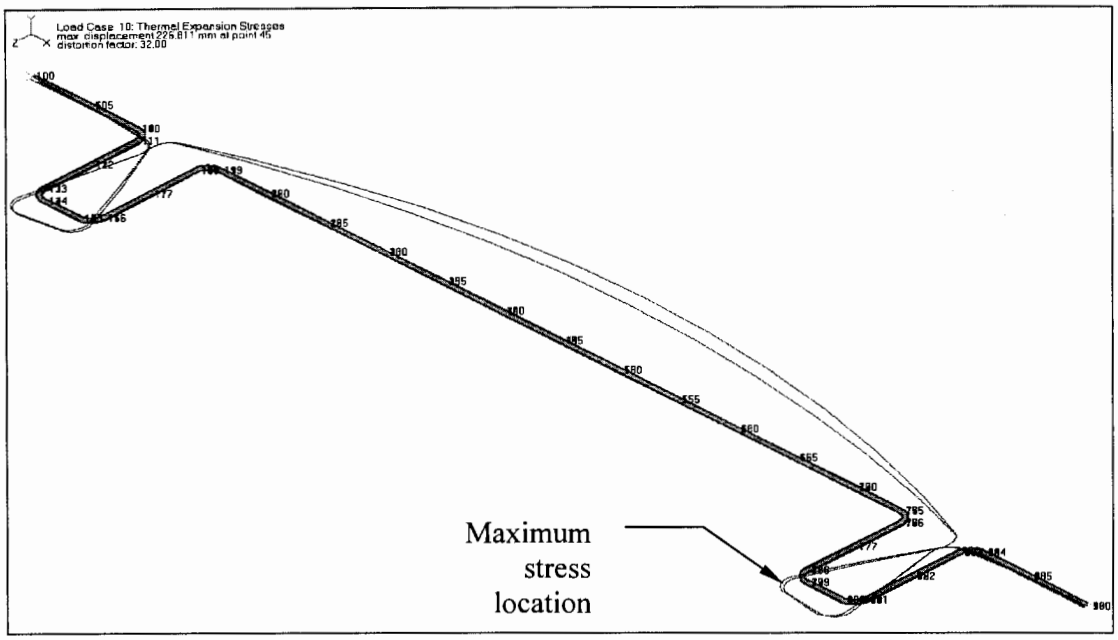


**Figure 56. Deformation Plot for Jacketed Configuration with Carbon Steel Pipe.**

Highest Stress Tables - ngnp_sit3_steel.fre

10

LOADING CASE NO. 10 THERMAL ANALYSIS - Thermal Expansion Stresses
EQUATION 10 PRIMARY + SECONDARY STRESS INTENSITY RANGE

| RANK | --POINTS-- FROM | AT | ELEMENT | EC/EH | C1 | PRESS. STRESS N/MM**2 | C2 | MOMENT STRESS N/MM**2 | STRESS RATIO |
|---|---|---|---|---|---|---|---|---|---|
| 1 | 178 | 179 | BEND | 1.133 | 1.140 | 69.49 | 4.713 | 200.54 | 0.971 |
| 2 | 181 | 180 | BEND | 1.133 | 1.140 | 69.49 | 4.713 | 200.54 | 0.971 |
| 3 | 113 | 114 | BEND | 1.133 | 1.140 | 69.49 | 4.713 | 200.54 | 0.971 |
| 4 | 116 | 115 | BEND | 1.133 | 1.140 | 69.49 | 4.713 | 200.54 | 0.971 |
| 5 | 179 | 178 | BEND | 1.133 | 1.140 | 69.49 | 4.713 | 171.58 | 0.867 |
| 6 | 180 | 181 | BEND | 1.133 | 1.140 | 69.49 | 4.713 | 171.58 | 0.867 |
| 7 | 114 | 113 | BEND | 1.133 | 1.140 | 69.49 | 4.713 | 171.58 | 0.867 |
| 8 | 115 | 116 | BEND | 1.133 | 1.140 | 69.49 | 4.713 | 171.58 | 0.867 |
| 9 | 78 | 79 | BEND | 1.133 | 1.115 | 76.68 | 2.857 | 160.18 | 0.852 |
| 10 | 81 | 80 | BEND | 1.133 | 1.115 | 76.68 | 2.857 | 160.18 | 0.852 |
| 11 | 13 | 14 | BEND | 1.133 | 1.115 | 76.68 | 2.857 | 160.18 | 0.852 |
| 12 | 16 | 15 | BEND | 1.133 | 1.115 | 76.68 | 2.857 | 160.18 | 0.852 |
| 13 | 79 | 78 | BEND | 1.133 | 1.115 | 76.68 | 2.857 | 138.42 | 0.774 |
| 14 | 80 | 81 | BEND | 1.133 | 1.115 | 76.68 | 2.857 | 138.42 | 0.774 |
| 15 | 14 | 13 | BEND | 1.133 | 1.115 | 76.68 | 2.857 | 138.42 | 0.774 |
| 16 | 15 | 16 | BEND | 1.133 | 1.115 | 76.68 | 2.857 | 138.42 | 0.774 |
| 17 | 111 | 110 | BEND | 1.133 | 1.140 | 69.49 | 4.713 | 89.11 | 0.570 |
| 18 | 118 | 119 | BEND | 1.133 | 1.140 | 69.49 | 4.713 | 89.11 | 0.570 |
| 19 | 176 | 175 | BEND | 1.133 | 1.140 | 69.49 | 4.713 | 89.11 | 0.570 |
| 20 | 183 | 184 | BEND | 1.133 | 1.140 | 69.49 | 4.713 | 89.11 | 0.570 |

**Figure 57. Highest Stress Table for Jacketed Configuration with Carbon Steel Pipe**

Table 37 summarizes the results from one case with the concentric configuration and two cases with the jacketed configuration considered in this study.

Table 37. Summary of results from concentric configuration and jacketed configuration.

| Configuration | Case | Material | Pipe Length (m) | Max. Code Stress Ratio | Max. Deformation (mm) |
|---|---|---|---|---|---|
| Concentric | 1, Exp. Loop | Inconel | 162 | 0.895 | 106.7 |
| Jacketed | 1, Exp. Loop | Inconel | 118 | 0.854 | 325.0 |
| Jacketed | 2, Exp. Loop | Carbon Steel | 130 | 0.971 | 226.8 |

The carbon steel and the Inconel are reasonably comparable for the operating temperature and loads (pressure and thermal expansion only) we investigated. Inconel offers some advantages over carbon steel in that it has better strength at higher temperatures and better corrosion resistance. The semi-circular configuration typically has the lower stresses than the expansion loop, but requires more pipe length. Fabrication and installation costs may be higher for the semi-circular compared to the expansion loop, but it is more efficient at higher temperatures.

The concentric configuration requires the greatest amount of pipe due to the higher operating temperature of the hot leg metal. The carbon steel and the Inconel are reasonably comparable for the jacketed configuration. The concentric configuration also has disadvantages in terms of installation and inspection.

This pipe stress analysis did not account for any dynamic loads such as earthquake or wind loads, deadweight or supports. Furthermore, spacers may need to be added when the analysis accounts for these additional loads in order to prevent the pipe walls from colliding. All of these factors will need to be considered in the final design.

## 5.3 Economic Analyses

Simple economic analyses were performed to estimate the cost of various configurations of the IHTL, including the hot and cold leg piping, the IHX, and the circulator.

The cost estimates for the hot and cold leg piping were based on data presented by Delene and Hudson (1993). Cost data were provided for three different sizes of non-nuclear carbon steel pipes, including installation, in 1992$ per unit length. The pipe sizes included 4-inch schedule 40, 12-inch schedule 80, and 20-inch schedule 120. Linear regression analysis showed that both the commodity and installation costs were adequately correlated using the metal cross sectional area, $A_x$, where

$$A_x = \pi(D_o^2 - D_i^2)/4 \tag{45}$$

and $D_o$ and $D_i$, are the outer and inner diameters of the pipe, respectively. Although the data were limited, the $R^2$ value of the fits was at least 0.995 for both the commodity and the installation costs. The two cost components were combined to obtain a total cost, which was then multiplied by 1.442 to

account for the change in the Consumer Price Index between January 1992 and January 2006. The resulting correlation for total cost, C in 2006$ per meter, is

$$C(\$/m) = 251.05 + 1.171E5A_x \quad . \tag{46}$$

Note that Equation 46 neglects the cost of the insulation.

Richards et al. (2006) presented cost estimates for the piping in the IHTL of a single-purpose facility dedicated to hydrogen production. The cost from Equation 46 was about 20% higher than the estimate from Richards et al. This level of agreement was considered adequate to justify using Equation 46 for this analysis.

The piping costs for the configurations described in Section 5.1 were estimated using Equation 46. Figure 58 presents results for the case with helium as a working fluid. The piping cost is a strong function of the separation distance, and to a lesser extent, power. Increasing the separation distance from 90 to 500 m, which corresponds to less than a factor of six increase in length, results in a factor of twenty increase in cost. Thus, there is a strong economic incentive to reduce the separation distance. Increasing the loop power by a factor of 12 causes the cost to increase by a factor of about 6. The differences between the parallel and concentric configurations were relatively small. At the best-estimate separation distance of 90 m, the piping costs for the concentric configuration were about 40% higher than for the parallel configuration. The differences between configurations decreased with separation distance and the costs were similar at a distance of 500 m. The results presented in Figure 56 probably underestimate the relative costs associated with the concentric configuration because Equation 46 does not account for the increased complexity in installing a concentric design.

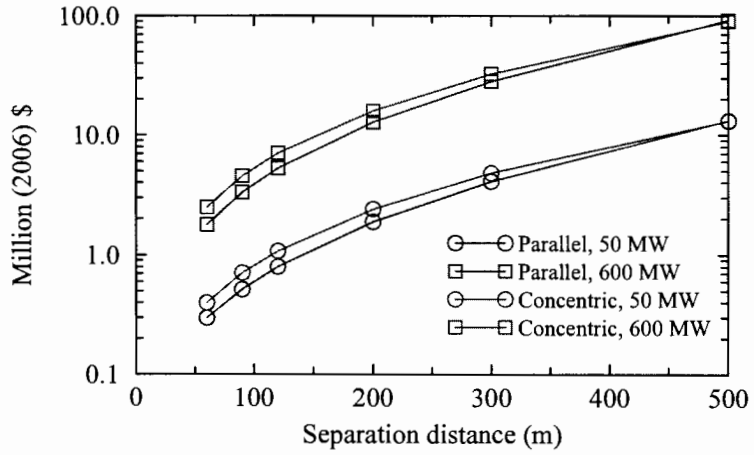


**Figure 58. The effect of configuration, power, and separation distance on IHTL piping costs (helium working fluid).**

The effect of the working fluid on the cost of the IHTL could not be reliably determined because the cost depends heavily on the piping material used. If the same material can be used with both working fluids, there is a strong economic benefit to be gained using the liquid salt. Because of the smaller diameter and thickness of the pipes, the piping cost can be reduced by a factor of 5 to 10 with liquid salt as the working fluid. However, the cost advantage of liquid salt diminishes or disappears if corrosion concerns, such as would be caused by leakage between the insulation and the pipe, require a more expensive material to be used. Material adjustment factors for components with nickel-based

alloys are generally in the range of 2 to 5 (Peters et al. 2003). The cost of the piping would be roughly the same with helium and liquid salt at a separation distance of 90 m and a 50-MW heat transport loop if the material used with the liquid salt is five times more expensive than carbon steel. Liquid salt still has up to a factor of two economic advantage at larger separation distances and for a 600-MW loop. However, if the material needs for salt compatibility require the use of a more exotic material, the cost adjustment factor could be a factor of twenty or more, and a salt-based loop could be more expensive than a helium-based loop.

Equation 46 was also used to compare the costs of the jacketed and parallel hot leg configurations. The jacketed hot leg was about 20% more expensive than the parallel configuration for a 50-MW loop at a separation distance of 90 m.

Table 38 presents cost estimates for an IHTL with a parallel configuration, a separation distance of 90 m, and with helium as the working fluid. The piping costs were determined from the results shown in Figure 56. The costs of the other components were based on estimates from Richards et al. (2006), which were generated for a 600-MW loop in an $n^{th}$-of-a-kind plant. A scaling exponent of 0.6 (Peters et al. 2003) was used to estimate the cost of the corresponding components in the 50-MW loop. Note that the total cost of the loop does not include the IHX and PHX, which are assumed to be included within the cost of the nuclear primary coolant system and the hydrogen production plant, respectively.

Table 38. Estimated IHTL costs.

| Component | Cost (M$) | |
|---|---|---|
| | 50-MW loop | 600-MW loop |
| Piping | 0.5 | 3.3 |
| Circulator | 3.9 | 17.5 |
| Helium services system | 0.2 | 1.0 |
| Isolation valves | 1.1 | 5.0 |
| Residual heat removal system | 0.9 | 4.0 |
| | | |
| Total | 6.6 | 30.8 |

The estimated piping cost corresponds to about 10% of the total for the IHTL at a separation distance of 90 m. However, the estimated piping cost jumps to about 70% of the total when the separation distance increases to 500 m.

## 6.0 CONCLUSIONS

*Three-Shaft Cycle*

The helium working fluid has the best PCU efficiency of 50.93%. The nitrogen-helium mixture gave a slightly lower cycle efficiency of 50.76%. $CO_2$ had much lower cycle efficiency at 46.73%. The turbomachinery work using $CO_2$ was approximately 8.8% lower than the work when using helium and the mixture. Dostal et al. (2004) also state that for turbomachinery of the same power, $CO_2$ is smaller than that of helium. The nitrogen-helium mixture produced the smallest total heat exchanger volume followed by helium and then $CO_2$. Although the heat exchanger volume is larger for $CO_2$, the total cost of the plant could be less than that of a He or nitrogen-helium mixture due to its smaller turbomachinery size. Parametric studies demonstrated that helium is less susceptible to changes in working conditions than $CO_2$ and the nitrogen-helium mixture. The advantage of this is reduced losses during off-normal operations; however if the reactor were to be up rated to a higher outlet temperature the increase in efficiency would not be as advantageous as for the other working fluids.

*Combined Cycle*

$CO_2$ proved to be the best working fluid in terms of efficiency, with a value of 50.50%. Helium had an efficiency of 49.10% and the nitrogen-helium mixture had an efficiency of 48.70%. The turbomachinery work using $CO_2$ was approximately 8.5% lower than the work when using helium and the mixture. $CO_2$ results in a total heat exchanger volume that was slightly larger than that of helium. The total heat exchanger volume for the combined cycle is the lowest of all the PCU configurations. It also uses existing steam cycle technology making it a very attractive candidate. Parametric studies demonstrated that the working fluids were similarly affected by the working conditions within the cycle, except that helium was less affected by pressure. The pressure study also highlighted that the combined cycle was not greatly affected by the pressure. Therefore, lower pressures could be used in the system to decrease component sizes with a small decrease in efficiency. Due to its small dependence on working conditions such as pressure and smaller heat exchanger sizes as compared to the three-shaft cycle, the combined cycle is recommended. Further exploration of this cycle could include improvements to the steam cycle efficiency by the use of feedwater heaters and reheating.

*Reheated Cycle*

Helium working fluid had the best PCU efficiency of 55.46%. The nitrogen-helium mixture gave a slightly lower efficiency of 55.19% and $CO_2$ had a much lower efficiency at 52.10%. The turbomachinery work using $CO_2$ was approximately 15.2% lower than the work when using helium and the mixture. The nitrogen-helium mixture produced the smallest total heat exchanger volume followed by $CO_2$ and then helium. A study using helium as the primary working fluid gave an efficiency of 51.54%. Comparing this to the three-shaft option efficiency of 50.93% confirms that helium is not a viable primary working fluid for the reheat option because the increased efficiency does not compensate for the increased complexity and construction cost of the cycle. The total heat exchanger volume is approximately 50% larger than that for the combined cycle.

*IHTL and HTSE*

The use of an IHTL and HTSE plant allows the simultaneous production of hydrogen and electricity. With approximately 50 MW of process heat being transferred to the HTSE facility, hydrogen can be produced at a rate of 96.42 to 113.7 kg/hr. The use of a liquid salt in the IHTL increases the overall cycle efficiency by about 1% by lowering the pumping power required in the loop. Some of the electrical power generated by the PCU must be used to power the electrolysis cell, thus decreasing the net electrical output.

*Engineering Analyses of the IHTL*

The engineering analyzes showed that the size and cost of the IHTL are strong functions of the loop power. The estimated cost of the IHTL was 6.6 M$ (in 2006$) for the IHTL in a dual-purpose facility with 50 MW dedicated for hydrogen production. The estimated cost increased to 30.8 M$ for a single-purpose facility with all 600 MW applied to hydrogen production. The above estimates assumed a parallel configuration, a 90-m separation distance between the nuclear reactor and the hydrogen production plant, helium working fluid, and that internal insulation in the pipes can be used to reduce the metal temperature sufficiently so that carbon steel could be used. The cost would be increased significantly if higher-temperature alloys are required.

The engineering analyses also showed that the size and cost of the IHTL are strong functions of the separation distance. If the separation distance were to increase to 500 m, the cost estimates would increase to 20 M$ and 120 M$ for the 50-MW and 600-MW loops, respectively. Thus, there is a strong incentive to minimize the separation distance between the nuclear reactor and the hydrogen production plant.

The differences between the parallel, jacketed, and concentric configurations were relatively small. The parallel configuration was the cheapest, with the jacketed and concentric configurations 20 to 40% more expensive.

The carbon steel and the Inconel are reasonably comparable for the operating temperature and loads (pressure and thermal expansion only) we investigated. Inconel offers some advantages over carbon steel in that it has better strength at higher temperatures and better corrosion resistance. The semi-circular configuration typically has the lower stresses than the expansion loop, but requires more pipe length. Fabrication and installation costs may be higher for the semi-circular compared to the expansion loop, but it is more efficient at higher temperatures.

The concentric configuration requires the greatest amount of pipe due to the higher operating temperature of the hot leg metal. The carbon steel and the Inconel are reasonably comparable for the jacketed configuration. The concentric configuration also has disadvantages in terms of installation and inspection.

This pipe stress analysis did not account for any dynamic loads such as earthquake or wind loads, deadweight or supports. Furthermore, spacers may need to be added when the analysis accounts for these additional loads in order to prevent the pipe walls from colliding. All of these factors will need to be considered in the final design.

The mechanical design of the IHTL piping appears feasible if the internal insulation can keep the temperatures sufficiently low. The piping lengths must be increased by 35 – 60% to accommodate the stresses associated with thermal expansion.

## 7.0 REFERENCES


ANLW, *Reactor/Process Interface Requirements*, ANL W7500-0001-ES-00, Revision 0, July 2004.

ASME, *ASME Boiler and Pressure Vessel Code*, Section II, Part D (2001 with 2002 Addenda).

ASME Boiler and Pressure Vessel Code, Section II, "Materials," Part D, "Properties," 2004 Edition, with 2005 and 2006 Addenda

Aspen Technology, *HYSYS Process Version 2.2.2*, www.aspentech.com, 2005.

Aspen Technology, *HYSYS Simulation Basis Manual,* www.aspentech.com, 2002.

Bammert, K. and R. Klein, "The Influence of He-Ne, He-$N_2$, and He-$CO_2$ Gas Mixtures on Closed-Cycle Gas Turbines", ASME 74-GT-124, 1974.

Bird, R. B., W. E. Stewart, and E. N. Lightfoot, *Transport Phenomena*, John Wiley & Sons, Inc., New York, 1960.

Collier, J. G., and J. R. Thome, *Convective Boiling and Condensation*, Third Edition, Oxford University Press, Oxford, 1994.

Copsey, B., M. Lecomte, G. Brinkmann, A. Capitaine, and N. Deberne, *The Framatome ANP Indirect-Cycle Very High Temperature Reactor*, Proceedings of ICAPP '04, Paper 4201, June 2004.

Davis, C. B., C. H. Oh, R. B. Barner, S. R. Sherman, and D. F. Wilson, *Thermal-Hydraulic Analyses of Heat Transfer Fluid Requirements and Characteristics for Coupling a Hydrogen Production Plant to a High-Temperature Nuclear Reactor*, INL/EXT-05-00453, June 2005.

Delene, J. G. and C. R. Hudson II, *Cost Estimate Guidelines for Advanced Nuclear Power Technologies*, ONRL/TM-10071, May 1993.

Dostal, V., M. J. Driscoll, and P. Hejzlar, *A Supercritical Carbon Dioxide Cycle for Next Generation Nuclear Reactors*, MIT-ANP-TR-100, March 2004.

DST Computer Services, S. A., *PipeStress*, Geneva, Switzerland, Version 3.5.1+026, June 2004.

Ely, J. F and H. J. M. Hanley, "Prediction of Transport Properties, I. Viscosities of Fluids and Mixtures", *Ind. Eng. Chem. Fundam.*, 1981, 20, 323.

Ely, J. F and H. J. M. Hanley, "Prediction of Transport Properties, II. Thermal Conductivities of Fluids and Mixtures", *Ind. Eng. Chem. Fundam*, 1983, 22, 90.

General Atomics, *Gas Turbine-Modular Helium Reactor (GT-MHR) Conceptual Design Description Report*, GA Project No. 7658, 910720 Revision 1, July 1996.

*Generation IV Roadmap, Description and Evaluation of Candidate Gas-Cooled Reactor Systems*, TWG-2, Summary Prt XR01-03, December 2001.

Heatric, www.heatric.com, 2005.

Independent Technology Review Group, *Design Features and Technology Uncertainties for the Next Generation Nuclear Plant*, INEEL/EXT-04-01816, 2004.

INEEL, *Next Generation Nuclear Plant Research and Development Program Plan*, INEEL/EXT-05-02581, January 2005.

INEEL, *RELAP5-3D Code Manual Volume 4: Models and Correlations*, INEEL-98-00834, Revision 2.2, 2003.

Kayes, W. M., and M.E. Crawford, *Convective Heat and Mass Transfer*, Second Edition, McGraw-Hill Book Company, New York, 1980.

MacDonald, P. E., J. Buongiorno, *Design of an Actinide Burning, Lead or Lead-Bismuth Cooled Reactor That Produces Low Cost Electricity*, INEEL/EXT-02-01249, October 2002.

MacDonald, P. E., J. W. Sterbentz, R. L. Sant, P. D. Bayless, R. R. Schultz, H. D. Gougar, R. L. Moore, A. M. Ougouag, and W. K. Terry, *NGNP Preliminary Point Design – Results of the Initial Neutronics and Thermal-Hydraulic Assessments*, INEEL/EXT-03-00870, Rev. 1, September 2003.

NIST database, http://webbook.nist.gov/chemistry/, 2005.

O' Brien, J. E., C. M. Stoots, and G. L. Hawkes, *Comparison of a One-Dimensional Model of a High-Temperature Solid-Oxide Electrolysis Stack with CFD and Experimental Results*, Proceedings of 2005 ASME International Mechanical Engineering Congress and Exposition IMECE2005, Orlando, FL, November 5-11, 2005.

Peng, D. Y. and Robinson, D. B., *A Two Constant Equation of State*, I.E.C. Fundamentals, 15, pp. 59-64, 1976.

Perry, R., D. Green, and J. Maloney, *Perry's Chemical Engineer's Handbook*, Sixth Edition, McGraw-Hill, 1984.

Peters, M. S., K. D. Timmerhaus, and R. E. West, *Plant Design and Economics for Chemical Engineers*, Fifth Edition, McGraw Hill, New York, 2003.

Richards, M. B., A. S. Shenoy, L. C. Brown, R. T. Buckingham, E. A. Harvego, K. L. Peddicord, S. M. M. Reza, and J. P. Coupey, 2006, *H2-MHR Pre-Conceptual Design Report: SI-Based Plant*, GA-A25401, April 2006.

Saravanamuttoo, H. et al., *Gas Turbine Theory*, Fifth Edition, Prentice Hall, 1996.

Sochet, I., J. L. Rouyer, and P. Hemmerich, *Safe Hydrogen Generation by Nuclear HTR*, Paper 4261, Proceedings of ICAPP '04, Pittsburgh, PA, USA, June 13-17, 2004.

Special Metals, www.specialmetals.com, 2005.

Smith, C., S. Beck, and B. Galyean, *An Engineering Analysis for Separation Requirements of a Hydrogen Production Plant and High-Temperature Nuclear Reactor*, INL/EXT-05-00137 Rev 0, March 2005.

Stoots, C. M., J. E. O'Brien, M. G. McKellar, and G. L. Hawkes, *Engineering Process Model for High-Temperature Electrolysis System Performance Evaluation*, AiChE 2005 Annual Meeting, Cincinnati, OH, October 30 - November 4, 2005

Todreas, N. E. and M. S. Kazimi, *Nuclear Systems I. Thermal Hydraulic Fundamentals*, Hemisphere Publishing Corporation, 1990.

Ulrich, G. D., *A Guide to Chemical Engineering Process Design and Economics*, John Wiley & Sons, New York, 1984.